

GRAPHENE-BASED CHEMICAL VAPOR SENSORS FOR ELECTRONIC NOSE  
APPLICATIONS

by

Eric C. Nallon  
A Dissertation  
Submitted to the  
Graduate Faculty  
of  
George Mason University  
in Partial Fulfillment of  
The Requirements for the Degree  
of  
Doctor of Philosophy  
Electrical and Computer Engineering

Committee:

\_\_\_\_\_ Dr. Qiliang Li, Dissertation Director  
\_\_\_\_\_ Dr. Dimitris E. Ioannou, Committee Member  
\_\_\_\_\_ Dr. Rao V. Mulpuri, Committee Member  
\_\_\_\_\_ Dr. Dimitrios A. Papaconstantopoulos,  
Committee Member  
\_\_\_\_\_ Dr. Vincent P. Schnee, Committee Member  
\_\_\_\_\_ Dr. Monson H. Hayes, Department Chair  
\_\_\_\_\_ Dr. Kenneth S. Ball, Dean, Volgenau School  
of Engineering

Date: \_\_\_\_\_ Spring Semester 2016  
George Mason University  
Fairfax, VA

Graphene-Based Chemical Vapor Sensors for Electronic Nose Applications

A Dissertation submitted in partial fulfillment of the requirements for the degree of Doctor of Philosophy at George Mason University

by

Eric C. Nallon  
Bachelor of Science  
The Pennsylvania State University, 2007

Director: Qiliang Li, Professor  
Department of Electrical and Computer Engineering

Spring Semester 2016  
George Mason University

COPYRIGHT © 2016 BY ERIC C. NALLON  
ALL RIGHTS RESERVED

## **Acknowledgements**

I would like to thank my family, friends, and co-workers who have been there to support me through my academic journey. My mother and father for providing me with a loving and supportive home and all the conditions for success. My wife, Catherine, for her patience, kindness, and support over the many years of schooling. My friends, who have been engaged in my life for many years with their continuous support. Finally, many thanks to my professor and advisor, Prof. Qiliang Li, for his scientific and engineering guidance throughout the years.

# Table of Contents

	Page
List of Tables.....	vii
List of Figures .....	viii
List of Abbreviations .....	xiv
Abstract.....	x
Chapter 1 Electronic Nose Technology.....	1
1.1 The Olfactory System.....	1
1.2 The Electronic Nose.....	3
1.3 Data Analysis and Pattern Recognition Methods .....	6
1.4 State-of-the-Art: Electronic Nose and Graphene Sensors .....	18
Chapter 2 Graphene and its Use as a Chemical Sensing Material .....	25
2.1 Graphene Properties .....	25
2.2 Graphene Production.....	27
2.2.1 Graphite Exfoliation.....	27
2.2.3 Chemical Vapor Deposition .....	28
2.2.4 Epitaxial Growth on SiC .....	30
2.2.5 Graphene Oxide.....	30
2.2.6 Roll-to-Roll Processing.....	31
2.3 Sensor Design .....	31
2.4 Sensor Fabrication.....	32
2.4.1 Fabrication Issues .....	34
2.5 Gas Sensing Setup.....	39
2.6 Issues and Challenges.....	47
2.6.1 Substrate Effects .....	47
2.6.2 Noise .....	49
2.6.3 Fabrication Contamination.....	50
Chapter 3 Characterization and Sensor Response.....	52

3.1 Raman Spectroscopy .....	52
3.2 Response Voltage Dependence and Linearity .....	56
3.2 Response Stability .....	58
3.3 Response Magnitude and Signal-to-Noise .....	60
3.4 Concentration Effects .....	63
3.5 Residual Transfer Polymer Effects .....	64
3.6 Response Mechanism .....	66
Chapter 4 Chemical Discrimination with an Unmodified Graphene Chemical Sensor ....	71
4.1 Abstract.....	71
4.2 Introduction.....	72
4.3 Experimental Methods.....	73
4.4 Sensor Response Data Processing.....	75
4.5 Results and Discussion .....	77
4.6 Classification Accuracy.....	82
4.7 Conclusions.....	84
Chapter 5 Discrimination Enhancement with Transient Feature Analysis of a Graphene Chemical Sensor.....	86
5.1 Abstract.....	86
5.2 Introduction.....	87
5.3 Materials and Methods .....	89
5.4 Data Processing.....	91
5.5 Results and Discussion .....	93
5.6 Discrimination and Classification .....	100
5.7 Conclusions.....	103
Chapter 6 Surface Functionalization of Graphene for Sensor Applications.....	104
6.1 Types of graphene modification .....	104
6.2 Oxygen plasma modification .....	105
6.3 Modification with Diazonium Compounds .....	110
6.4 Polymer modification.....	113
Chapter 7 Cross-Reactive Graphene Sensor Array .....	122
7.1 Abstract.....	122
7.2 Introduction.....	123
7.3 Experimental Section .....	125

7.4 Results and Discussion .....	129
7.5 Conclusions.....	138
7.6 Supporting Information .....	139
Chapter 8 Future Graphene-Based Sensing Work .....	144
References.....	146

## List of Tables

Table	Page
Table 2.1 Mechanical and electrical properties of graphene .....	26
Table 3.1 Average change in resistance and corresponding standard deviation values of a graphene sensor when exposed to acetone, acetonitrile, chloroform, isopropanol, methanol, and toluene for 60 exposures each. ....	60
Table 3.2 Relationship between the molar mass and the calculated time difference between the sensor response with and without PMMA. ....	66
Table 4.1 Maximum change in resistance, SNR values, and corresponding standard deviations for the responses shown in Figure 4.1. The mean and standard deviation were calculated for twenty measurements of each analyte.....	79
Table 4.2 Maximum change in resistance, SNR values, and corresponding standard deviations for the responses shown in Figure 4.3. The mean and standard deviation were calculated for twenty measurements of each analyte.....	81
Table 5.1 Chemical information for mesitylene, o-xylene, p-xylene, and toluene.....	93
Table 7.1 Selected polymers and their respective solvents used as coatings to create a cross-reactive graphene sensor array. ....	128
Table 7.2 Comparison of uncoated and coated sensor responses for a specific coating which produced a notable change for each single compound. ....	133

## List of Figures

Figure	Page
Figure 1.1 Illustration of the human olfactory system .....	3
Figure 1.2 Typical elements that comprise an electronic nose.....	4
Figure 1.3 Bubble chart representing the most popular coding languages of 2015. <sup>4</sup> .....	6
Figure 1.4 Data analysis process flow showing preprocessing, feature extraction, dimensionality reduction, and classifying of chemical sensor data.....	8
Figure 1.5 Example of smoothing sensor data at different smoothing window sizes.....	9
Figure 1.6 Drift correction with a first-order linear fit applied to the sensor baseline data..	10
Figure 1.7 Feature extraction techniques using a) parameters such as maximum change in resistance and signal areas, b) sub-sampling of original response data, and c) transient fitting of response curve.....	13
Figure 1.8 Example of the structure of the feature vector with rows for each measurement and columns for the label and features for each measurement. In this case, the features that were extracted from each measurement are max change, area response, and area recovery..	14
Figure 1.9 The cumulative percent variance for the number of principal components for a PCA transformation.....	16
Figure 1.10 Illustration of k-fold cross-validation using 5 folds. Each row represents a separate prediction performed on that specific testing and train set.....	17
Figure 2.1 Electron cloud configuration above and below graphene. <sup>34</sup> .....	26
Figure 2.2 Mechanical exfoliation process of graphene using the scotch tape method. <sup>38</sup> .....	28
Figure 2.3 Chemical vapor deposition growth of graphene and transfer process with steps a) synthesis of graphene on copper foil, b) spin-coating of PMMA onto the Cu foil to protect graphene, c) etching of Cu, d) transfer of graphene/PMMA film onto glass, e) removal of PMMA in acetone. <sup>40</sup> .....	29

Figure 2.4 Roll-to-roll production of graphene onto a flexible substrate. <sup>42</sup> .....	31
Figure 2.5 a) Sensor design consisting of interdigitated electrode contacts deposited on an Si/SiO <sub>2</sub> /Graphene substrate and b) typical time-dependent change in resistance of the graphene chemical sensor .....	32
Figure 2.6 Graphene sensor fabrication process steps. ....	34
Figure 2.7 a) Cleaved graphene pieces, b) photolithography pattern for a single device, and c) completed sensor wire bonded in leadless chip carrier. ....	34
Figure 2.8 SEM images of a) wire bond attached to lifted metal pad, b) IDE pattern lifting from the substrate, and c) complete removal of metal IDE. ....	36
Figure 2.9 Confocal laser scanning microscope image showing the removal of the metal contact pattern from few-layer graphene. ....	36
Figure 2.10 SEM images of graphene appearing to have been unintentionally etched during photoresist development. ....	37
Figure 2.11 Microscope images of processed graphene device a) before metal deposition and b) after metal deposition. ....	38
Figure 2.12 Raman spectra of processed graphene device taken before metal deposition and after metal deposition.....	39
Figure 2.13 Gas Sensing test fixture showing a) LCC socket with LCC and Teflon gasket, b) bottom of Teflon flow cell, and c) top of Teflon flow cell.....	40
Figure 2.14 a) Keithley 2450 source meter used for single device measurements and b) United Electronics Industry data acquisition cube. ....	41
Figure 2.15 Typical sensor response showing change in resistance for baseline (I), sample (II), and recovery (III) regions. ....	41
Figure 2.16 Time-series plot of a graphene sensor exposed to various flow rates of chloroform vapor ranging from 1 mL/min to 50 mL/min.....	43
Figure 2.17 Vapor generation and sampling systems utilizing a a) bubbler method and b) headspace method. ....	46
Figure 2.18 Plot illustrating the effect of different substrates on the surface reactivity of graphene. <sup>44</sup> .....	48

Figure 2.19 Low-frequency noise spectra of a graphene device while exposed to various chemicals. <sup>47</sup> .....	50
Figure 3.1 Raman spectra for graphene samples comparing a) graphite and single layer graphene for all bands, b) shift in the G-band for graphite, single layer, and double layer graphene, and c) the change in G-band intensity for graphite, single layer, and double layer graphene. <sup>51</sup> .....	54
Figure 3.2 Raman spectra for graphite and Graphene Supermarket CVD single layer, single double layer, and few layer graphene. ....	55
Figure 3.3 Raman spectra for single layer graphene, purchased from Graphenea, from three separate batches. ....	56
Figure 3.4 Current versus voltage measurement for graphene sensor .....	57
Figure 3.5 Resistance values while exposed to various chemical compounds for different operating voltages. ....	58
Figure 3.6 Time-series plot of the change in resistance and b) sample-to-sample variation of the response for a graphene sensor exposed to acetone, acetonitrile, chloroform, isopropanol, methanol, and toluene for 60 exposures each.....	60
Figure 3.7 Sensor response for device using a) single layer graphene and b) few-layer graphene. ....	61
Figure 3.8 a) Change in resistance and b) signal-to-noise ratio for single layer graphene and few layer graphene . ....	62
Figure 3.9 Concentration dependent response characteristics for acetonitrile, chloroform, and toluene showing a) variation in the change in resistance and b) PCA plot with wandering points which eventually converge at low concentrations.....	64
Figure 3.10 Comparison of sensor response with and without PMMA transfer polymer for chloroform, diethyl ether, acetone, acetonitrile, and formaldehyde.....	66
Figure 3.11 Proposed graphene sensor response mechanism for when the graphene becomes a) more conductive and b) less conductive. ....	70
Figure 4.1 Typical sensor response curve with regions I) baseline, II) sample, and III) recovery. Potential features that can be extracted include the maximum change in resistance ( $\Delta R$ ), area of the response (red shaded area), and area of the recovery (green shaded area)..	76
Figure 4.2 a) Normalized sensor response to a chemically diverse set of compounds and b) corresponding PCA transform.....	78

Figure 4.3 a) Sensor response to a group of substituted benzene compounds and b) corresponding PCA transform.....	80
Figure 4.4 Classification accuracy comparison for the chemically diverse and substituted benzene data sets using K-Nearest Neighbors, Linear SVM, Random Forest, and Linear Discrimination Analysis classifiers. ....	83
Figure 4.5 Confusion matrix showing correctly and incorrectly classified compounds for a) substituted benzene set using LDA and b) chemically diverse set using kNN.....	84
Figure 5.1 Typical sensor response curve with regions I) baseline, II) sample, and III) recovery. Features include the maximum change in resistance ( $\Delta R$ ), area of the response (red shaded area), area of the recovery (green shaded area), and exponential fitting coefficients from the sample ( $\alpha_S$ , $\beta_S$ , $\gamma_S$ ) and recovery ( $\alpha_R$ , $\beta_R$ , $\gamma_R$ ) regions.....	92
Figure 5.2 Sensor response to a group of analytes highlighting the overlap that can be encountered between responses.....	94
Figure 5.3 a) Plotted fitting coefficients for each compound, b) feature importance weights for each feature determined by a random forest classifier, and c) standard deviation values for each feature.....	97
Figure 5.4 Relationship between a) compound mass ( $1/m$ ) and adsorption frequency factor fitting term ( $\alpha_S$ ) and b) vapor pressure (VP) and desorption exponential fitting term ( $\beta_R$ ). ....	100
Figure 5.5 PCA transform for a feature vector containing a) $\Delta R$ , $A_S$ , $A_R$ and b) supplemented exponential fitting coefficients $\alpha_S$ , $\beta_S$ , $\gamma_S$ , $\alpha_R$ , $\beta_R$ , and $\gamma_R$ . ....	101
Figure 5.6 Classification accuracy comparison using parameters features only and supplementing with transient features from exponential fitting.....	102
Figure 6.1 a) Noncovalent and b) covalent functionalization of graphene. <sup>106</sup> .....	105
Figure 6.2 Raman spectra of single-layer graphene subjected to oxygen plasma for different amounts of time.....	107
Figure 6.3 Comparison of oxygen plasma treated sensor response to 3-nitrotoluene, 4-chlorotoluene, chlorobenzene, and nitrobenzene.....	108
Figure 6.4 Comparison of oxygen plasma treated sensor response to phenol, 4-chlorophenol, and 4-chloroaniline.....	109
Figure 6.5 SEM image of graphene sensor treated with an oxygen plasma for 60s at 10 W. ....	110

Figure 6.6 Various diazonium compound functional groups with their relative dipole moments. <sup>110</sup> .....	111
Figure 6.7 Raman spectra of graphene sensor modified with nitrobenzene diazonium tetrafluoroborate.....	112
Figure 6.8 Response comparison of an unmodified and NBD-functionalized SLG sensor. ....	113
Figure 6.9 SEM images of five different polymers spin-cast from a chloroform solution over the graphene sensor electrode array. ....	115
Figure 6.10 24-element sensor array a) photolithography metallization mask design, b) photolithography SU8 mask design, and c) completed device in LCC. ....	116
Figure 6.11 Confocal laser scanning microscope images of a single sensor element in a) color, b) intensity, and c) false height coloring along with the d) step profile along the electrode array. ....	117
Figure 6.12 Sensor array output response towards chloroform and formaldehyde for an array containing an un-coated sensor along with 5 polymer-coated sensors. ....	119
Figure 6.13 Single graphene sensor without surface modification to cyclohexanone, diethyl ether, hexane, and toluene, highlighting the similar response patterns that cause misclassifications during the classification process. ....	120
Figure 6.14 Sensor array output response towards cyclohexanone, diethyl ether, hexane, and toluene. ....	121
Figure 7.1 24-element graphene sensor array a) photolithography mask design and b) completed device, mounted and wire bonded in a leadless chip carrier with polymers applied to each sensor element. ....	127
Figure 7.2 a) Cross-reactive response behavior of the graphene sensor array with 23 different polymer coatings, comparing the maximum change in resistance upon exposure to acetone, acetonitrile, methanol, and tetrahydrofuran. Time-series plots of maximum change in resistance for coatings b) PVPh, PVPy, PCI, PEG, and PVBP while exposed to acetonitrile and c) TEGDME, PDMS, PVPYd, PCI, and PEG while exposed to methanol. ....	132
Figure 7.3 Analysis of graphene sensor array with a) a correlation heatmap and b) hierarchical cluster analysis dendrogram. ....	135
Figure 7.4 Time-series plots of PECH and PDMS-Alk coated sensors demonstrating the variations that can be seen for sensors with different polymer coatings. ....	136

Figure 7.5 Graphene sensor response to the headspace of various Scotch whiskies for an a) uncoated sensor and sensors coated with b) Nafion, c) 2-Hydroxyethyl cellulose, and d) Poly(4-tert-butylstyrene).....	138
Figure 7.6 Cross-reactive behavior of the graphene sensor array, with 23 different polymer coatings, comparing the maximum change in resistance response pattern towards ethanol, methanol, acetone, cyclohexanone, tetrahydrofuran, diethyl ether, formaldehyde, 2-nitrotoluene, 4-chlorotoluene, toluene, hexane, chloroform, acetonitrile, and dimethyl sulfoxide.....	140
Figure 7.7 Array maximum change in resistance response values shown with actual value and also represented by color mapping, with red indicating an increase in resistance and blue indicating a decrease in resistance. ....	141
Figure 7.8 Times-series change in resistance for each sensor type towards 2-Nitrotoluene, 4-Chlorotoluene, Acetone, Acetonitrile, Chloroform, Cyclohexanone, Diethyl Ether, Dimethyl Sulfoxide, Ethanol, Formaldehyde, Hexane, Methanol, Tetrahydrofuran, and Toluene. ....	142
Figure 7.9 Linear discrimination transform of Scotch whisky data displaying excellent class separation.....	143

## List of Abbreviations

2D	2-Dimensional
2NT	2-Nitrotoluene
ACN	Acetonitrile
ANN	Artificial Neural Network
Au	Gold
CNT	Carbon Nanotube
CO	Carbon Monoxide
CSV	Comma Separated Values
Cu	Copper
CVD	Chemical Vapor Deposition
DMSO	Dimethyl Sulfoxide
DNA	Deoxyribonucleic acid
DNB	Dinitrobenzene
DNT	Dinitrotoluene
e-nose	Electronic Nose
FLG	Few-Layer Graphene
H <sub>2</sub> O	Water
HCA	Hierarchical Clustering Analysis
I <sub>2</sub>	Iodine
IDE	Interdigitated Electrode
KNN	k-Nearest Neighbor
LCC	Leadless Chip Carrier
LDA	Linear Discrimination Analysis
LSER	Linear Solvation Energy Relationship
MeOH	Methanol
MFC	Mass Flow Controller
MOS	Metal Oxide Semiconductor
NBD	Nitrobenzene Diazonium Tetrafluoroborate
NH <sub>3</sub>	Ammonia
Ni	Nickel
NO <sub>2</sub>	Nitrogen Dioxide
OHcell	2-Hydroxyethyl cellulose
ORN	Olfactory receptor Neuron
P4tBS	Poly(4-tert-butylstyrene)
P6DS	Poly(1-hexadecene-sulfone)
PACN	Polyacenaphthylene
PBMA	Poly(benzyl methacrylate)

PBrS	Poly(4-bromostyrene)
PC	Principal Component
PCA	Principal Component Analysis
PCB	Printed Circuit Board
PCL	Polycaprolactone
PDMS-Alk	Poly(dimethylsiloxane-co-alkylmethylsiloxane)
PECH	Polyepichlorohydrin
PEEK	Polyether Ether Ketone
PEG	Polyethylene glycol
PEO	Poly(ethylene oxide)
PEVA	Poly(ethylene-co-vinyl acetate)
PIB	Polyisobutylene
PMMA	Poly(methyl methacrylate)
ppt	Parts Per Trillion
PS	Polystyrene
PVA	Poly vinyl alcohol
PVBCI	Poly(vinylbenzyl chloride)
PVBP	Poly(4-vinylbiphenyl)
PVPh	Poly(4-vinylphenol)
PVPy	Poly(4-vinylpyridine)
PVPyd	Polyvinylpyrrolidone
QCM	Quartz Crystal Microbalance
QD	Quantum Dot
R2R	Roll-to-Roll
RDX	1,3,5-trinitroperhydro-1,3,5-triazine
RF	Random Forest
SAW	Surface Acoustic Wave
SDLG	Single Double Layer Graphene
SEM	Scanning Electron Microscope
Si	Silicon
SiC	Silicon Carbide
SiO <sub>2</sub>	Silicon Dioxide
SLG	Single Layer Graphene
SNR	Signal-to-Noise Ratio
STD	Standard Deviation
SVM	Support Vector Machine
TEGDME	Tetraethylene glycol dimethyl ether
THF	Tetrahydrofuran
Ti	Titanium
TMAH	Tetramethyl Ammonium Hydroxide
TNT	Trinitrotoluene
UEI	United Electronics Industry
USB	Universal Serial Bus
VOCs	Volatile Organic Compounds

## **Abstract**

### **GRAPHENE-BASED CHEMICAL VAPOR SENSORS FOR ELECTRONIC NOSE APPLICATIONS**

Eric C. Nallon, Ph.D.

George Mason University, 2016

Dissertation Director: Dr. Qiliang Li

An electronic nose (e-nose) is a biologically inspired device designed to mimic the operation of the olfactory system. The e-nose utilizes a chemical sensor array consisting of broadly responsive vapor sensors, whose combined response produces a unique pattern for a given compound or mixture. The sensor array is inspired by the biological function of the receptor neurons found in the human olfactory system, which are inherently cross-reactive and respond to many different compounds. The use of an e-nose is an attractive approach to predict unknown odors and is used in many fields for quantitative and qualitative analysis. If properly designed, an e-nose has the potential to adapt to new odors it was not originally designed for through laboratory training and algorithm updates. This would eliminate the lengthy and costly R&D costs associated with materiel and product development. Although e-nose technology has been around for over two decades, much research is still being undertaken in order to find new and more diverse types of sensors.

Graphene is a single-layer, 2D material comprised of carbon atoms arranged in a hexagonal lattice, with extraordinary electrical, mechanical, thermal and optical properties due to its 2D,  $sp^2$ -bonded structure. Graphene has much potential as a chemical sensing material due to its 2D structure, which provides a surface entirely exposed to its surrounding environment. In this configuration, every carbon atom in graphene is a surface atom, providing the greatest possible surface area per unit volume, so that electron transport is highly sensitive to adsorbed molecular species. Graphene has gained much attention since its discovery in 2004, but has not been realized in many commercial electronics. It has the potential to be a revolutionary material for use in chemical sensors due to its excellent conductivity, large surface area, low noise, and versatile surface for functionalization.

In this work, graphene is incorporated into a chemiresistor device and used as a chemical sensor, where its resistance is temporarily modified while exposed to chemical compounds. The inherent, broad selective nature of graphene is demonstrated by testing a sensor against a diverse set of volatile organic compounds and also against a set of chemically similar compounds. The sensor exhibits excellent selectivity and is capable of achieving high classification accuracies. The kinetics of the sensor's response are further investigated revealing a relationship between the transient behavior of the response curve and physiochemical properties of the compounds, such as the molar mass and vapor pressure. This kinetic information is also shown to provide important information for further pattern recognition and classification, which is demonstrated by increased classification accuracy of very similar compounds. Covalent modification of the graphene surface is demonstrated by means of plasma treatment and free radical exchange, and sensing performance compared to an unmodified graphene sensor. Finally, the first example

of a graphene-based, cross-reactive chemical sensor array is demonstrated by applying various polymers as coatings over an array of graphene sensors. The sensor array is tested against a variety of compounds, including the complex odor of Scotch whiskies, where it is capable of perfect classification of 10 Scotch whiskey variations.

# Chapter 1 Electronic Nose Technology

## 1.1 The Olfactory System

The olfactory system is the sensory system in mammals responsible for the ability to smell and has a remarkable capability to distinguish a wide range of odors. For instance, humans have approximately 6 million receptors and have typically been known to be capable of distinguishing approximately 10,000 odors.<sup>1</sup> Recent research suggests that this number has been severely underestimated. Through empirical studies, it is estimated that humans can discriminate at least 1 trillion odors.<sup>2</sup> Canines have always been known for their keen sense of smell and are often regarded as the best method of chemical detection to date. The olfactory system of a dog is believed to be capable of detecting odorant concentration levels at 1-2 ppt, which is roughly 10,000 – 100,000 times more sensitive than the sensitivity of a human. Also, Canines poses somewhere in the range of 125 – 250 million receptors and have a larger percentage of their brain dedicated to olfactory processing.<sup>3</sup> In either case, the major components of each olfactory system are quite similar. The differences include the number of sensory neurons, the nasal flow path, and the actual sniffing action during olfaction.

Two major components that are common to the olfactory system of humans, canines, and others are olfactory receptor neurons (ORNs) and the olfactory bulb. The ORNs operate in such a way that they are not activated by specific compounds, but rather

that an odorant can activate multiple receptors, and a receptor can be activated by multiple odorants. This cross-reactive design of the receptors is at the foundation of electronic nose (e-nose) systems and is of fundamental importance for designing such systems. One important and remarkable distinction between the ORNs and artificial sensors is that these receptor neurons are continuously regenerated, unlike most other neurons, which die and are never replaced.<sup>1</sup>

Odors are typically characterized as being hydrophobic, volatile compounds with a molecular weight of less than 300 g/mol.<sup>4</sup> Most odors are mixtures of hundreds of compounds opposed to a single compound. The ability to identify and differentiate odors starts with the detection of odor molecules at ORNs. When the odor molecules bind to ORNs, an electrical signal is triggered, and then travels along olfactory axons to the olfactory bulb. The overall function of the olfactory bulb is to receive, process, and relay olfactory information to the limbic region of the brain where further pattern recognition is performed to identify the odor. The operations that occur inside the olfactory bulb remain unclear at this point, but it appears that the received activated neuron signals are encoded as sensory information, which describes the spatial and temporal response pattern of the ORNs. The encoded sensory information is then passed to the limbic region of the brain where patterns are recognized, and the odor is either learned for the first time or identified as a previously encountered odor. Shown in Figure 1.1 is an illustration of the olfactory system showing where the ORNs and olfactory bulb reside, and the connections between the receptor neurons and the olfactory bulb.<sup>5</sup>

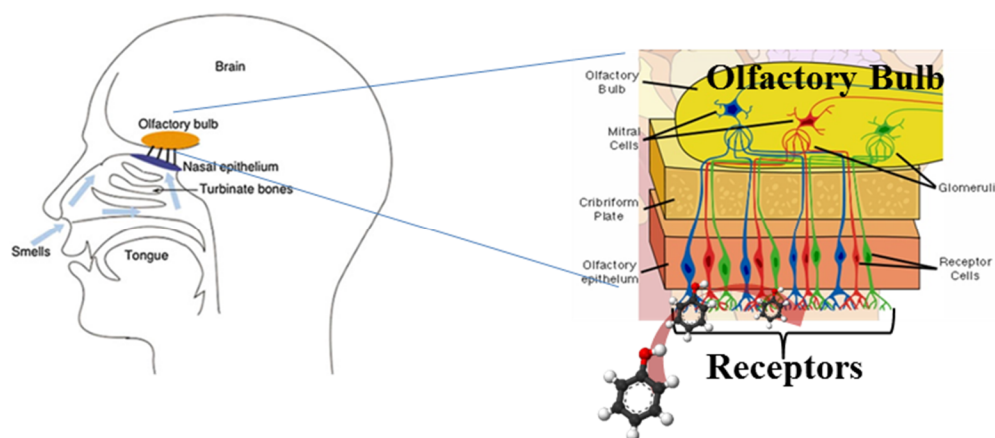


**Figure 1.1** Illustration of the human olfactory system

Another astonishing attribute of this process is the fact that, normally, the brain only needs to be trained once on a given odor before it can accurately predict that odor in the future, as opposed to artificial olfaction, which often needs to be trained many times in order to accurately predict an odor in the future. This is most likely attributed to the inability to properly design a highly dimensional sensor-array response with cross-reactive characteristics, and also the inefficient translation of sensor signals into meaningful response patterns.

## 1.2 The Electronic Nose

An e-nose is a biologically inspired device designed to mimic the olfactory system. The concept and design of this type of sensor system is very different from the lock-and-key approach of designing a sensor to detect a very specific compound. Sensor arrays comprised of multiple specifically designed sensors have been successfully created, but the major limitation lies in detecting new compounds outside their originally intended design. The e-

nose, being inspired by the biological functions of the olfactory system, is designed to contain an array of broadly responding (i.e., cross-reactive) sensors. The array elements respond to a broad number of compounds, with specificity being achieved by relationships and patterns across the array. Sensory information is encoded in features which are extracted from each sensor. This depends on the type of sensor technology being used. The main attraction of this type of sensor design is that if the sensor array is designed with enough dimensionality, it would be capable of detecting and classifying new, previously unforeseen compounds. This is a powerful concept since it would allow for a sensor system to have the ability to adapt to new scenarios, adding additional capability without the need for costly and time consuming hardware development. The sensor array in an en-nose is a very important piece, but is not able to provide direct classification of compounds on its own. The important elements of an e-nose are illustrated in Figure 1.2, showing a sensor array, a feature extraction method, and pattern classification.

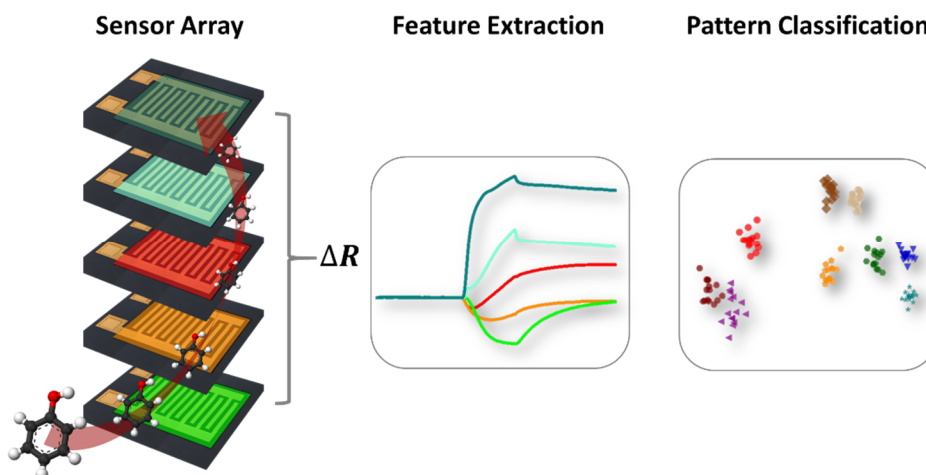


**Figure 1.2** Typical elements that comprise an electronic nose.

As previously described, the sensor array is comprised of cross-reactive array elements, where each sensor is broadly responsive. In this case, a change in resistance ( $\Delta R$ ) for each sensor is recorded. The  $\Delta R$  feature needs to be extracted to describe the response of that sensor to the compound. In some cases, certain features of the sensor response can be directly related to physiochemical properties of the compound. This process is where most of the human-in-the-loop interaction takes place since a sensor designer may intimately understand the sensor material and have insight into the physical and chemical mechanisms involved with the interaction of the compound with the sensing material. Once the features have been extracted from each sensor response, they are formatted into a specific feature vector format and then supplied to a pattern recognition and machine learning algorithm. During classification, the feature vector data is typically split into training and testing sets, where the training set is used to train the algorithm to learn the provided features, while the testing set is used to test the ability of the trained algorithm to correctly classify the compounds. This train/test process is used to validate the overall classification accuracy of the sensor system so that when the sensor has collected new data, a level of confidence as to how it will perform can be trusted. For sensor systems that are used in real-world applications, the sensor is often trained in a laboratory on the anticipated set of compounds it can detect under various environmental conditions, along with common compounds which may confuse or interfere with the correct classification of the target compounds. These variables induce noise into the classification system and can help to tune the prediction algorithm to be more robust.

### 1.3 Data Analysis and Pattern Recognition Methods

Besides programs such as Matlab and Microsoft Excel, many programming languages exist which can be used to perform data analysis by reading data, performing analysis, then creating visualizations and generating consolidated reports. According to [www.codeeval.com](http://www.codeeval.com), the most popular programming language in 2015 is Python, followed by Java, C++, and Javascript. The breakdown of the popularity of 19 different programming languages analyzed by processing of over 600,000+ coding tests and challenges is shown in Figure 1.3.<sup>6</sup> The popularity of Python has risen over the years to make it into this position. It can most likely be attributed to no monetary cost to obtain, a vast amount of library modules available, and a large active development and user community.

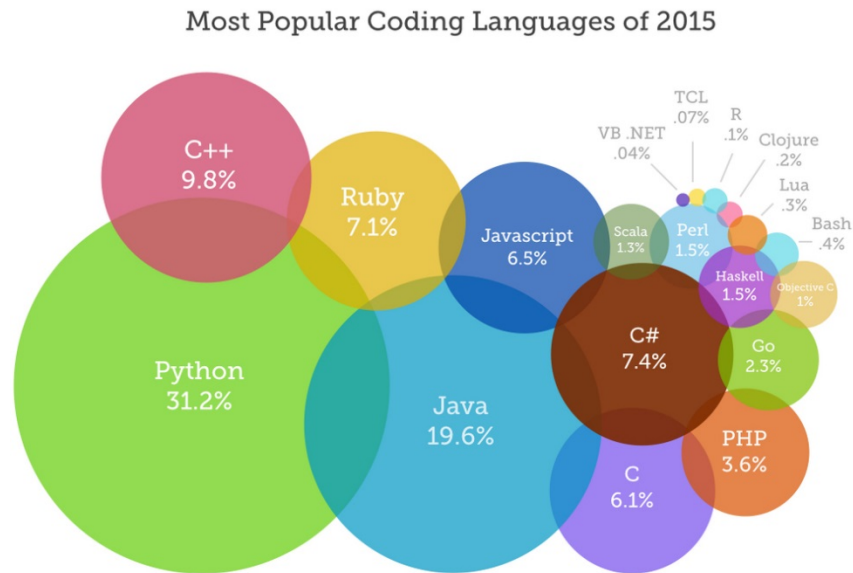


**Figure 1.3** Bubble chart representing the most popular coding languages of 2015.<sup>6</sup>

Throughout this dissertation, Python will be used exclusively with some of its many libraries that are related to numerical manipulation and machine learning, such as SciPy,<sup>7</sup> Numpy,<sup>8</sup> Pandas,<sup>9</sup> Scikit-learn,<sup>10,11</sup> and Matplotlib.<sup>12</sup> The Scipy library contains modules for optimization, linear algebra, integration, interpolation, various transforms, signal/image processing, and many more modules for scientific computing. Numpy is a library primarily used for multi-dimensional array and matrix mathematical manipulation and creation, and is an efficient way to handle and perform operations on large data sets. The Pandas library can be used for reading and writing of data in multiple formats, data alignment, reshaping/transposing, data slicing, and structure manipulation such as merging and joining. Pandas also has some statistical and signal processing features such as data smoothing. Scikit-learn is a library solely built for machine learning based functions; Common procedures that it can perform include data preprocessing, clustering, dimensionality reduction, classification, regression, and model selection. Matplotlib is a Matlab-style plotting library capable of producing publication quality visualizations such as time-series plots, bar plots, scatter plots, histograms, and 3D contours.

### **Data Analysis, Pattern Recognition, and Classification**

The first step of data analysis is the collection of sensor data in a suitable format. Sensor data should be collected in its most raw form in order to maintain the integrity of the original measurement. On-board signal processing such as filtering and averaging can work very well, but these operations are usually permanently applied to the measured data, unless custom hardware/software outputs raw measurements as well. A generic illustration of the

overall data analysis process flow is shown in Figure 1.4, which consists of 5 main steps: collection of sensor data, preprocessing, feature extraction, dimensionality reduction, and classification. This is not a strict definition for achieving the end goal of classifying sensor data into a decision, but rather a general guide to the steps needed to achieve this. The actual collection of sensor data will be described in much detail in later chapters. At this point, we can consider that sensor data has been collected from either a single sensor or an array of sensors, and is represented by an array of resistance and timestamp values which have been read into an appropriate data analysis platform such as Python. The measured sensor data is in its most raw form and contained in a data matrix array format for ease of further processing. The next step is to perform data preprocessing on the raw sensor data in order to condition the data for further steps.

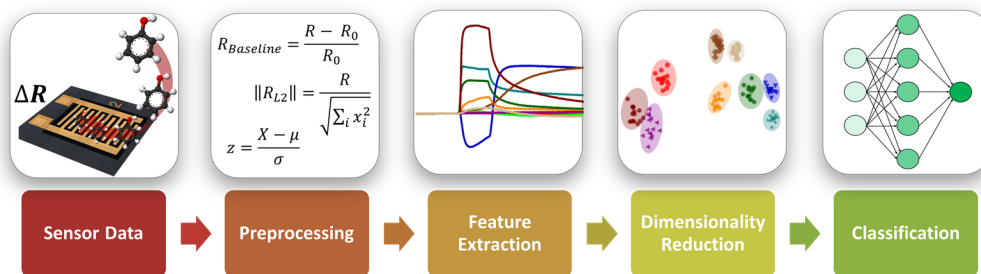


**Figure 1.4** Data analysis process flow showing preprocessing, feature extraction, dimensionality reduction, and classifying of chemical sensor data.

Data preprocessing broadly refers to any transformation performed on the raw sensor data prior to building the analysis model and can largely be broken into processes to

reduce noise/drift and to perform numerical preconditioning. Examples of noise/drift reduction may include smoothing, drift correction, and baseline manipulation, while examples of numerical preconditioning usually deal with applying normalization and scaling operations to the sensor data. Smoothing of data can be performed by using a moving window average with a defined smoothing window (e.g., boxcar, blackman, hamming) and a specified window size. This can be accomplished with the Python Pandas module.<sup>9</sup> An example of applying smoothing at different window sizes is shown in Figure 1.5, where a boxcar type window with window sizes of 5, 10, and 15 points was used to smooth the original data. A clear difference can be even be observed between the original sensor data and the data with 5-point smoothing performed. Beyond the 5-point smoothing, minimal differences can be seen and one must be careful not to simply smooth at a higher window size, since this would increase the likelihood of smoothing or smearing an important feature. Statistical techniques can be helpful to determine a range of smoothing parameters by analyzing the noise in the signal and taking into account the data collection rate.

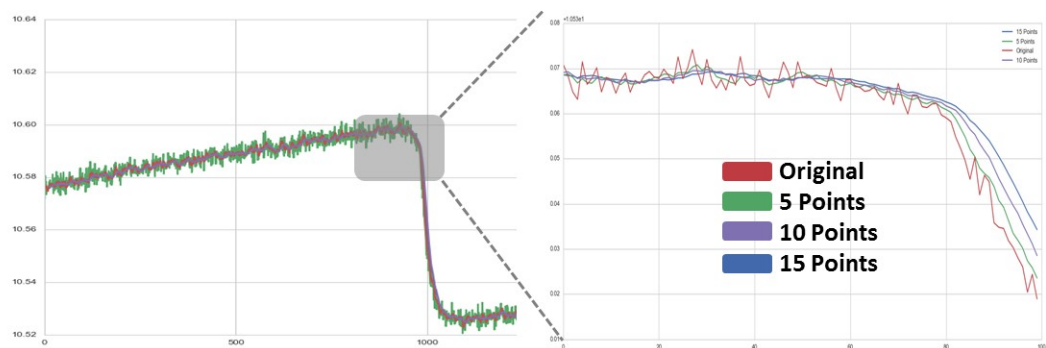


**Figure 1.5** Example of smoothing sensor data at different smoothing window sizes.

Sensors of all kinds almost always exhibit some kind of drift over time. This affect is particularly prevalent in sensors that contain a reactive material, such as a chemical sensor. Not only does drift occur as the sensor recovers from a previous exposure, but chemical sensors are often prone to temperature and humidity changes due to interaction with the sensing material. One method to correct this drift is to apply a first-degree linear fit to the baseline data before the sensor responds, then determine the difference in slope of this line relative to a horizontal line, which represent zero drift. Once this difference is found, it can be used to adjust the original data into drift corrected data. Shown in Figure 1.6 are two examples of how applying a drift correction technique can significantly correct a drifting signal. This step is important for further processing when features are extracted from the response signal, and is especially important when performing feature calculations such as the maximum change in resistance and areas under a curve. Drift correcting does not change the dynamics of the original sensor response, but rather creates a common reference, which calculations can be compared to.

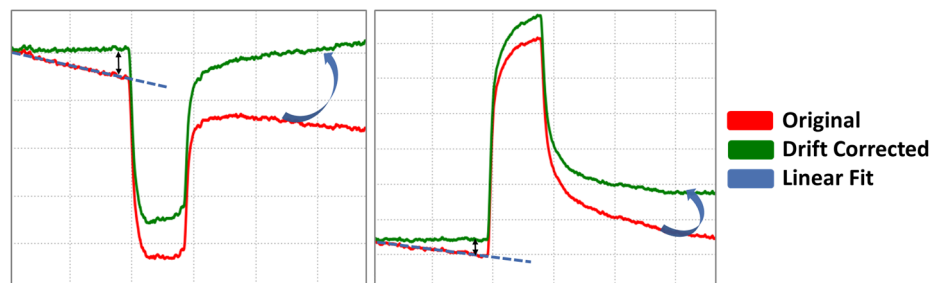


**Figure 1.6** Drift correction with a first-order linear fit applied to the sensor baseline data.

Another important preprocessing step is the manipulation of the sensor response with respect to its baseline for the purposes of contrast enhancement and scaling.<sup>4</sup> Three of the most commonly used scaling techniques are differential, relative, and fractional. The differential method subtracts the baseline from the sensor response, and as a result, any additive noise that may be present in the sensor signal is removed. The relative method divides the sensor response by the baseline, which eliminates the effect of multiplicative drift and creates a dimensionless response. Finally, the fractional method subtracts the baseline then divides by the baseline, creating a normalized, dimensionless response represented in per-unit change. The equations for the described differential, relative, and fractional scaling methods can be seen in equations 1, 2, and 3, respectively.

$$R_{Differential} = R - R_{Baseline} \quad (1)$$

$$R_{Relative} = \frac{R}{R_{Baseline}} \quad (2)$$

$$R_{Fractional} = \frac{R - R_{Baseline}}{R_{Baseline}} \quad (3)$$

The next step in the data analysis process is the extraction of features from the sensor response data. Feature extraction is also sometimes referred to as feature engineering. It deals with the process of gaining information from the sensor data by describing features which characterize the sensor response. The features are used to train the classification algorithm and are also the same features that will be extracted from unknown sensor data. This step is probably the most important step in the entire process since the features are what truly describe the response of the sensor. This is also the step which requires the most human intuition, and knowledge of the type of sensor and the physical response mechanisms that produce the sensor response. The underlying

mechanisms that govern the physical and chemical interactions between the compound and the sensor are principles that can be used to develop meaningful features. Three examples of types of features that can be extracted from temporal chemical sensor response data are shown in Figure 1.7. Parameter extraction refers to the calculation of features such as the maximum change in signal, and areas calculated for the sampling ( $A_S$ ) and recovery ( $A_R$ ) periods of the response. This method requires either knowing when the sample and recovery period begin via a hardware trigger, or a detection algorithm capable of finding these points of transition. The next technique, labeled at sub-sampling, simply takes the drift-corrected data and samples it at a lower rate, pulling out equally spaced resistance values. This method can be used on the entire response signal or can be limited to only the sample and recovery regions. The last method deals with applying fitting models to the sample and recovery portions of the response in order to extract fitting coefficients. The sample and recovery regions of the response curve can be fit with exponential or polynomial equations, where the fitting coefficients describe the shape of each response. This method could be very powerful since the fitting coefficients could be indirectly related to the actual compound being sensed due to absorption and desorption kinetics. This method is computationally expensive and could be prone to mistakes if integrated into an automated fashion, due to the fitting of anomalies in the signal that can occur.

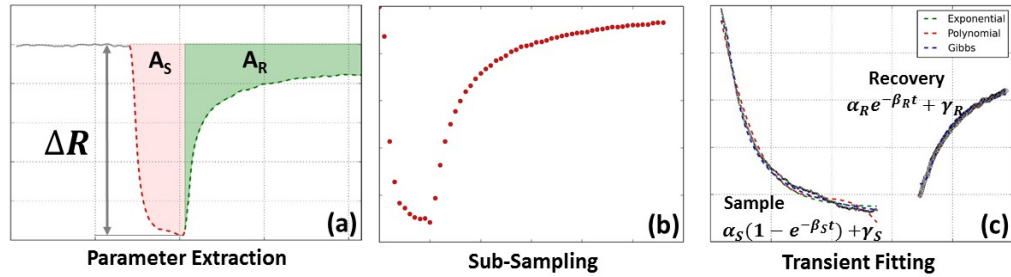


**Figure 1.7** Feature extraction techniques using a) parameters such as maximum change in resistance and signal areas, b) sub-sampling of original response data, and c) transient fitting of response curve.

Subsequent pattern recognition, clustering, and classification techniques require the data to be in a specific format. The features that were previously described are extracted for each measurement and assigned a label corresponding to the true identity of the class for that measurement. The features are put into an  $M \times N$  array, with  $M$  measurements and  $N$  features; this array is called the feature vector. Shown in Figure 1.8 is an example of the structure of a feature vector for 18 measurements with max change, area response, and area recovery extracted from each. Each measurement is contained in a row and the columns represent the label, max change, area response, and area recovery.

Label	Max Change	Area Response	Area Recovery
2-Nitrotoluene	-0.175	-4.676	-9.724
4-Chlorotoluene	-0.542	-15.440	-14.411
Acetic Acid	-1.949	-54.862	-219.495
Acetone	0.929	25.157	90.047
Acetonitrile	-0.214	-5.514	1.914
Ammonium Hydroxide	1.630	47.836	264.222
Blank	0.007	0.291	3.270
Chloroform	-1.149	-34.634	-36.476
Cyclohexanone	0.622	18.454	67.599
Diethyl Ether	0.446	12.603	19.088
Dimethyl Sulfoxide	0.201	9.689	112.079
Ethanol	0.042	1.427	5.386
Formaldehyde	0.045	1.607	14.686
Hexane	-0.145	-4.232	-1.834
Phenol	-0.026	-0.966	-14.852
Tetrahydrofuran	0.920	26.097	66.698
Toluene	-0.162	-4.462	-4.401
Water	0.010	0.411	9.037

**Figure 1.8** Example of the structure of a feature vector with rows for each measurement and columns for the label and features. In this case, the features that were extracted from each measurement are max change, area response, and area recovery.

A powerful technique for exploring a data set and structure that may exist in the data is principal component analysis (PCA). PCA is a linear transformation into an alternate coordinate system which highlights similarities and differences in the underlying structure of the data. The input data to PCA is the feature vector, where the features are used to describe the data. The data is measured in terms of its principal components (PC), which represent the variance contained in that particular direction. The PCs are arranged in descending order, with PC1 representing the direction that contains the most variance in the system. Each PC is a linear combination from all features in the original feature vector and each PC is orthogonal to each other. PCA is computed by finding the eigenvectors and eigenvalues of the covariance matrix, where the covariance matrix is used to measure how

much the dimensions vary from the mean with respect to each other. The eigenvalues are used to define the magnitude of each PC and the eigenvectors are used to define the direction. The most common uses of PCA are to explore a data set for structure and grouping and to reduce high dimensionality data to a lower dimension. Reducing the dimensionality of a large dataset by PCA can be a very useful technique. The transformed data can have a significantly lower dimension, but still contain a very large amount of the variance contained within the data, which is important for developing learning algorithms and when making predictions. Features can grow rapidly, which also requires the amount of training data to grow as well. It is often not possible to obtain more training data or is too costly, so to avoid the curse of dimensionality,<sup>13</sup> the size of the feature space must be reduced. Figure 1.9 is an example demonstrating the amount of variance that can be maintained in a smaller number of PCs. The feature vector used for PCA in this case contained 14 features. This plot shows that if the first PC is kept, then 51% of variance will be represented by this single PC. Similarly, if 5 PCs are kept, then 99% of the variance will be contained in the first 5 PCs. So in this case, a feature space of 14 can be reduced to 5, while still maintaining 99% of the variance in the data.

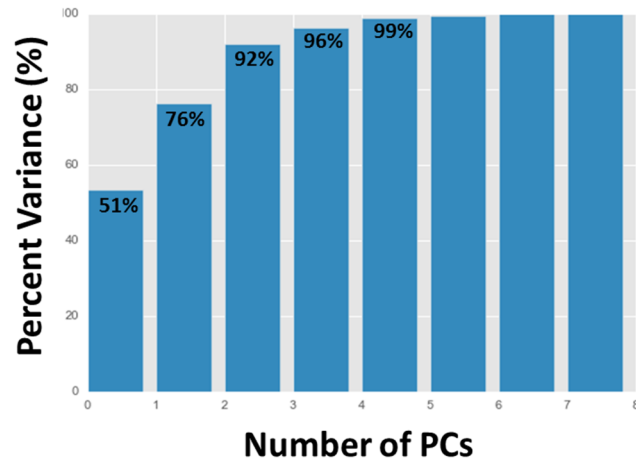


**Figure 1.9** The cumulative percent variance for the number of principal components for a PCA transformation.

Many techniques exist that can learn the structure of a set of data so well that when the model is applied to the data on which the model was built, it correctly predicts every sample. In addition to learning the general patterns in the data, the model also learns the characteristics of each measurement's unique noise. This type of model is said to be overfit and will usually have poor accuracy when predicting a new sample.<sup>14</sup> It is tempting to use the entire data as the training set; however, that results in a model that overfits to the training data, and is unable to be generalized to new data. The problem of overfitting is exacerbated with classifiers which have a large number of parameters.<sup>15</sup> A commonly used technique to better validate the prediction accuracy of a model is k-fold cross-validation. When this technique is utilized, the data set is split into training and test sets for each k-fold iteration, where the training and test sets are different for each fold. In this manner, a prediction accuracy is obtained for each fold from the prediction outcomes on the test set, which can then be averaged to obtain an overall prediction accuracy. Figure 1.10 illustrates

the process of k-fold cross-validation using 5 folds. This example is generic and does not define the size of the training and test set, but in a real example the size of these are defined with values such as a training size of 70% and a test size of 30%. For each fold show in this example, it can be seen that a different training and test set are chosen and a prediction accuracy is determined for each fold. This example purposely shows that the range of accuracies can vary widely, with in this case, a minimum of 73% and maximum of 93%. Without using k-fold validation these are the results that one would obtain if choosing just that specific training, and test sets from the data and would give an inaccurate representation on how the model may perform on new data. The average prediction accuracy for this model using 5-fold cross-validation is 84%, with a standard deviation of 6.7%.

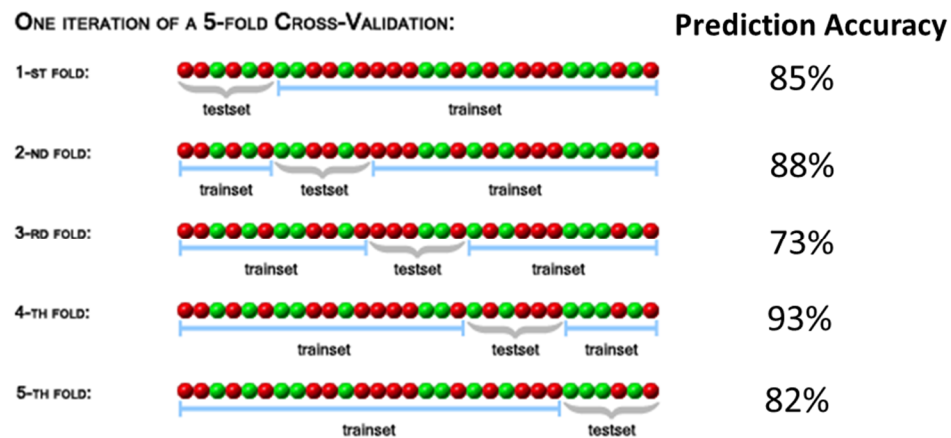


**Figure 1.10** Illustration of k-fold cross-validation using 5 folds. Each row represents a separate prediction performed on that specific testing and train set.

## 1.4 State-of-the-Art: Electronic Nose and Graphene Sensors

The types of sensors used in an e-nose are not necessarily limited to those providing a direct electrical output, but rather those in which the sensor response is some measurable phenomenon that can be converted into an electrical signal. More important than the type of sensor used is if the sensor can be utilized in an array format. The diversity needed for an e-nose is made possible by creating a cross-reactive array, which contains multiple broadly responsive sensors. The various types of sensors can be largely grouped into sensors that produce a direct electrical change (e.g., voltage, resistance, current, capacitance), and sensors that transduce physical change, temperature change, or optical changes into an electrical signal of some form. The following is a brief summary of various approaches of novel materials and devices for sensor applications.

(i) Silicon nanowire field effect transistors (SiNW FETs) have been used for selective detection of gas phase compounds. The SiNW FETs are individually functionalized by various molecular layers containing carboxyl, phenyl, and methyl functional groups, providing a variety of electron-donating and electron-withdrawing functionalities. The extracted features from each modified sensor output include the voltage threshold, hole mobility, subthreshold swing, and on-current, which are derived from the measurement of the drain-current versus gate-voltage. These features are used directly as inputs to an artificial neural network (ANN) model for classification of the target compounds.<sup>16</sup>

(ii) Carbon nanotubes (CNT) vapor sensors has shown great promise, with high sensitivity conferred by the small dimensionality and exceptional electronic properties of the CNT. This type of device relies on the change in resistance of the CNT upon exposure to

an analyte. One approach used to create a cross-reactive array based on CNTs is to functionalize each element with single-stranded DNA. In this work, four different DNA oligomers were used to create a sensor array capable of detecting target analytes in backgrounds of volatile interferents and discriminating between highly similar molecules.<sup>17</sup>

(iii) Carbon black-polymer composites have been used fairly extensively for chemical vapor sensing. Carbon black is combined with a polymer at a certain weight ratio to create a conductive composite, and is typically deposited over a pair of electrodes. Upon exposure to chemical vapors, the conductive film swells, causing an increase in film resistance due to increased distance between carbon black particles. Arrays of carbon black-polymer composites vapor sensors have been created by utilizing a variety of organic polymers with varying properties that have been selected to provide a broad responsivity. These arrays have shown excellent discrimination ability when used with proper pattern recognition methods and have been compared to mammalian olfaction.<sup>18</sup>

(iv) Metal oxide semiconductor (MOS) materials used in a chemiresistor format are widely used sensing materials in e-nose design and can be found commercially from companies such as Alpha-MOS and Applied Sensor.<sup>4</sup> These sensors also rely on a change in the resistance of the sensing material, but this change occurs under different conditions and mechanisms. The target gas interacts with the surface of the metal oxide film, which results in a change in the carrier concentration of the semiconducting film and ultimately serves to alter the conductivity.<sup>19</sup> These sensors have shown to be very sensitive when larger surface areas are used, but can lack selectivity. Selectivity can be gained by adding catalytic metals to the film and varying the operating temperature. MOS sensors have been applied extensively

in the food industry for the analysis of products such as meats, fish, dairy, grains, fruit, and beverages.<sup>20</sup>

(v) Surface acoustic wave (SAW) devices have long been popular for vapor phase gas sensing. These devices are completely reliant on a polymer coating, which is modified in the presence of a chemical compound, causing a modification to the reference frequency of the device. Since these devices are reliant on the polymer properties, statistical methods can be used to attempt to determine the similarity of polymer coatings by analyzing their solvation parameters according to the linear solvation energy relationship. In one specific example, data mining approaches are used to select optimal polymers from a group of 22 polymers used to coat SAW devices for vapor phase detection of TNT and DNT in the presence of interferent background compounds.<sup>21</sup>

(vi) A sensor technology related to SAW sensors are quartz crystal microbalance (QCM) sensors. QCM sensors also rely on the absorption of gas molecules into a polymer coating applied to the device, which in-turn causes a shift in frequency from a baseline resonant frequency. The polymer coatings used for a QCM array can be similar, if not identical, to those used for SAW and carbon black sensors.<sup>22</sup>

(vii) A mass-based sensing system based on a microfabricated silicon cantilever array translates physical and chemical processes into nanomechanical motion of a cantilever. The motion of the cantilever is represented by a signal magnitude based on its overall movement. In this example, eight cantilevers are contained in the array, each with a single polymer coating or a combination of the single polymer coatings. Signal values at five points in time are extracted from each of the eight sensors; the combined features are reduced by PCA to

obtain a reasonable dimension feature vector, which is then used as an input to an ANN for learning and classification.<sup>23</sup>

(viii) Fluorescent polymers have become popular for sensing of chemical compounds due to their fluorescence amplifying effect, which can produce dramatic changes when exposed to low concentrations of chemical compounds. In this approach, glass beads were coated with five fluorescent polymers with distinct spectral emissions and packed in a flow cell. Water was passed over the beads while continuously monitoring the fluorescence intensity of each section of beads with separate spectrometers. The array was challenged with 17 different analytes, including explosive and explosive-related compounds. The array displayed excellent ability to discriminate between explosives and explosive-related compounds such as TNT, DNT, RDX, DNB, and tetryl. Although this work used water as the carrier of the analytes, this same idea could be used directly in the vapor phase.<sup>24</sup>

(ix) An additional fluorescent based sensing material that can be used for array-based sensing is quantum dots (QD), also known as nanocrystals. In terms of fabrication and deposition, they are similar to polymers and are usually contained in a solvent solution. They can be deposited into solid-state films on their own or combined with non-fluorescent polymers to form a composite. Recently, QD polymer composite films were created in a cross-reactive array by ink-jet printing five composite films, each with a different composite polymer. The fluorescent QD array was tested against 14 functionalized benzenes and 14 compounds related to security concerns, and displayed excellent discrimination ability.

(x) Cross-reactive colorimetric arrays are based on a chemically diverse range of chemically responsive dyes, where the color change of each dye is monitored over time. This approach converts olfactory-like responses to a visual output, which is monitored with

a flatbed scanner to convert the image into digital data that can be further processed. The dyes are of three primary types used to target different types of reactions: metal-ion containing dyes, pH indicating dyes, and dyes with large permanent dipoles. These colorimetric arrays have successfully been able to discriminate between various targets such as beers, soft drinks, and VOCs.<sup>25,26</sup>

Graphene has been used in many different chemical and biological sensing applications, but still remains to be actualized in a cross-reactive array for applications such as an electronic nose. Graphene has certainly been used for chemical vapor sensing, but most of the shortcomings have revolved around modification schemes to create multiple sensors on a single substrate in order to increase selectivity. The only reported case of a graphene-based sensor array uses reduced graphene oxide as the sensing material and creates an array of sensors across the reduced graphene oxide film due to the irregularity across the film.<sup>27</sup> This approach is not an appropriate way to create a sensor array and does not contain any cross-reactivity between sensors. Furthermore, this work is very prone to device-to-device variations since the array is based on irregularities across the film.

Schedin et al. demonstrated, for the first time, the detection of individual gas molecules adsorbed onto graphene.<sup>28</sup> In this groundbreaking work they showed the incredible sensitivity of graphene as a gas sensitive material. Detecting a single molecule is the ultimate level in sensitivity for a chemical sensor. Much of the graphene-based chemical sensor work after this point focused on increasing the sensor selectivity while maintaining the sensitivity. There is often a direct tradeoff between sensitivity, selectivity, and sensor performance, such as response and recovery time. A gain in one of these areas usually results in a loss in one or more of the other areas.

Graphene's surface can be modified by many different methods, and this is often the approach taken to create a sensor or sensor array with increased selectivity. Outside the area of chemical sensing, many cases of graphene functionalization have been reported, with a focus on attempting to induce a bandgap in graphene for use in semiconductor devices. Although these modifications are not intended for sensor applications, the approach of graphene functionalization can be applied to graphene gas sensors for the purpose of extending the sensitivity to certain compounds or overall selectivity.

One potentially versatile modification scheme is the use of single stranded DNA, where the DNA provides sequence dependent chemical recognition capability by varying the length of sequence of the DNA. If changing the sequence of the DNA translates into a gained selectivity of the sensor output response, an almost endless number of sequence combinations could be established. The first reported case of using DNA in this manner used two different coded single stranded DNA sequences to create sensors which display fast response times, complete and rapid recovery to baseline at room temperature, and discrimination between several similar vapor analytes.<sup>29</sup> Additional research done by the same group demonstrated the scalability of this technique by applying additional sequences to the same device type.<sup>30</sup> The detection of nitrogen dioxide (NO<sub>2</sub>) is important for environmental applications because it plays a role in the formation of ozone and acid precipitation.<sup>31</sup> Graphene has been reported to be highly sensitive to NO<sub>2</sub> when the sensor has been treated with an oxygen plasma, which imparts oxygen functionality groups at the graphene edges and on the surface. In this work substantial increase in sensitivity when compared to pristine graphene is reported, with an approximate 8x increase in sensitivity for oxygen treated graphene.<sup>32</sup> In addition, research of NO<sub>2</sub> sensing using graphene grown by

epitaxy on SiC was used to create ultrasensitive sensors with an estimated sensitivity of 0.6 ppt. In this research an annealing process is performed at 120 °C with a carrier gas flow, and improvements in sensitivity were over tenfold when compared to an un-annealed device.<sup>33</sup>

The research described in the previous works predominately focused on increasing the sensitivity of a graphene-based sensor towards a specific compound and largely ignore how it may respond to chemically and structurally similar compounds. One of the first reports of using a single sensor based on graphene to detect and discriminate against multiple compounds was done by Rumyanstev et al., who used an innovative approach to gain further information from the graphene device.<sup>34</sup> In this work, they used a pristine graphene transistor without surface modification and monitored not only the change in resistance of the device upon exposure to seven compounds, but also measured the low-frequency noise spectra of the device simultaneously. The low-frequency noise spectra, also referred to as 1/f noise, displayed characteristic frequency peaks for most of the compounds. This additional information complements the change in resistance values and can effectively be used to help discriminate the individual compounds. Although very innovative, this approach has the drawback of requiring a completely separate measurement of 1/f noise spectra, which can be difficult to perform, especially when it is needed for a compact device or wearable electronics.

## Chapter 2 Graphene and its Use as a Chemical Sensing Material

### 2.1 Graphene Properties

Graphene is a carbon-based material with extraordinary electrical, mechanical, thermal, and optical properties mostly attributed to its 2-dimensional (2D),  $sp^2$ -bonded structure.<sup>35</sup> It is currently one of the strongest known materials, with excellent thermal and electrical conductivity, mechanical flexibility, and optical transparency. Some of these important properties can be seen in Table 2.1. In graphene,  $sp^2$  hybridized orbitals are responsible for bonding in the X-Y plane, which bond to three neighboring carbon atoms. These bonds are very strong and contribute to the mechanical strength of graphene. The remaining 2p orbital exists perpendicular to the plane, contributing one conduction electron per carbon atom. This electron, located perpendicular to the surface of each carbon atom, forms a delocalized electron cloud above or below each carbon ring. The electron clouds from each carbon ring overlap to form a continuous  $\pi$ -orbital system across the graphene layer, which provides its outstanding electrical conductivity. This electron cloud formed above and below the graphene is illustrated in Figure 2.1.<sup>36</sup> Disruption of the graphene lattice by physical or chemical means changes the electronic configuration of the carbon atoms and the overall conductivity.

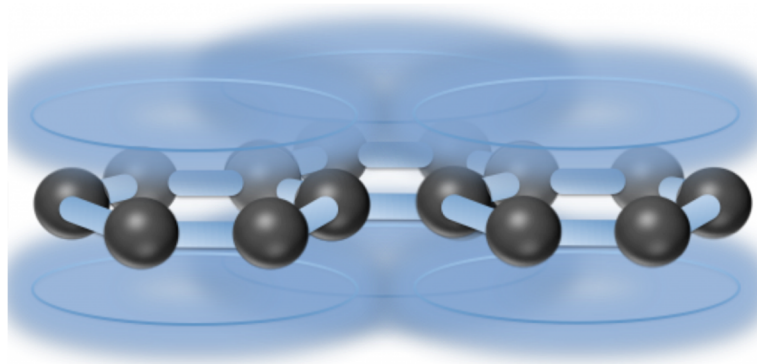


**Figure 2.1** Electron cloud configuration above and below graphene.<sup>36</sup>

**Table 2.1** Mechanical and electrical properties of graphene

Density	0.77 mg/m <sup>2</sup>
Young modulus	0.05 TPa
Carrier density	10 <sup>12</sup> cm <sup>-2</sup>
Resistivity	10 <sup>-6</sup> Ω cm
Electron mobility (at 300K)	20,000 cm <sup>2</sup> V <sup>-1</sup> s <sup>-1</sup>
Thermal conductivity (at 27 °C)	5000 W/mK

Of all other carbon-based materials, carbon nanotubes have been used most extensively for chemical sensing applications,<sup>37</sup> and upon discovery of graphene, it also became a candidate material for chemical sensing. Graphene has a high potential for use in this area owing to its 2D geometry, which provides a surface entirely exposed to its surrounding environment. In this configuration every carbon atom in graphene is a surface atom, providing the greatest possible surface area per unit volume. Therefore, electron transport in graphene is highly sensitive to adsorbed molecular species.<sup>38</sup> Graphene has already been shown to be extremely sensitive to various gaseous compounds and detection

of single gas molecules has been reported.<sup>28</sup> An additional property of graphene which is important for sensor design is its pure carbon makeup. A carbon surface offers much potential for surface functionalization by polymer modification, covalent attachments, bio molecules, and many other chemical processes. Surface functionalization can provide additional sensitivity and selectivity and also can be used as the basis to create cross-reactive arrays.

## **2.2 Graphene Production**

Graphene is produced by a wide variety of methods ranging from mechanical exfoliation to silicon carbide sublimation. The method used to produce graphene has profound effects on its quality, with each method having its respective strengths and differences. The commercialization and realization of any graphene-based device will not only be dependent on the maturity of the device itself, but also the scalability and manufacturability of the device on a mass production scale. This chapters aims to provide an overview of various graphene production methods, and insight into why some methods may be more desirable over others.

### **2.2.1 Graphite Exfoliation**

Graphite is easily sheared into single graphene layers due to the weak Van der Waals forces which keep layers together.<sup>39</sup> The Scotch-tape method uses standard scotch tape to remove layers of graphite from a bulk graphite piece. The tape is repeatedly folded and unfolded to exfoliate graphene layers. Graphene is then transferred to a final substrate such as SiO<sub>2</sub>. This method produces high quality graphene layers but suffers from small,

unpredictable sizes and is often difficult to reproduce. For small-scale research purposes and to probe the fundamental properties of graphene, this method was used. Single graphene layers were able to be isolated and then patterned with metal contacts to create devices. Shown in Figure 2.2 is the exfoliation process of graphene, where scotch tape is used to exfoliate graphene layers from a piece of bulk graphite which are then transferred from the scotch tape to a final substrate.<sup>40</sup>

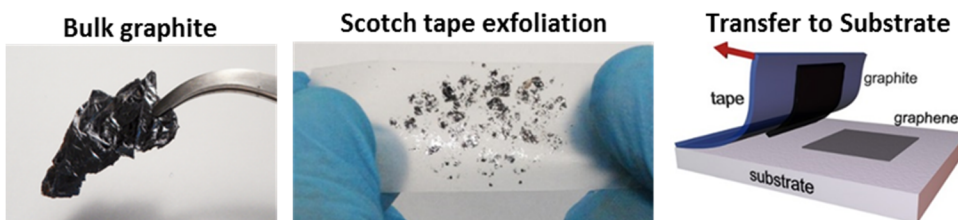


**Figure 2.2** Mechanical exfoliation process of graphene using the scotch tape method.<sup>40</sup>

### 2.2.3 Chemical Vapor Deposition

The deposition of graphene over metal films by chemical vapor deposition (CVD) is one of the most popular synthesis routes, if not the most popular.<sup>41</sup> This technique has the advantages of being a widely available and understood fabrication method and allows the use of large substrates to create large area graphene. This method is fundamentally different than exfoliation, and while it can produce much larger continuous graphene films, the quality is less than that of exfoliated graphene flakes. The CVD process begins by passing a feedstock gas over a catalytic metal substrate (e.g., Ni, Cu) held at an elevated temperature in range of 800 – 1200 °C, depending on the metal substrate. At this elevated temperature the

carbon feedstock decomposes, providing a source of carbon. For the case of a Ni substrate, the carbon is absorbed into the Ni, or if carbon solubility is limited, then  $sp^2$ -carbon formation can occur as a surface process, as in the case of a Cu substrate. After carbon decomposition and absorption or surface formation of carbon, the substrate is moved to a heating zone with a decreased temperature and then to room temperature. A transfer polymer such Poly(methyl methacrylate) (PMMA) is then applied to the metal/graphene substrate and the metal is then etched away with a wet chemical etch solution, leaving the graphene attached to the PMMA. The transfer polymer containing the graphene can now be applied to the final substrate, which is then followed by an acetone rinse to remove the PMMA layer or other organic removal techniques such as reactive plasma treatment. The process of synthesizing graphene on copper foil and its transfer to a final substrate by PMMA acetone removal is illustrated in Figure 2.3.<sup>42</sup>

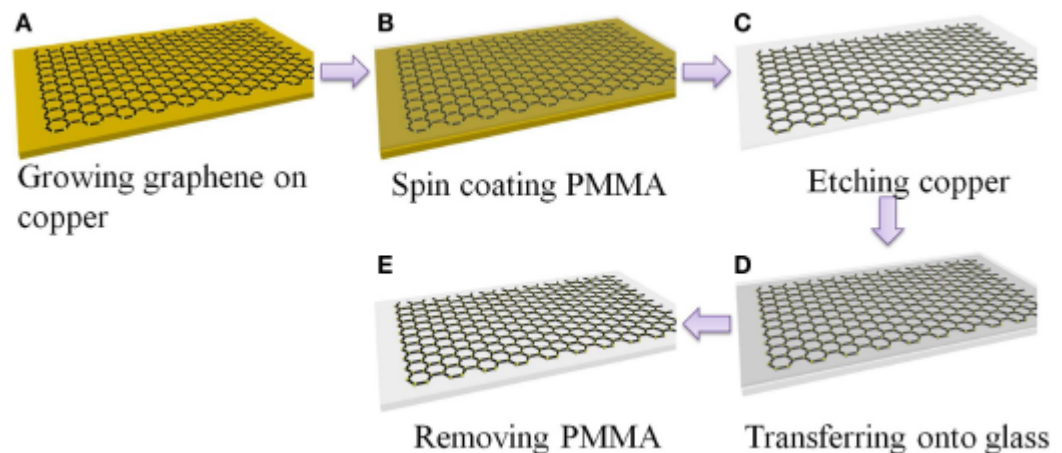


**Figure 2.3** Chemical vapor deposition growth of graphene and transfer process with steps a) synthesis of graphene on copper foil, b) spin-coating of PMMA onto the Cu foil to

protect graphene, c) etching of Cu, d) transfer of graphene/PMMA film onto glass, e) removal of PMMA in acetone.<sup>42</sup>

#### **2.2.4 Epitaxial Growth on SiC**

Graphene can be grown directly on commercially available silicon carbide (SiC) substrates and the process is capable of producing high quality, clean graphene films. The growth process is based on controlled sublimation of silicon from the SiC substrate. A SiC sample is typically heated at temperatures near 1600 °C, resulting in a direct transformation of silicon in the solid phase to vapor phase. When the silicon sublimates, it leaves behind a few layers of nearly free carbon which reconstruct on the surface to minimize bonding energy.<sup>41</sup>

#### **2.2.5 Graphene Oxide**

Graphene oxide is still considered a type of graphene but will not produce nearly the quality of the previously described graphene films. To create graphene oxide, graphite is exfoliated chemically with a strong oxidizer. This creates a solution of single layer flakes typically suspended in water or ethanol. The solution can then be spun onto many different substrates, but in this state is an insulator due to the large number of insulting functional groups created during chemical exfoliation which disrupts the  $sp^2$  bonding. A graphene oxide film can be reduced in an attempt to restore its properties. Reduction of graphene films can be done by a variety of methods but two of the most popular are thermal reduction, performed in a furnace, and chemical reduction via hydrazine vapor.<sup>43</sup>

## 2.2.6 Roll-to-Roll Processing

Roll-to-roll (R2R) processing of high quality graphene is currently the most advanced method of graphene production and is mostly developed for flexible, conductive substrates for displays and a higher throughput manufacturing method. One recent report demonstrates R2R processing of 30" graphene films onto a flexible substrate for transparent electrode applications.<sup>44</sup> Shown in Figure 2.4 is an image of the procedure used in this report and depicts R2R production by attaching graphene on copper foil to a polymer support, followed by copper etching, and finally polymer support release and graphene transfer to a final flexible substrate. This process is very similar to that of CVD graphene but is done in a continuous fashion for application in high volume production.

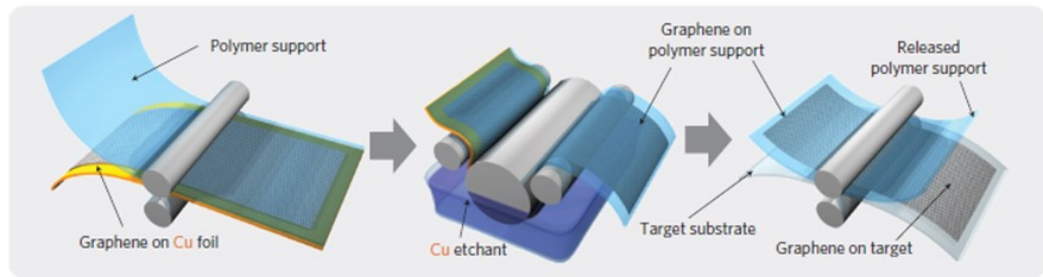


**Figure 2.4** Roll-to-roll production of graphene onto a flexible substrate.<sup>44</sup>

## 2.3 Sensor Design

The sensor design consists of a simple chemiresistor device comprised of a pair of metal contacts deposited onto a graphene substrate, where the substrate is comprised of silicon (Si), thermally grown silicon dioxide ( $\text{SiO}_2$ ), and graphene. The metal contacts are a

series of interdigitated electrodes (IDE) with a specified length, width, and separation. A resistance is established due to the separation of the electrode fingers and resistive properties of the graphene. To operate the sensor a constant bias is applied across the electrodes and a resulting current is measured. When a chemical compound is presented to the sensor surface, the resistance of the graphene is temporarily modified, resulting in a time-dependent change in resistance. Upon removal of the compound from the sensor, the resistance begins to return to its baseline value. Shown in Figure 2.5 is an illustration of a graphene sensor device, where a chemical compound comes in contact with its surface, producing a change in resistance of the graphene film over time.

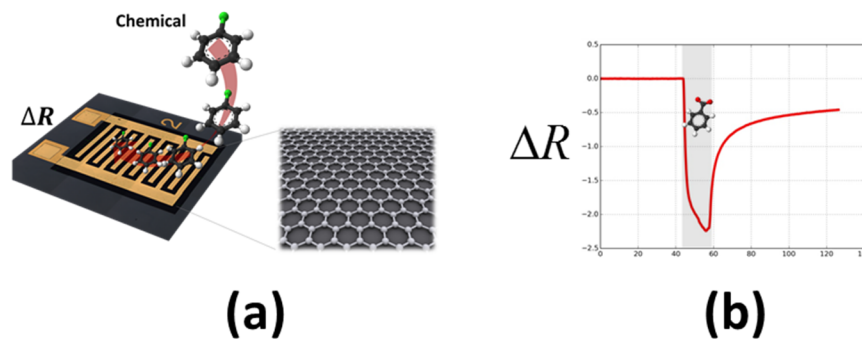


**Figure 2.5** a) Sensor design consisting of interdigitated electrode contacts deposited on an Si/SiO<sub>2</sub>/Graphene substrate and b) typical time-dependent change in resistance of the graphene chemical sensor.

## 2.4 Sensor Fabrication

All sensor devices used throughout this work were fabricated from purchased Si/SiO<sub>2</sub>/graphene substrates. The graphene was produced through CVD and physically

transferred to the Si/SiO<sub>2</sub>. 4" single layer graphene substrates were purchased from Graphenea (Cambridge, MA) and cleaved into approximate 1.3 cm x 1.3 cm pieces using a diamond scribe. Other graphene samples consisting single layer, single double layer, and few layer films were purchased from Graphene Supermarket and come pre-cleaved as 1 cm x 1 cm pieces (Calverton, NY) and were used as noted. Pressurized nitrogen was then used to remove any particles on the surface before photoresist application. AZ nLOF 2035 negative photoresist was then applied to the sample and spun at 500 rpm for 4 s, followed by a 30 s spin at 3000 rpm. A laboratory swab wetted with acetone was then used to remove the edge bead formed around the perimeter of the sample. The sample was then soft baked on a hot plate for 60 s at 110 °C to remove residual solvents. A photolithography mask of the IDE design was then used to expose the photoresist for 4 s. A post exposure bake was then performed for 60 s at 100 °C. The exposed sample was then developed in AZ 300 MIF developer for approximately 35 s or until the pattern visually appeared. Following photoresist development, the sample was rinsed in deionized water and dried with pressurized nitrogen. The patterned sample was then mounted to a Si carrier wafer and loaded into a Temescal BJD-1800 electron beam evaporator where a layer of Ti/Au (25 nm/300 nm) was deposited once an appropriate base pressure was achieved. Following metal deposition, metal lift-off is achieved by soaking the sample in an acetone bath for ~2 hrs. After the metal patterned sample was rinsed with deionized water and dried, it was mounted in a leadless chip carrier and wire bonded. The described fabrication steps are visually shown in the process diagram in Figure 2.6 and images of graphene substrates, photolithography design, and a completed device are shown in Figure 2.7.

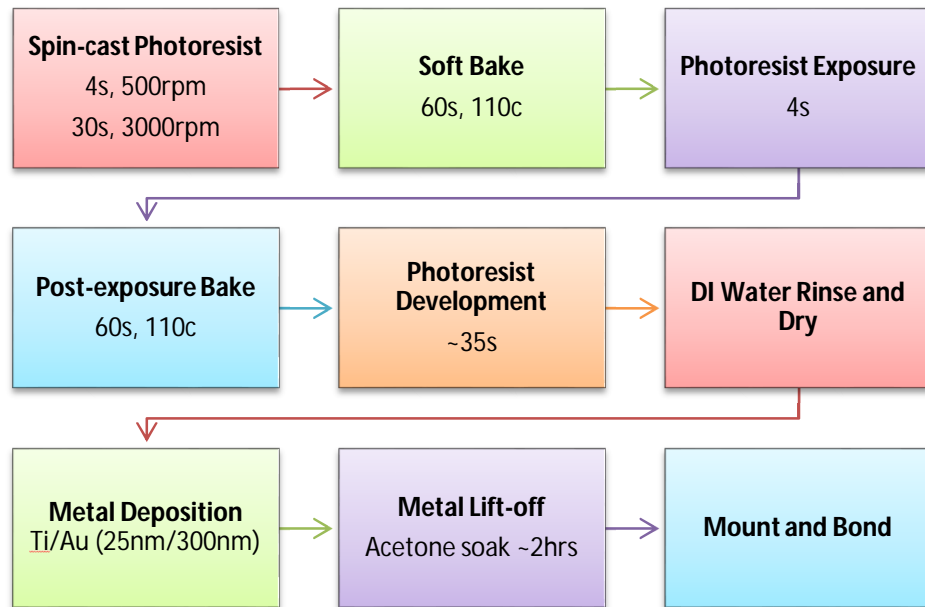


**Figure 2.6** Graphene sensor fabrication process steps.

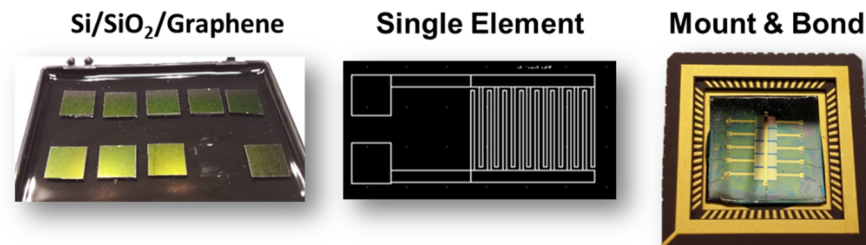


**Figure 2.7** a) Cleaved graphene pieces, b) photolithography pattern for a single device, and c) completed sensor wire bonded in leadless chip carrier.

### 2.4.1 Fabrication Issues

Two main fabrication issues were encountered: 1) the lifting of the deposited metal from the substrate during wire bonding and 2) unintentional removal of the graphene during photoresist development. Graphene produced through CVD is not directly grown on the

SiO<sub>2</sub>, but rather by a transfer process using a carrier polymer. Given these reasons, it is not inconceivable that the bond strength between the graphene and SiO<sub>2</sub> is weak relative to the bond between the Ti/Au layer and graphene. During wire bonding the first bond contacts directly to a Ti/Au bonding pad and the second bond to the inner perimeter of the LCC. When transitioning from the first bond to the second, the tension can cause the metal pattern to lift from the surface, or in some cases be completely removed. Figure 2.8 contains SEM images detailing the lifting of the metal IDE during wire bonding with a) gold wire bond attached to a bonding pad that has lifted off of the surface, b) IDE lifting from the surface and removing the graphene layer, and c) complete removal of the metal IDE and underlying graphene. This issue is particularly challenging when working with FLG. The many graphene layers are still able to be easily exfoliated and the metal deposited on the top most graphene layer promotes this exfoliation during the bonding process. An image taken with a confocal laser scanning microscope of FLG is shown in Figure 2.9 and clearly shows the removal of the majority of the electrode pattern and underlying graphene in a very sharp, defined pattern. In this case, it still appears that the graphene is completely removed even though this is FLG, further indicating that the bond between the graphene and the SiO<sub>2</sub> substrate is weak.

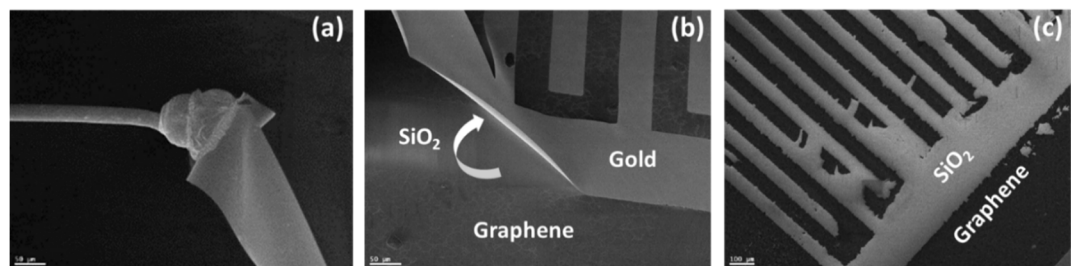


**Figure 2.8** SEM images of a) wire bond attached to lifted metal pad, b) IDE pattern lifting from the substrate, and c) complete removal of metal IDE.

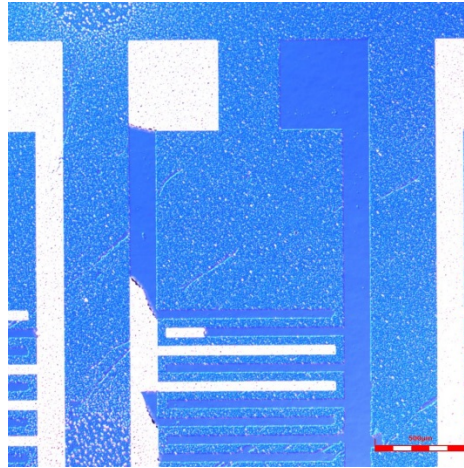


**Figure 2.9** Confocal laser scanning microscope image showing the removal of the metal contact pattern from few-layer graphene.

During the photoresist development step performed for lift-off, the developer removes the portions of the photoresist which were masked from the UV light until it reaches the underlying layer. The development time is typically determined by manufacturer guidelines and experimentally, which takes into account the actual temperature and humidity. Shown in Figure 2.10 are SEM images of a graphene sample that has been patterned for metal deposition, but instead of depositing the metal, the photoresist was stripped with acetone, revealing a deteriorated surface. This developer, along with many others, consists of water and Tetramethylammonium hydroxide (TMAH). No obvious cases of interactions between TMAH and graphene have been reported.

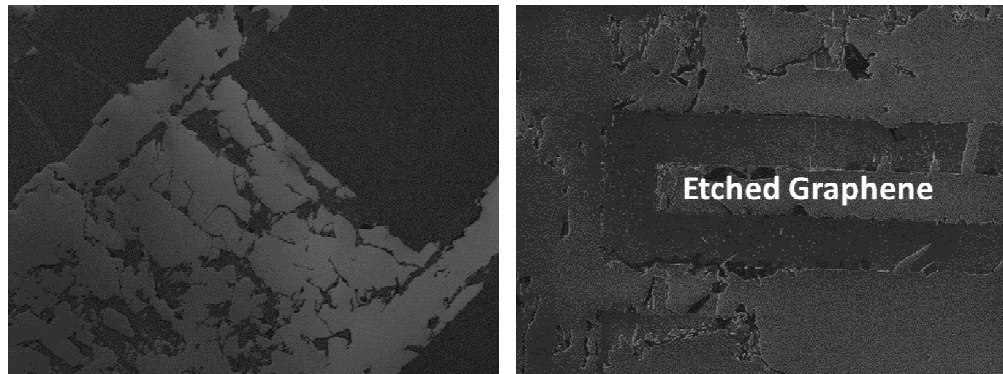


**Figure 2.10** SEM images of graphene appearing to have been unintentionally etched during photoresist development.

This effect was further investigated by optical spectroscopy and Raman spectroscopy during the fabrication process. Following photoresist development for metal lift-off, the sample was imaged with an optical microscope to look for damage. Shown in Figure 2.11a is the surface where metal deposition will occur and clearly shows a disrupted film. The previous SEM images appear to show an etched film, but in this image the film appears to have lifted from the  $\text{SiO}_2$  surface, and in some areas, folded on top of itself, creating wrinkles. Figure 2.11b shows the same device after metal deposition and liftoff, where the same features in the previous image are visible in the metal film. It is important to note in Figure 2.11b that the graphene under the photoresist during photoresist development is not damaged and can be seen in the magnified view of Figure 2.11b. From a manufacturing standpoint this is an issue that would need to be addressed, but in the case of this sensor, the graphene makes good electrical contact with the metal and the graphene between electrodes is undamaged.

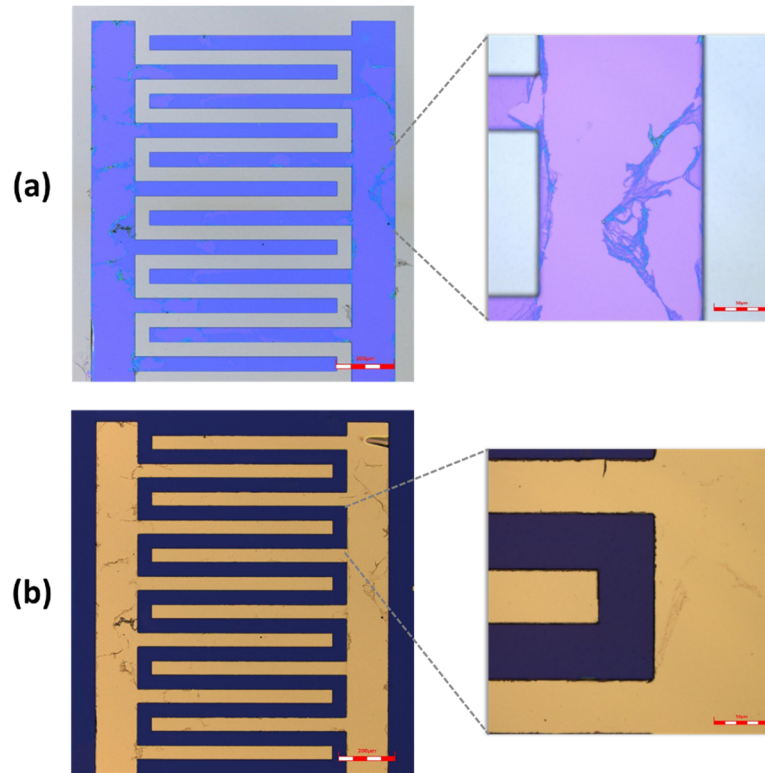


**Figure 2.11** Microscope images of processed graphene device a) before metal deposition and b) after metal deposition.

To confirm that the graphene was indeed removed during photoresist development as shown in the previous figures and that the graphene between electrodes was intact, the Raman spectra of three different regions were measured. Three measured Raman spectra are shown in Figure 2.12: 1) where graphene appears to be removed after photoresist removal, 2) area which appears undamaged after photoresist removal, and 3) between the metal electrodes after metal liftoff. The spectra of the apparently removed graphene area shown in blue confirms no graphene is present due to the lack of any characteristic peaks. The spectra for the undamaged area and the area between metal electrodes are characteristic Raman spectra for graphene and only differ by a small change in the D-peak.

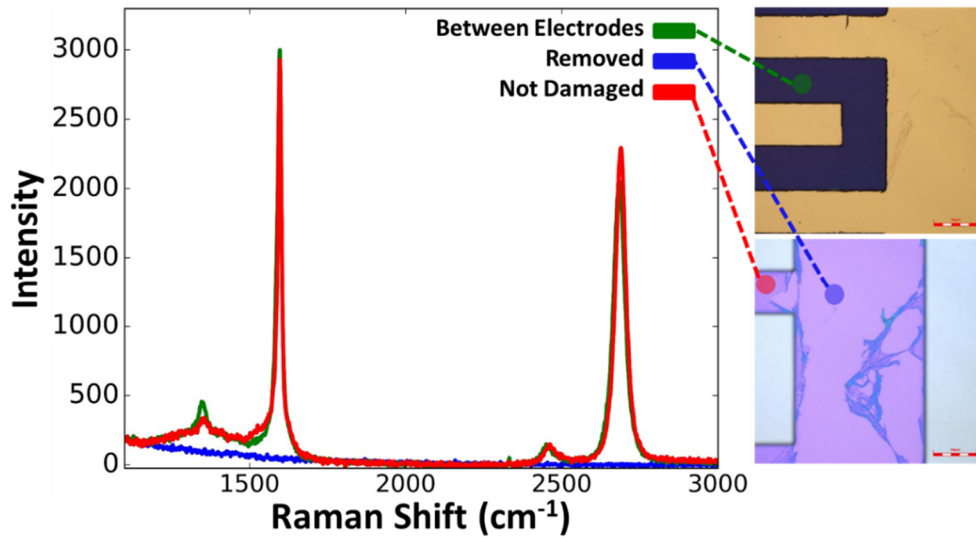


**Figure 2.12** Raman spectra of processed graphene device taken before metal deposition and after metal deposition.

## 2.5 Gas Sensing Setup

Once the graphene sensor is mounted and wire bonded in the LCC, it is ready to be placed into the testing fixture used for experimental gas sensing. The testing fixture is shown in Figure 2.13 with its various components. It consists of a printed circuit board (PCB) with a socket matched to the pin layout of the LCC used. A 2" aluminum lens tube cap has been machined to fit around the LCC socket and is adhered to the PCB. The lens tube also has four tapped screw holes which allow a Teflon flow channel to be secured to the PCB. With the LCC placed in the socket and the Teflon gasket and the flow cell secured with the four screws, a seal is created, allowing access to only the cavity of the LCC where

the sensor is located. An inlet and outlet port are used to introduce a gaseous chemical vapors across the sensor surface.

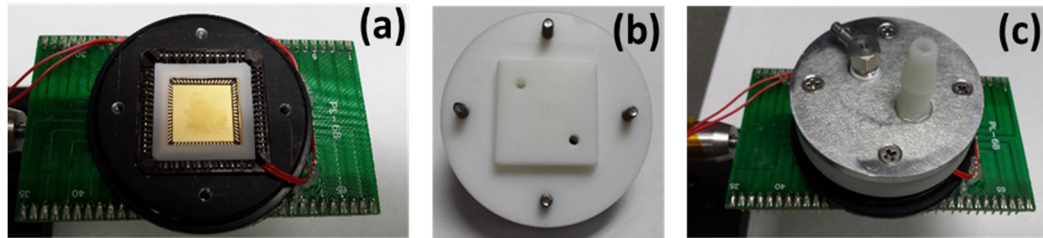


**Figure 2.13** Gas Sensing test fixture showing a) LCC socket with LCC and Teflon gasket, b) bottom of Teflon flow cell, and c) top of Teflon flow cell.

The PCB provides connections from the internal sensor cavity to the outside world. For a single sensor measurements, the resistance is measured using a Keithley 2450 source meter. This measurement instrument is capable of sourcing a current or voltage while measuring the resulting voltage or current, respectively. The Keithley 2450 is shown in Figure 2.14a. The Keithley 2450 is only capable of measuring a single channel and would require multiplexing to measure multiple channels. When multiple channels are needed, as in the case of a sensor array, a United Electronics Industry (UEI) data acquisition cube was used (Shown in Figure 2.14b). The UEI unit was equipped with two UEI AI-222 resistance measurement cards. Each AI-222 card provides 12 fully differential analog input channels with 24-bit resolution and an input resistance range of 0 – 40 k $\Omega$ , and is capable of collecting measurements at a maximum of 100 Hz.

For each measurement, the resistance is continuously measured over a specified interval. Figure 2.15 illustrates a typical sensor response curve with three distinct regions

consisting of a baseline, sample, and recovery period. The response exhibits a characteristic exponential-like rise which reaches a steady-state maximum change in resistance, followed by a similar exponential-like decay as it recovers back to towards the baseline resistance value.



**Figure 2.14** a) Keithley 2450 source meter used for single device measurements and b) United Electronics Industry data acquisition cube.

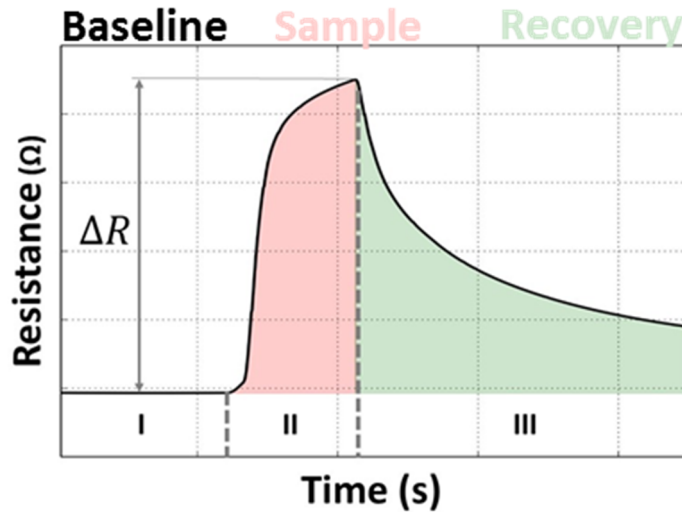


**Figure 2.15** Typical sensor response showing change in resistance for baseline (I), sample (II), and recovery (III) regions.

The response of the chemical sensor is influenced by the design of the entire gas system including the temperature, flow cell volume, and flow rate. It was experimentally determined that certain response ranges exist for the given flow cell being used. This was determined by testing a sensor against a single compound under the same conditions while varying the flow rate. Shown in Figure 2.16 is a plot of a graphene sensor in response to chloroform vapor introduced to the sensor at various flow rates ranging from 1 mL/min to 50 mL/min. A fairly distinct group can be observed for the flow rates 50 mL/min, 40 mL/min, 30 mL/min, and 20 mL/min. These four response curves have a sharp peak that occurs almost immediately after the introduction of the chloroform vapor, where it reaches its maximum value then begins to decay. In this case, the flow rate is most likely too high, causing the most highly concentrated portion of the vapor to pass over the sensor before it has adequate time to respond. This can also be seen in the recovery portion of the response when the vapor is removed and air begins to flow again. At 10 mL/min the shape of the response takes on a completely different shape and a slight decay can be noticed at the introduction of the vapor. As the flow rate continues to decrease the response continues to approximately reach the maximum response value, but takes on more shape during sampling and recovery. This continues until 3 mL/min where the maximum value of the response begins to decrease significantly and the time delay between vapor introduction and the beginning of the response becomes larger. Choosing a flowrate is a trade-off between maintaining a reasonable time between when the vapor begins and when the response begins, and obtaining enough of the kinetic information in the sensor response. The start and stop points of the response are important for proceeding data analysis steps which queue off of these points to determine where to look for certain features. For this type of

sensor and the design of the flow cell, flow rates between 5-10 mL/min appear to be appropriate. An additional consideration when choosing a flow rate is if dilution will be used to test concentration dependence. For instance, diluting a total flow rate of 5 mL/min to 1% saturated vapor would require a dilution stream with a flow rate of 0.05 mL/min, which is not reasonable for a mass flow controller to maintain accurately and consistently.

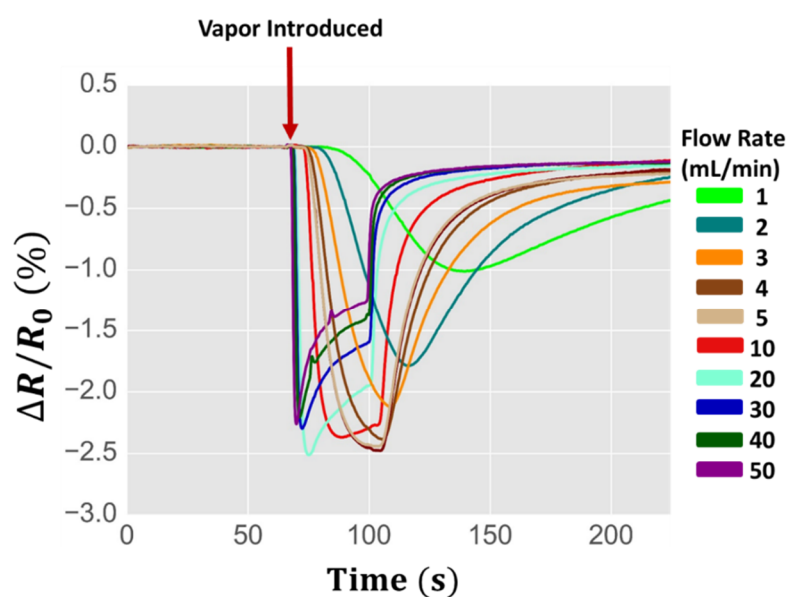


**Figure 2.16** Time-series plot of a graphene sensor exposed to various flow rates of chloroform vapor ranging from 1 mL/min to 50 mL/min.

Generating and supplying chemical vapors of many different chemical compounds at controlled rates and concentrations is typically accomplished by methods such as headspace sampling, diffusion method, permeation method, bubbler method, and sampling bag method.<sup>4</sup> Each method has its strengths and weaknesses, usually revolving around contamination potential, desired concentration levels, and design complexity. When

considering a vapor generation system capable of producing many compounds, the issues associated with contamination quickly arise. In the case of this dissertation, two methods were used; the headspace and bubbler methods.

Shown in Figure 2.17a is a bubbler system with the graphene sensor flow cell connected to the top of a Teflon manifold. In this system, a carrier gas, such as air or nitrogen is passed through a vial containing the liquid form of the compound. A fritted alumina solvent filter lies in the bottom of each vial, where the carrier gas is forced through the porous material, creating very small bubbles which travel through the solvent. The generated vapor is then passed through chemically resistant tubing to a 16-input, low-volume Teflon manifold, where each input is connected with a PEEK check-valve to prevent contamination. Each vial bubbler is addressed by means of an Ethernet controlled relay switch and Teflon mixing valves constructed of low-volume Teflon ports and solenoid valves. In this manner, each bubbler vial can be addressed electronically and allows for the process to be automated. The carrier gas supply for both the vial bubblers and for a dilution line input are precisely controlled by digital mass flow controllers (MFC).

The other vapor generation and sampling system used throughout this work is a variation of a headspace system and can be seen in Figure 2.17b. This system uses MFCs, smart motors, and an electromagnetic capper to automatically uncap a vial containing each compound and introduce the sensor to the headspace contained within the vial. Two MFCs are used; the first is connected to a vacuum pump and is used to draw air across the sensor from the input nozzle; the second is connected to compressed air and is used to dilute the sample flow. The sensor head and sample vial tray are both mounted to smart motors, allowing their position to be electronically addressed with precise control. The sensor head

is mounted to a vertical smart motor and is used to lower the input nozzle into the headspace of each vial. The sample vial tray is mounted to a rotating smart motor and is used to select the desired vial. Before the vial is moved into a position just below the sensor nozzle, an electromagnetic capper removes a metallic cap from the vial to be sampled. The opened vial is then moved to the position just below the sensor nozzle and the sensor is lowered into the vial headspace, where it samples the generated headspace for a specified amount time then moves back to its original position and the vial is capped. Both the bubbler and headspace systems are controlled over USB and Ethernet by custom Python-based software.

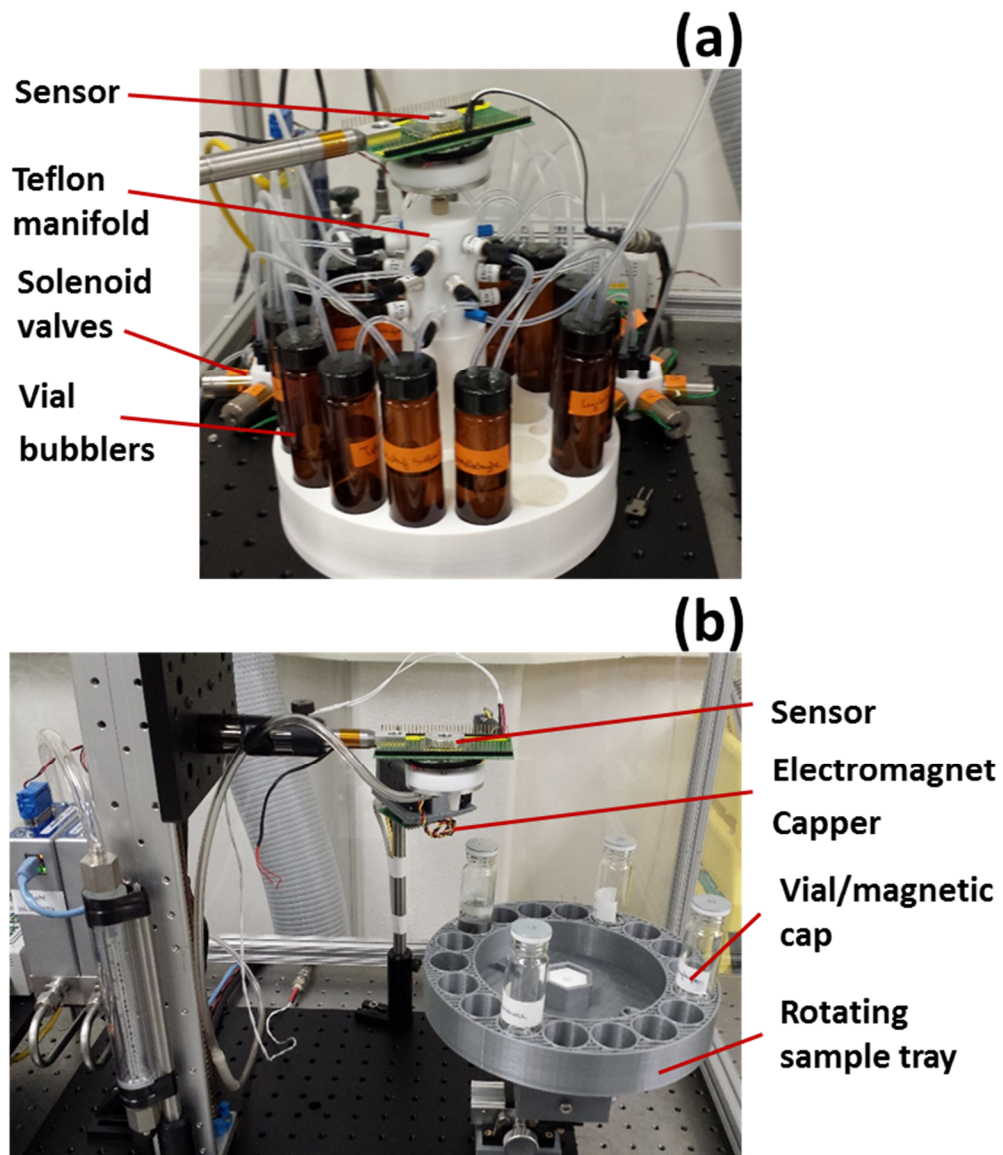


**Figure 2.17** Vapor generation and sampling systems utilizing a a) bubbler method and b) headspace method.

The sampler software takes a user input CSV file specifying the parameters for each measurement. The software then has the ability to choose if the input sample list should be randomized and repeated. For single device measurements, the Keithley 2450 is used and

the input CSV file takes the vial number, compound, baseline time, sample time, recovery time, sample flow rate, dilution flow rate, and device voltage. When multiple channel measurements are needed, the UEI AI-222 resistance measurement boards are used and the input CSV file takes the vial number, compound, baseline time, sample time, recovery time, sample flow rate, dilution flow rate, and selected channels. Throughout execution of each measurement data is collected for the resistance, time, flow rates, temperatures, motor positions, bubbler solenoid state, and other metadata. All data is stored in a universal binary file which is used for subsequent data processing.

## **2.6 Issues and Challenges**

### **2.6.1 Substrate Effects**

To date, a technique used to directly grow or deposit graphene onto the final substrate surface has not been developed, requiring graphene to be produced by other means and transferred to the final substrate. The type of substrate and its condition can have a profound effect on the properties of the graphene film. Quality, cleaning, or other treatment of the substrate prior to graphene transfer is important for the operation and reproducibility of further fabricated devices. Device-to-device variability, though in this case used in a positive manner,<sup>45</sup> can make realization of graphene devices difficult. Wang et al. developed a model to describe the reactivity of the graphene surface based on the surface energy of the underlying substrate.<sup>46</sup> They transferred graphene via CVD grown and PMMA transfer to various substrates with different surface energies and performed Raman spectroscopy on the surface of each sample. They discovered the surface reactivity, represented by the ratio of D-band intensity peak ( $I_D$ ) to the G-band intensity peak ( $I_G$ ), varied with the contact angle of

the surface and a more reactive surface results from a more hydrophilic surface. The results of their findings can be seen in Figure 2.18, which illustrates a plot of surface reactivity versus contact angle for Plasma-cleaned SiO<sub>2</sub>, piranha-cleaned SiO<sub>2</sub>, as-received SiO<sub>2</sub>, aluminum oxide, and octadecyltrichlorosilane surfaces, showing decreasing reactivity when going from hydrophilic to hydrophobic surfaces. In fact, it has been shown for a suspended graphene device, without a substrate in contact with the graphene layer, that no measured response is observed when various chemical compounds are introduced to its surface.<sup>47</sup>

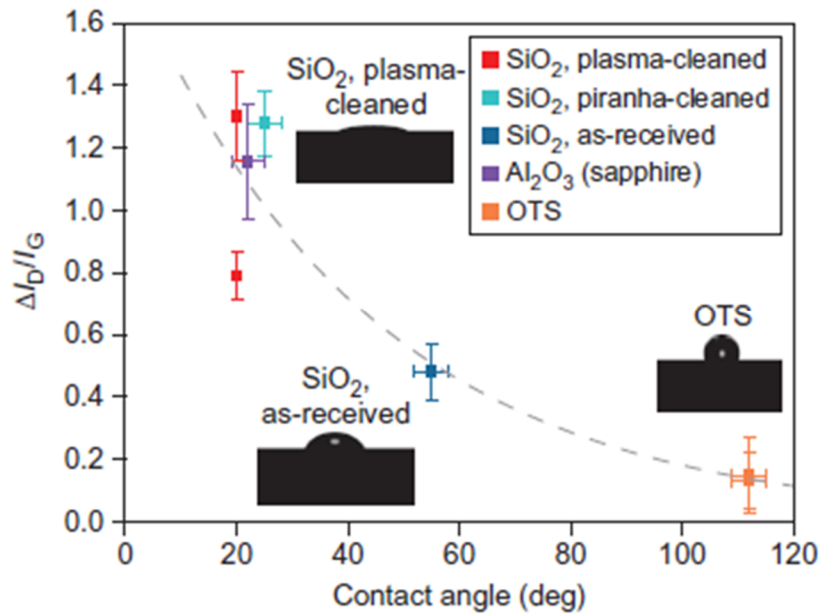


**Figure 2.18** Plot illustrating the effect of different substrates on the surface reactivity of graphene.<sup>46</sup>

## 2.6.2 Noise

Graphene is a unique material system in the context of  $1/f$  noise owing to its 2D nature.  $1/f$  noise, also commonly referred to as flicker or excess noise, is usually found at  $f < 100$  kHz and is now generally accepted that different fluctuation processes can be responsible for this noise in different materials and devices.<sup>48</sup> The 2D structure of graphene allows the entire surface to be exposed to its surrounding environment, making it desirable for chemical sensing applications. The conduction electrons located on the graphene surface are largely responsible for its overall conductivity, and can also be heavily influenced by surrounding conditions such as the presence of a chemical compound or charge impurities from the underlying substrate. These external effects lead to fluctuation in the conduction mobility, and ultimately to modification of the noise level. The ability to change the number of graphene layers allows for the study of noise effects as a function of number of layers. Balandin et al. demonstrated that the  $1/f$  noise dependence on the number of atomic planes in FLG devices can shed light on the physical mechanism of  $1/f$  noise.<sup>48</sup> They showed that the  $1/f$  noise level continues to decrease with increasing thickness of FLG conductors and therefore, for constant area film, noise is inversely proportional to its thickness. This is an important relationship to discover and has great impact when designing and developing devices. In the area of chemical sensing using graphene devices, it has been shown that the vapors of different chemicals produce distinguishably different effects on the low-frequency noise spectra of graphene, providing an additional feature for distinguishing between chemical compounds.<sup>49</sup> The experimental results from this experiment can be seen in Figure 2.19, showing the low-frequency noise spectra for a graphene device while exposed to

tetrahydrofuran, methanol, acetonitrile, chloroform, and open air. A fairly characteristic peak can be observed for each compound, which can be used in addition to the change in resistance of device while exposed to chemical compounds.

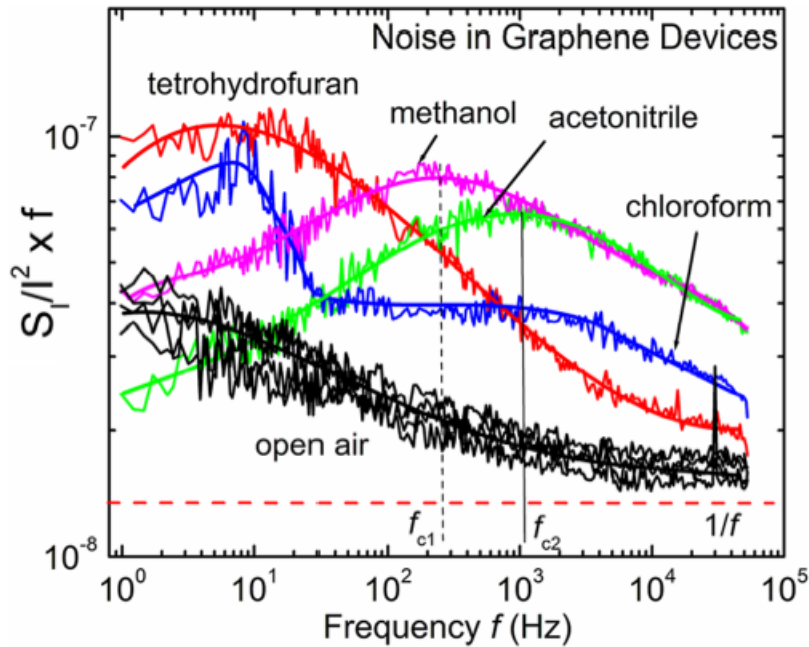


**Figure 2.19** Low-frequency noise spectra of a graphene device while exposed to various chemicals.<sup>49</sup>

### 2.6.3 Fabrication Contamination

Surface contamination by polymer residues is a critical problem, hindering the ability to probe the intrinsic properties of graphene.<sup>50</sup> PMMA is arguably the most widely used polymer for transferring CVD graphene from its metal substrate and is used by many commercial suppliers of graphene. The removal of the PMMA layer can be done by

methods such as an acetone bath or oxygen plasma treatment. Much debate still exists in this area as to whether PMMA residue still exists on the surface and how it affects the graphene properties. Additional processing often required for creating graphene-based devices, such as photolithography for metal deposition or etching, can leave photoresist residues even after cleaning. Residual photoresists left on the surface can modify the graphene's electrical properties such as its mobility and overall conductivity. The most successful technique to remove such residual contaminants has been thermal annealing at temperatures near 400 °C in vacuum.<sup>51</sup> This is dependent on the nature of the device at the current processing step and if it is compatible with this level of temperature.

## Chapter 3 Characterization and Sensor Response

### 3.1 Raman Spectroscopy

Graphene continues to become more and more available from commercial suppliers in various forms. Most commonly, as-supplied graphene is grown by CVD and transferred to Si/SiO<sub>2</sub> substrate where graphene itself can be single-layer graphene (SLG), single/double layer graphene (SDLG), or few-layer graphene (FLG). Raman spectroscopy is a classic technique for probing graphene and determining important properties such as number of layers, presence of defects, and defect density. The Raman spectra of graphite and graphene contains three main bands of interest: the D, 2D, and G bands. The G-band is an in-plane, carbon-carbon stretching mode and exists in sp<sup>2</sup> carbon systems. The 2D-band is a second-order breathing-like mode and is the strongest peak in graphene films with few layers. The D-band is not present in all graphene systems and is only present when a defect exists. A defect is described as any breaking of the symmetry of the graphene lattice, such as vacancy or the attachment of a functional group. The D, 2D, and G bands are found at a Raman shift of 1350 cm<sup>-1</sup>, 2690 cm<sup>-1</sup>, and 1580 cm<sup>-1</sup>, respectively, and are used to identify the number of layers and the extent of defects. The number of layers in the measured graphene film can be found by taking the ratio of the 2D and G peaks, where a ratio of 2, along with a lack of a D-band peak and a sharp symmetrical 2D-band indicate SLG. This relationship is shown in Equation 4 and holds true for lower numbers of graphene layers. Although the 2D-band is always present in graphene, the D-band is not because this band appears when defects in the carbon lattice are present. The level of defects or defect concentration is proportional to the ratio of intensities of the D-band and G-band; this relationship is shown

in Equation 5. Recent research indicates that the lesser reported on D'-band, found near the G-band peak, can be used in conjunction with the D-band to create a ratio to describe the nature of the sp<sup>3</sup>-defects.<sup>52</sup>

$$\text{Number of Layers} \propto \frac{I_{2D}}{I_G} \quad (4)$$

$$\text{Defect Concentration} \propto \frac{I_D}{I_G} \quad (5)$$

Figure 3.1 displays Raman spectra collected for graphite, SLG and double layer graphene.<sup>53</sup> In Figure 3.1a, graphite and SLG are compared, where the main differences are seen in the ratios of the previously described bands and also the shape of the 2D-band. In graphite, the 2D-band contains an extra hump compared to the spectra for SLG; both graphite and SLG exhibit little to no D-band and a very symmetrical G-band. Shown in Figure 3.1b are the normalized G-band Raman spectra for graphite, SLG, and double layer graphene, where the Raman shift increases when moving from graphite to SLG. Similarly, shown in Figure 3.1c is the relative increase in intensity of the G-band when graphene layers are increased.

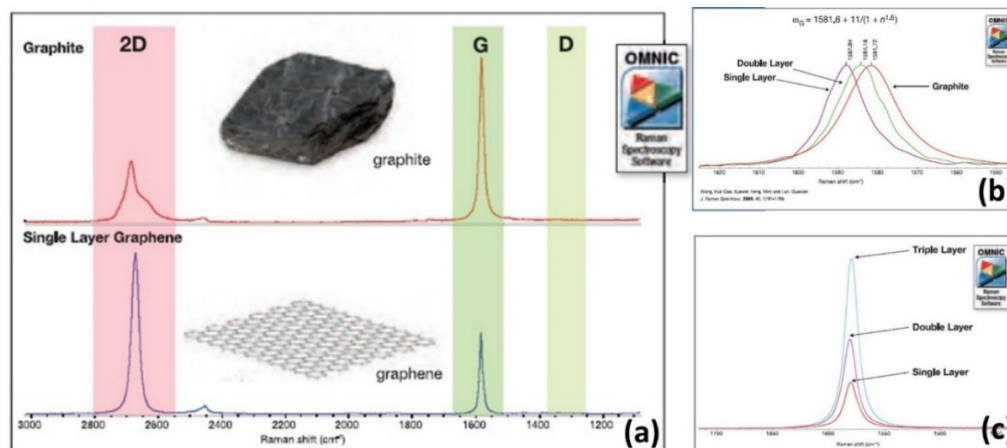


**Figure 3.1** Raman spectra for graphene samples comparing a) graphite and single-layer graphene for all bands, b) shift in the G-band for graphite, single-layer, and double layer graphene, and c) the change in G-band intensity for graphite, single-layer, and double layer graphene.<sup>53</sup>

Experimental Raman measurements were performed using a Thermo Fisher Scientific DXR Raman microscope equipped with a 532 nm laser source. The graphene samples used throughout this work consist of CVD graphene of various layers transferred onto a Si/SiO<sub>2</sub> substrate. Figure 3.2 shows experimentally measured Raman spectra for graphite, SLG, SDLG, and FLG, which were purchased from Graphene Supermarket. The results for graphite and SLG, as compared to those shown in Figure 3.1 which were taken at the manufacturer, match very closely. This confirms that this microscope is capable to perform precise measurements and also confirms that graphene used in our research has high quality. Looking closer at the D-band, G-band, and 2D-band for each material shows differences that occur. In the D-band, a negligible intensity is seen for graphite, SLG, and SDLG, while a large D-band peak is obvious for FLG. The presence of a D-band peak is indicative of defects which could certainly be possible for CVD produced graphene of many

layers. The G-band for each measurement displays an increase in the Raman shift when moving from graphite to SLG, as seen in the previous example.

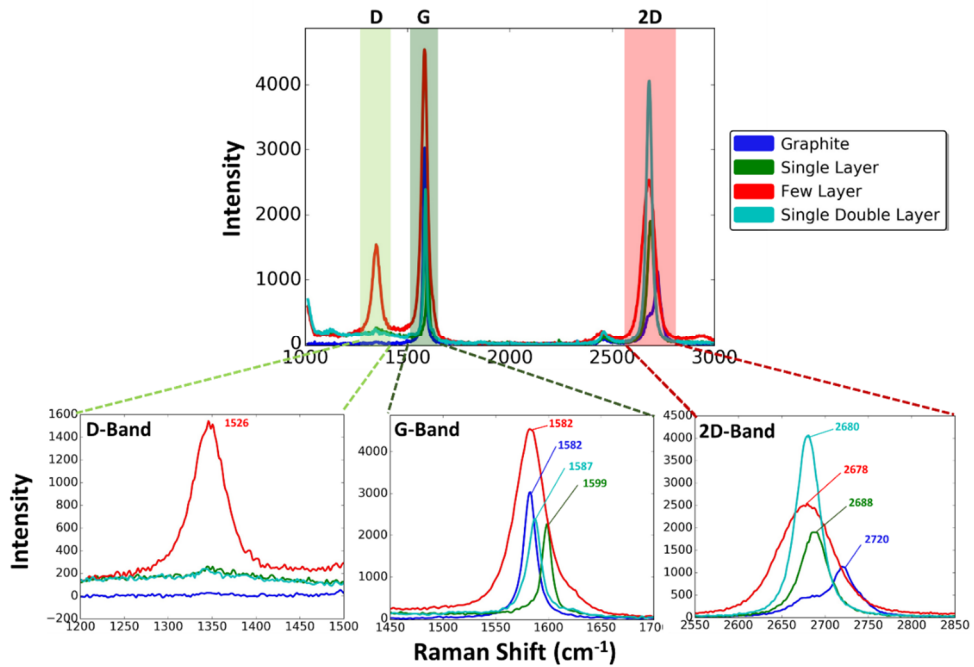


**Figure 3.2** Raman spectra for graphite and Graphene Supermarket CVD single layer, single double layer, and few layer graphene.

Another popular supplier of CVD graphene is Graphenea, which supplies a 4" Si/SiO<sub>2</sub> wafer with SLG. This product has the advantage of being supplied as a wafer so that it can be cleaved or diced into a desired sizes, unlike similar graphene from Graphene Supermarket which comes pre-diced into 1 cm x 1 cm pieces. Three 4" SLG wafers were purchased at different periods and Raman measurements taken on each to look at their consistency. Figure 3.3 displays the spectra for three separate batches of SLG purchased at different dates. Besides some slight differences in intensity of the G-band and 2D-band,

which can be attributed to sample focusing during the measurement, the consistency among different batches is very good. A small D-band peak can be seen that has approximately the same shape and intensity for each batch and may indicate that it could be a substrate effect or due to their method of production.

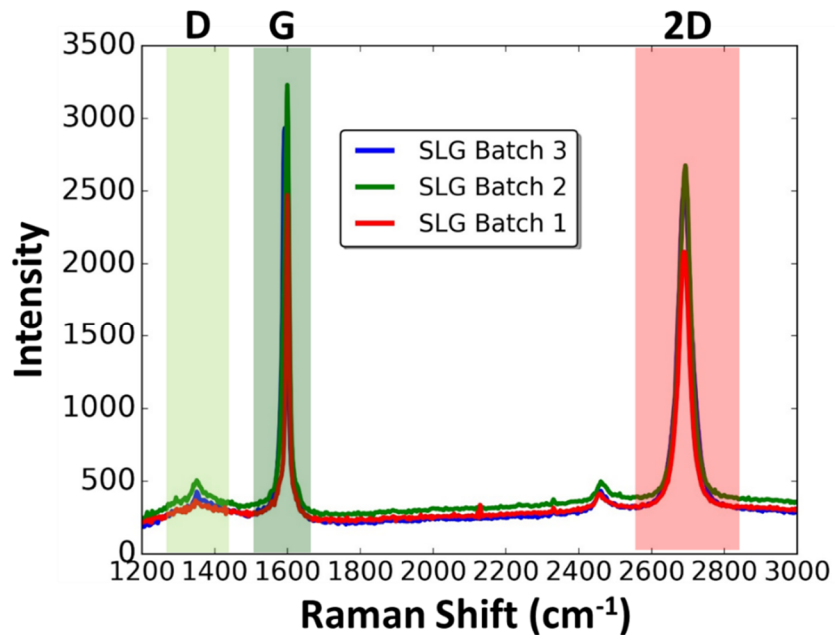


**Figure 3.3** Raman spectra for single layer graphene, purchased from Graphenea, from three separate batches.

### 3.2 Response Voltage Dependence and Linearity

A current-voltage measurement was taken to determine if any contact barriers appear to exist between the deposited Ti/Au contacts and the graphene layer. Shown in Figure 3.4 is a current-voltage measurement with voltage swept from -0.1 V to 0.1 V in 5mV steps.

Excellent linear behavior is shown with no indication of contact barriers at the Ti/Au-graphene interface.

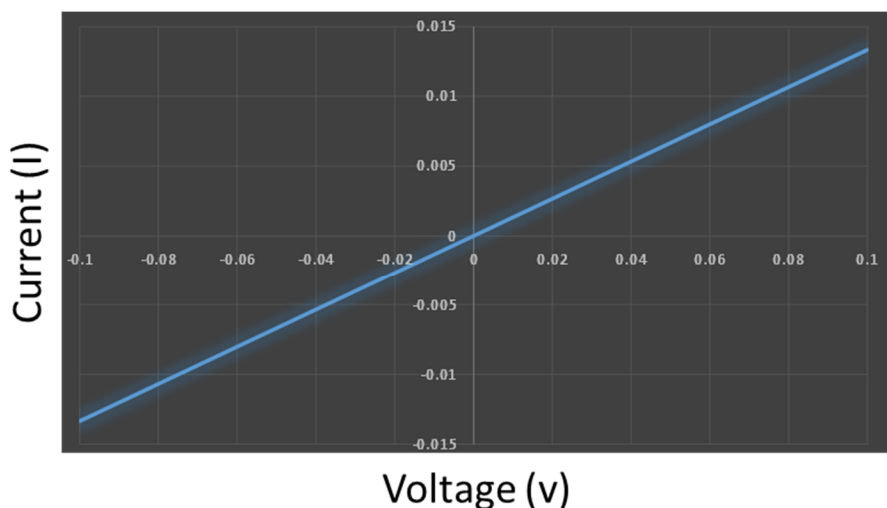


**Figure 3.4** Current versus voltage measurement for graphene sensor

Although the sensor displayed linear current-voltage characteristics, it is worth investigating the response of the sensor to chemical compounds at different operating voltages to determine if a noticeable variation occurs. If a particular voltage or voltage range produced larger responses, it could be difficult to reproduce and device-to-device reproducibility could be difficult. Current-voltage measurements were performed by sweeping the applied voltage from -0.1 V to 0.1 V with a voltage step of 5 mV while exposed to air, diethyl ether, 4-chlorotoluene, acetonitrile, and chloroform. For each of the measurements while exposed to a chemical compound, the sensor was allowed to reach its saturated response value. Shown in Figure 3.5 is the measured resistance value for each

applied operating voltage while exposed to the described chemical compounds. For each measurement the sensor displays a linear relationship between measured resistance and applied operating voltage. Measurements shown for 4-chlorotoluene and chloroform display a negative slope over the voltage range, which is attributed to drifting of the supplied compounds' concentrations.

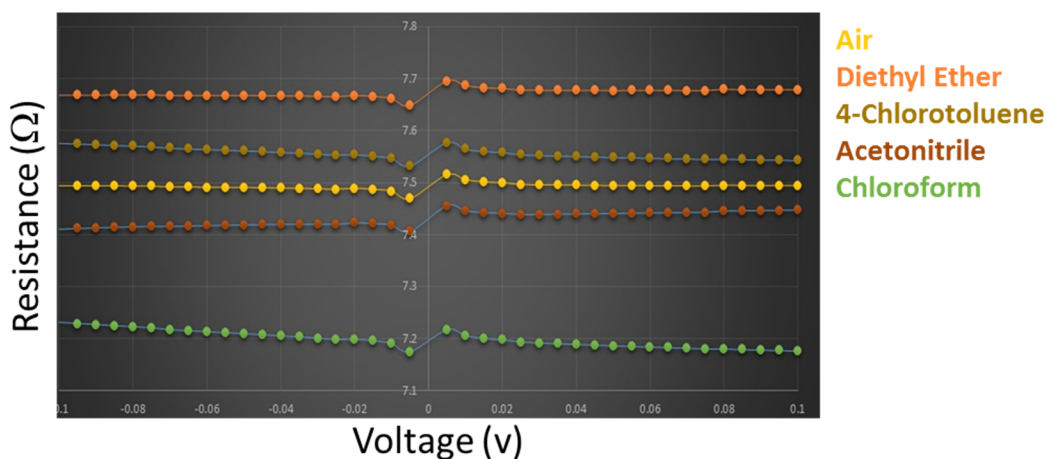


**Figure 3.5** Resistance values while exposed to various chemical compounds for different operating voltages.

### 3.2 Response Stability

The ability of a chemical sensor to maintain a stable response over a period of time is important for reproducible response behavior and sensor longevity. The sensor drift consists of small and non-deterministic temporal variations of the sensor response when it is exposed to the same analytes under identical conditions.<sup>54</sup> A drift in the sensor's response will change the sensitivity and selectivity of the sensor over time, ultimately leading to the

inability to sense compounds and improper recognition and classification of already learned compounds. Shown in Figure 3.6 is the response characteristics of a graphene sensor subjected to acetone, acetonitrile, chloroform, isopropanol, methanol, and toluene for 60 different measurements. The measurements were conducted consecutively under the same experimental conditions and executed in a randomized order. Figure 3.6a shows the time-series plot for each compound and their 60 measurements. It can be seen visually in this plot that the response span for each compound is relatively low, with acetone showing the largest variance. Figure 3.6b displays the maximum change in resistance for each measurement, showing a relatively linear response that is either flat or shows a slight increase in response magnitude over time. The variation in the response magnitude can not only be attributed to potential drift of the sensor, but also to variations in the concentration of the supplied compound vapor. Table 3.1 summarizes the values used to create this plot and numerically indicates that chloroform has the largest deviation in response, while toluene has the lowest.

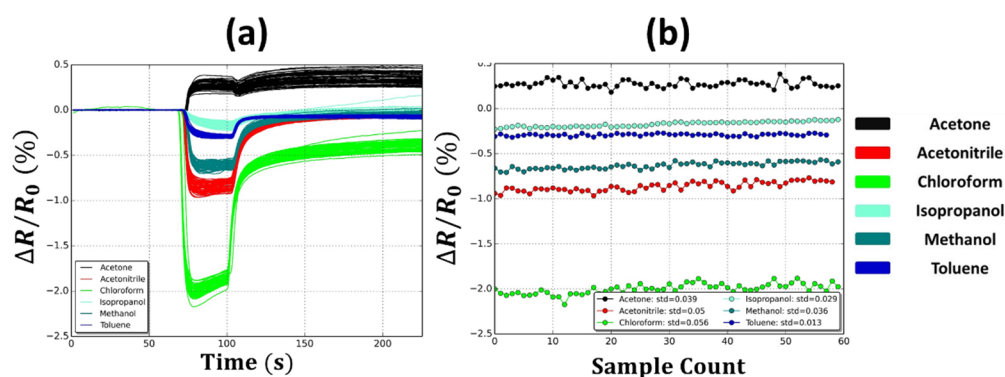


**Figure 3.6** Time-series plot of the change in resistance and b) sample-to-sample variation of the response for a graphene sensor exposed to acetone, acetonitrile, chloroform, isopropanol, methanol, and toluene for 60 exposures each.

**Table 3.1** Average change in resistance and corresponding standard deviation values of a graphene sensor when exposed to acetone, acetonitrile, chloroform, isopropanol, methanol, and toluene for 60 exposures each.

Compound	Average $\Delta R/R_0$ (%)	Standard Deviation
Acetone	0.27	$\pm 0.0391$
Acetonitrile	-0.86	$\pm 0.0508$
Chloroform	-1.98	$\pm 0.0530$
Isopropanol	-0.14	$\pm 0.0267$
Methanol	-0.62	$\pm 0.0370$
Toluene	-0.27	$\pm 0.0170$

### 3.3 Response Magnitude and Signal-to-Noise

Although graphene is strictly defined as a single atomic layer of carbon, it often comes in bi-layer and few-layer varieties. These varieties could either be intentional or unintentional due to the manufacturing process. Characteristics of the sensor response such as magnitude and noise could potentially be affected by the number of graphene layers.

Figure 3.7 provides a comparison of measured sensor response for a device using single layer graphene and few-layer graphene. The devices were fabricated in the same manner with identical IDE pattern and measurements were performed under the same experimental conditions and for the same chemical set. The single layer graphene sensor response is larger than that of the few-layer graphene sensor for every compound by at least 2x and up to 7x. For each compound it can also be observed that the shape of the response remains approximately the same even though the magnitudes differ.

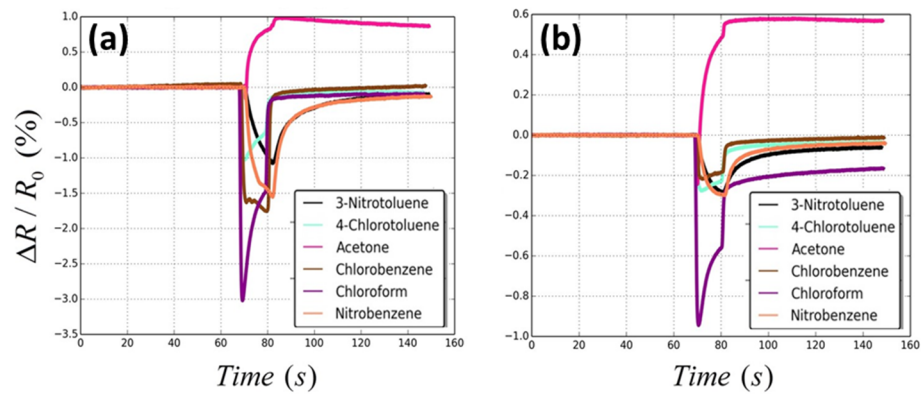


**Figure 3.7** Sensor response for device using a) single-layer graphene and b) few-layer graphene.

Although the magnitude of response is larger for the single-layer device, this comparison metric does not take into account the noise contained in the baseline measurements before the chemical compound is introduced to the sensor. This is important to consider especially when trying to determine limits of detection, and is commonly used to determine if a signal can be resolved from the measurement noise. Figure 3.8a summarizes the change in resistance values for single layer and few-layer graphene sensors. As

previously discussed, it can easily be seen that the response values obtained using a single layer device are much larger than those obtained from a few-layer device. Figure 3.8b summarizes the calculated signal-to-noise ratio (SNR) values for each sensor type and chemical compounds. This comparison contradicts what is seen when strictly looking at the magnitude of the response, where the SNR for the few-layer graphene sensor is either very comparable to or larger than the SNR for the single layer sensor. This could be attributed to low-frequency,  $1/f$  noise caused by impurity charges in the substrate. This noise is believed to be less prevalent in graphene devices with more graphene layers due to the ability of the additional layers to screen the top conducting layer from substrate effects. Since the top graphene layer is contact with the surrounding environment, it is conceivable that less noise would be contained in the steady-state baseline measurement region of the chemical sensor response, leading to higher SNR values.

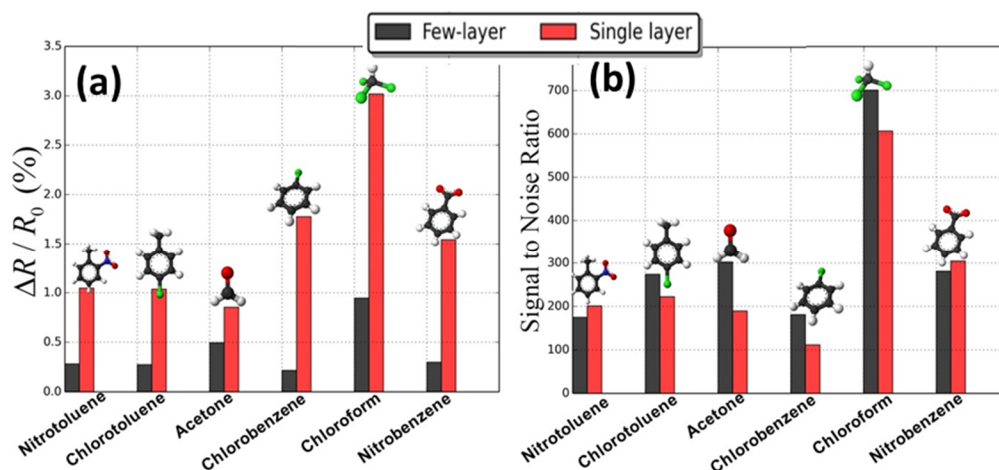


**Figure 3.8** a) Change in resistance and b) signal-to-noise ratio for single layer graphene and few layer graphene .

### 3.4 Concentration Effects

Most chemical sensors possess a linear dependence with the concentration of the present compound. This is a useful relationship for determining the limit of detection, but causes issues for sensor systems which rely on the maximum change in resistance as a discriminating feature for chemical classification. To demonstrate this effect, a graphene sensor was exposed to acetonitrile, chloroform, and toluene in a series of decreasing concentrations. Shown in Figure 3.9a is a time series-plot containing responses to 10 different concentrations for each compound, ranging from 1% - 10% saturated vapor in 1% increments. To illustrate the effect of choosing a feature, such as maximum change in resistance, which is dependent on concentration, a PCA plot was created which uses the maximum change in resistance as the feature. Figure 3.9b shows a PCA plot for the concentration dependent response data, using the maximum change in resistance as the feature. For all compounds it can be observed that as the concentration of each compound decreases, each point travels closer to the 1% point, where they eventually converge. At this low concentration it would be more difficult to distinguish the compounds from each other, unless additional descriptive features were contained in the response curve and could be used to aid in their discrimination.

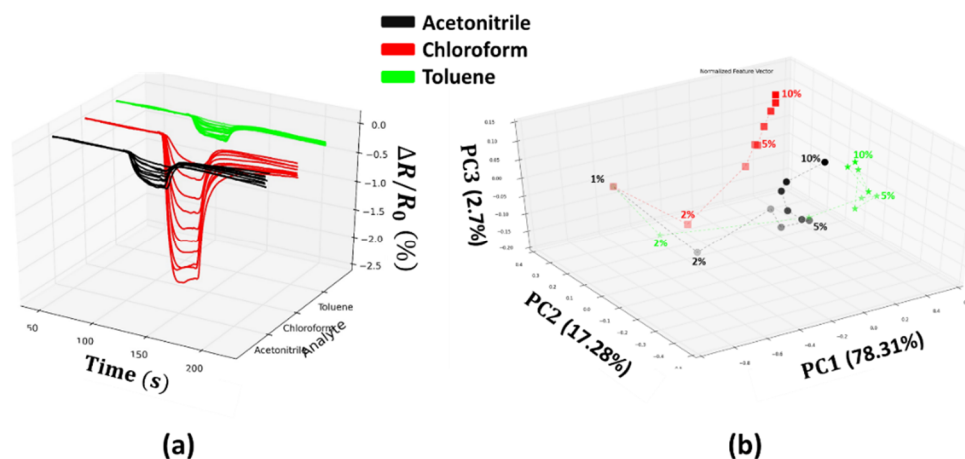


**Figure 3.9** Concentration dependent response characteristics for acetonitrile, chloroform, and toluene showing a) variation in the change in resistance and b) PCA plot with wandering points which eventually converge at low concentrations.

### 3.5 Residual Transfer Polymer Effects

The current process using graphene prepared by CVD growth on metal substrates requires the use of a transfer polymer. After the metal substrate is removed by chemical etching, the graphene remains attached to the transfer polymer, which can then be applied to a final substrate. Once the graphene is transferred to the final substrate the transfer polymer can be removed with either solvents or reactive plasma treatments. The most widely used and accepted transfer polymer is PMMA.

ACS materials offers a Trivial Transfer Graphene product that is advertised to allow transfer of graphene film to any substrate in seconds. The graphene layer(s) come as a 1 cm x 1 cm square on a polymer sponge. The graphene film, which is covered in a PMMA layer, is released from the sponge by applying water around its perimeter. Once the film begins to lift it is placed in a water bath where it floats until scooped up with a substrate. Since

PMMA is a fairly common polymer, it is often used in chemical sensing as a composite material,<sup>55,56</sup> it is worth investigating the response of a graphene sensor with the PMMA coating still intact. Shown in Figure 3.10 are the response curves of a graphene sensor with the PMMA layer and then with the PMMA removed by soaking in acetone. For each compound exposure, a time delay of the sensor response can clearly be seen. The time difference,  $\Delta t$ , was found for each compound by finding the point at which the sensor just begins to respond and calculating the difference in time between the sensor with PMMA and without PMMA. The calculated time difference for chloroform, diethyl ether, acetone, acetonitrile, and formaldehyde were found to be 11.04 s, 10.90 s, 4.95 s, 4.61 s, and 2.51 s, respectively. Table 3.2 summarizes the calculated time difference for each compound and also lists each molar mass. It is not surprising that the molar mass is positively correlated with time difference between responses since the compound needs to make its way through the polymer before it interacts with the sensitive graphene film.

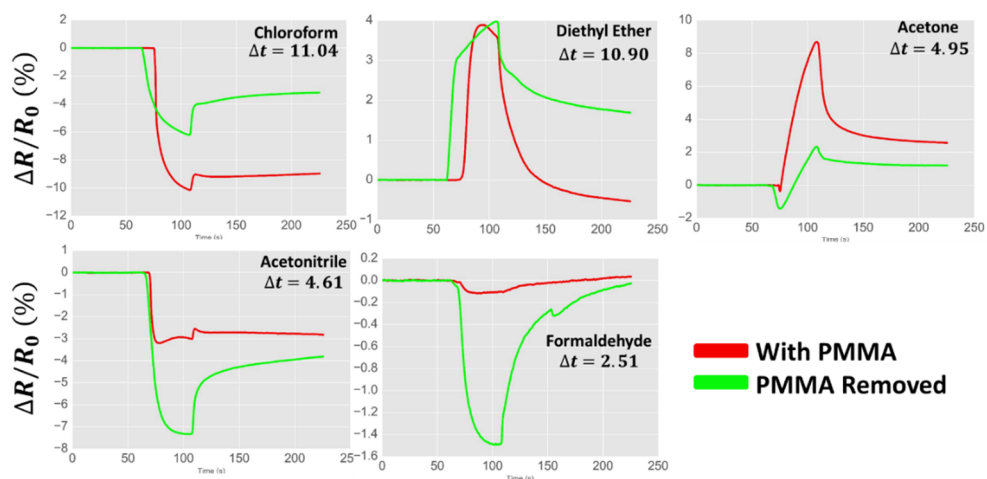


**Figure 3.10** Comparison of sensor response with and without PMMA transfer polymer for chloroform, diethyl ether, acetone, acetonitrile, and formaldehyde.

**Table 3.2** Relationship between the molar mass and the calculated time difference between the sensor response with and without PMMA.

Compound	Molar Mass (g/mol)	$\Delta t$ (s)
Chloroform	119.38	11.04
Diethyl Ether	74.12	10.90
Acetone	58.08	4.95
Acetonitrile	41.05	4.61
Formaldehyde	30.03	2.51

### 3.6 Response Mechanism

The interaction of chemical compounds with graphene and the mechanisms which cause electrical changes is not well understood. Typically, this process is generalized by eluding to a charge transfer process, but lacks the details to support this basis. In one of the first reported applications of using graphene as a chemical sensing material, Schedin et al.

reported single molecule detection and attributed the change in conductivity of the device to compounds acting as either electron acceptors or electron donors, causing a charge transfer.<sup>28</sup> For example, different gases caused different effects on the resistivity, with electron acceptors (e.g., NO<sub>2</sub>, H<sub>2</sub>O, and I<sub>2</sub>) and electron donors (e.g., CO, ethanol, and NH<sub>3</sub>) causing a decrease and increase in resistivity, respectively. The change in carrier concentration is the basic mechanism describing the operation of all electrical conductivity-based graphene gas sensors, where the conductivity is proportional to the product of number of charge carriers and mobility.

Modification of the graphene surface can largely be categorized into covalent and non-covalent modifications. Covalent modification typically involves physical disruption of the in-plane, sp<sup>2</sup> carbon-carbon bonds, which are converted into covalent sp<sup>3</sup> bonds with the modifying compound. This is usually considered a permanent modification and alters the properties of the graphene, such as its electrical conductivity and surface reactivity. Non-covalent modification is a more temporary modification process and involves weaker bonds, which may be disrupted or removed with elevated temperatures, UV light treatments, or application of chemical compounds. With respect to graphene used as a chemical sensing material, the interaction of a chemical compound with the graphene surface is most likely a weak, non-covalent interaction based on physisorption. Much of this can be inferred from inspection of the sensor response to various chemicals. If no additional techniques are needed to drive off the sampled compounds, such as elevated temperatures or UV light treatments, and the sensor signal recovers to its baseline value, it is reasonable to assume that a non-covalent interaction has occurred. On the other hand, if the sensor response does not recover well, it is possible that some degree of covalent attachment has occurred. This

modification will build over time, causing a modification to the baseline, and over an extended period of time it may cause the sensor to become non-responsive or change its characteristics entirely.

Due to the 2D,  $sp^2$  hybridized structure of graphene, a single electron remains perpendicular to the surface and is responsible for graphene's conductivity. Graphene is ultimately mated to a substrate in order to create useful devices and is typically not suspended due to the difficulties of obtaining and the fragile state of a suspended 2D material. The underlying substrate on which graphene is placed has a profound effect on its electrical properties, and some of the electrical defects that may be present in the substrate can be mirrored on the graphene surface. Strano et al. introduced the idea of electron-hole puddles, which are induced by the underlying graphene substrate.<sup>46</sup> By placing graphene over substrates with various levels of surface energy ranging from hydrophilic (plasma cleaned  $SiO_2$ ) to hydrophobic (Octadecyltrichlorosilane) and performing Raman spectroscopy measurements, they were able to show that graphene placed over substrates with a polar, hydrophilic surface caused a more reactive graphene surface. The increase in graphene surface reactivity is attributed electron-hole puddling which is mirrored to the graphene surface from charged impurities in the  $SiO_2$  substrate. This theory has potential to describe interactions at the surface of graphene-based chemical sensors.

Consider Figure 3.11, where a non-polar, aromatic compound and a polar compound approach the surface of a continuous single layer of graphene. Figure 3.11a illustrates the case when the conductivity of graphene is increased, which may be attributed to additional electron contribution from  $\pi$ - $\pi$  stacking. Aromatic compounds, such as toluene, tend to stack themselves parallel to the surface of other materials with a  $\pi$ -electron system. The

additional  $\pi$ -electron cloud from the toluene may contribute additional electrons, causing a temporary increase in conductivity. Besides toluene, eleven other aromatic compounds with various functional groups also caused the graphene's resistance to decrease. The direction of response produced by these compounds appears to be independent of the nature of the functional group. Although the direction of the response is the same for all of these compounds, many of the response curves have additional features that may be a consequence of the functional group, such as response magnitude, response time, and recovery time. The functional group may cause the aromatic compounds to stack at different distances from the graphene surface, which could explain the presence of these additional features. Figure 3.11b presents the opposite case, where the conductivity of the graphene is decreased. Here, acetone, a polar compound, causes electrons to be pushed away from the surface to the opposing face of the graphene which is in contact with the substrate. In addition to acetone causing an increase in graphene resistance, other related polar compounds such as cyclohexanone, diethyl ether, dimethyl sulfoxide, and tetrahydrofuran also cause an increase in resistance. Each of these compounds are related by an electron rich oxygen that is bonded in different configurations. The commonly used charge transfer theory makes sense in certain cases but has not been extensively applied. The described theory herein attributes the chemically induced change of the graphene conductivity to a temporary electrostatic disruption of the  $\pi$ -electron system.

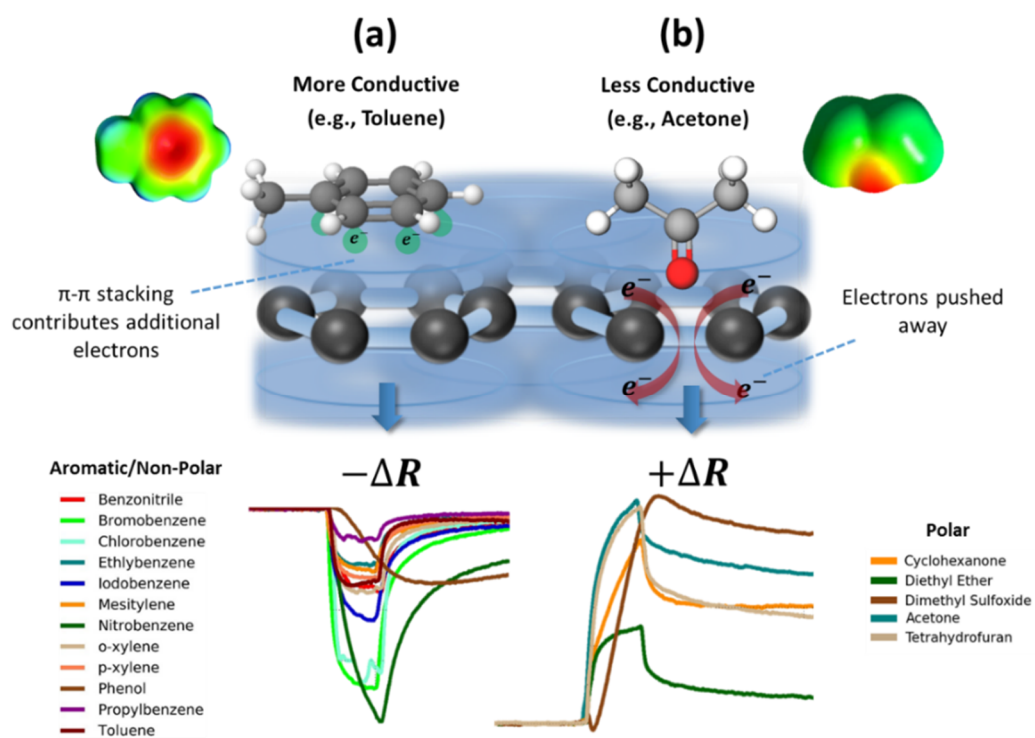


**Figure 3.11** Proposed graphene sensor response mechanism for when the graphene becomes a) more conductive and b) less conductive.

## Chapter 4 Chemical Discrimination with an Unmodified Graphene Chemical Sensor

### 4.1 Abstract

A graphene chemical vapor sensor with an unmodified surface has been fabricated and thoroughly characterized upon exposure to headspace vapor of a variety of solvents and related compounds. The vapor sensor exhibits excellent discrimination towards a variety of chemical compounds. Principle component analysis (PCA) was performed to explore the extent of grouping for each compound and separation between compounds and chemical classes. The prediction accuracy of the sensor is evaluated with linear discrimination analysis, k-nearest neighbor, random forest, and support vector classifiers. The combination of PCA and prediction accuracies demonstrate the discrimination capability of an unmodified graphene chemical vapor sensor. Such a vapor sensor is very attractive for application in small, low-power, robust, and adaptable cross-reactive arrays in electronic noses.

\* This chapter is reproduced according to American Chemical Society copyright guidelines, from "Chemical Discrimination with an Unmodified Graphene Chemical Sensor" by Eric C. Nallon, Vincent P. Schnee, Collin J. Bright, Michael P. Polcha, and Qiliang Li, ACS Sensors, 2015. Copyright 2015, American Chemical Society.

## 4.2 Introduction

Materials based on carbon allotropes have been heavily explored in recent years and have found their way into chemical vapor sensors. Some of the most successful materials used in this type of sensing application include carbon black,<sup>57–60</sup> carbon nanofibers,<sup>61–63</sup> carbon nanotubes,<sup>17,64–68</sup> and graphene,<sup>28,30,38,69–72</sup>. Although much impressive research has been accomplished in this area, a great need still exists for simple, low-cost, low-power, reliable, and easy-to-manufacture chemical sensors. Such versatile sensors can be utilized across different areas, such as environmental monitoring,<sup>73,74</sup> medical diagnostics,<sup>75</sup> drug screening,<sup>76,77</sup> process monitoring,<sup>78</sup> food and beverage quality assurance,<sup>26,79,80</sup> automotive and aerospace applications,<sup>4</sup> and detection of chemical warfare<sup>81</sup> and explosive<sup>82,24</sup> compounds for military and homeland security applications.

Graphene is of particular interest for chemical sensing applications mainly due to its 2D structure and carbon composition. Every carbon atom in graphene is a surface atom, providing the greatest possible surface area per unit volume so that electron transport is highly sensitive to adsorbed molecular species.<sup>38</sup> The carbon makeup of graphene also provides many avenues to perform surface modifications, including the attachment of organic groups, metal nanoparticles, enzymes, biomolecules, polymers, and many more.<sup>83</sup> The ability to modify sensor elements to be broadly responsive is desirable when considering their use in cross-reactive arrays towards such applications as an electronic nose.

Obtaining broad selectivity with a single chemical sensor is difficult. It is generally achieved with metal-oxide based sensors, which rely on temperature modulation to gain selectivity. However, this strategy increases system complexity. Dobrokhotov<sup>84</sup> reports

vapor recognition with a single zinc oxide chemiresistor for acetone, ethanol, and toluene, which is primarily accomplished through processing the chemiresistor response data with a fast Fourier transform combined with quadratic discriminant analysis. Rumyantsev et al. reported selective gas sensing with a single pristine graphene transistor,<sup>34</sup> which used the vapor-induced change in low frequency noise spectra as an additional sensing parameter to enhance selectivity. This is a novel method for gaining additional discrimination information from the same device, although this type of measurement can be difficult to perform and may be impractical for handheld and small footprint applications.

In this work, we report that, graphene chemical vapor sensors with an unmodified surface possess an intrinsic, broad selective nature capable of discriminating between both chemically diverse and chemically similar compounds. The sensors also exhibit other desirable characteristics such as room temperature operation, rapid response and recovery, reversibility, reproducibility, stable operation, low cost, and low power consumption. A chemically diverse set of compounds consisting of ketones, ethers, hydrocarbons, organosulfurs, and acids was used to study the broad, but diverse sensing response that is achievable. An additional set of mono-substituted benzene compounds was used to investigate how the sensor responds to chemically similar compounds.

### **4.3 Experimental Methods**

The graphene sensors fabricated for all experiments consisted of monolayer CVD graphene on an insulating Si/SiO<sub>2</sub> substrate with Ti/Au interdigitated electrode contacts, creating a chemiresistor device. Monolayer graphene on 1 cm x 1 cm Si/SiO<sub>2</sub> substrates were purchased from Graphenea (Cambridge, MA) and used as received. Devices were

created by performing standard photolithography to define interdigitated electrode contacts. A Temescal BJD-1800 electron beam evaporator was used to deposit Ti/Au (25 nm/300 nm), followed by successive soaking in acetone, isopropanol and deionized water to achieve metal lift-off. The interdigitated electrode pattern consisted of 16 fingers with a length of 1000  $\mu\text{m}$ , width of 50  $\mu\text{m}$ , and separation of 50  $\mu\text{m}$ , producing a total sensor area of 0.8  $\text{mm}^2$ . After nitrogen drying, the patterned device was mounted in a 68-pin leadless chip carrier and wire bonded. The bonded device was loaded into a 68-pin breakout board outfitted with a custom machined Teflon block to provide a low volume flow channel of 0.25 mL to the sensor surface. The entire sampling process was automated using a custom headspace sampling system, where the sensor was brought to the opening of a 40 mL vial containing the analytes shortly after it was unsealed. The sampling system and sensor were contained in a custom enclosure outfitted with a fume extraction system which was located in an ambient laboratory area. Each measurement was conducted under the same experimental conditions. A Keithley 2450 (Cleveland, OH) source meter was used for resistance measurements, collecting data at approximately 14 Hz.

A Python script was used to read a user generated input CSV file specifying the measurement parameters for a single measurement; which are baseline time, sample time, recovery time, device voltage, and sample flow rate. In this manner, many repetitions can be performed in a standardized and reproducible manner, generating large volumes of highly reproducible data. Features were extracted from each change in resistance response curve by calculating the maximum resistance change and the area of the response and recovery portion of the curve. For statistical purposes, 20 repetitions of each compound were collected and principal component analysis (PCA) was performed to visually explore the

discrimination ability of the sensor. The resulting grouping from PCA showed excellent separability, especially when considering results are based on a single sensor opposed to a sensor array. The ability of the sensor to correctly classify unseen measured response data was evaluated by a combination of cross-validation and linear discrimination analysis (LDA), k-nearest neighbor (kNN), random forest (RF), and support vector machine (SVM) classifiers. All post processing, data analysis and plotting was performed using Python 2.7 with scipy, numpy<sup>8</sup>, pandas<sup>9</sup>, scikit-learn<sup>10,85,86</sup> and matplotlib<sup>12</sup> modules.

#### 4.4 Sensor Response Data Processing

Resistance values were computed by using the applied bias voltage and measured current from the Keithley 2450 source meter. The start and stop times for each measurement were stored during each measurement, and were subsequently used to automatically calculate the maximum change in resistance ( $\Delta R$ ), area of the response signal ( $A_{\text{Resp}}$ ), area of the recovery signal ( $A_{\text{Recov}}$ ), and a ratio of the response to recovery area ( $A_{\text{Resp/Recov}}$ ). Preprocessing procedures included correction of drift by means of a first order linear fit and calculation of fractional change in resistance.<sup>4</sup> The illustration in Figure 4.1 shows three typical regions of response to a chemical analyte, where the response is represented by a change in resistance over time. Region I is the baseline period during which room air flows over the sensor without any analyte present. Region II represents the sampling period during which the sensor head is lowered into the headspace of an open vial and the headspace vapor flows over the sensor at the same flowrate as in the baseline period. The recovery phase shown in region III begins when the sensor head is removed from the vial headspace and room air again flows over the sensor. Various features can be extracted

from the response curve, and are used as discriminators in further data exploration and classification. The maximum change in resistance is calculated by taking the difference between the maximum signal change in signal value and the average value of the baseline resistance points contained within region I. The area contained in region II and region III is calculated by using the trapezoidal rule to approximate the area under the curve, with  $A_{\text{Resp}}$  calculated between  $t_a$  and  $t_b$  and  $A_{\text{Recov}}$  calculated between  $t_b$  and  $t_c$ , as marked in Figure 4.1.

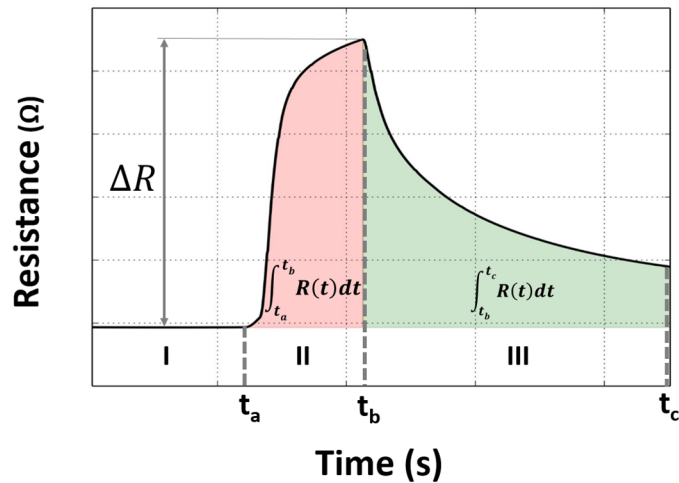


**Figure 4.1** Typical sensor response curve with regions I) baseline, II) sample, and III) recovery. Potential features that can be extracted include the maximum change in resistance ( $\Delta R$ ), area of the response (red shaded area), and area of the recovery (green shaded area).

## 4.5 Results and Discussion

### Sensor Response: Chemically Diverse Compounds

The sensor response was investigated by measuring the fractional change in resistance upon exposure to a set of 11 chemically diverse analytes: 2-nitrotoluene (2NT), 4-chlorotoluene, acetic acid, acetone, chloroform, cyclohexanone, diethyl ether, dimethyl sulfoxide (DMSO), hexane, tetrahydrofuran (THF), and toluene. The sensor was biased at a constant voltage of 10 mV and the current recorded continuously for each individual measurement from which the resistance change was calculated. The baseline, sample, and recovery times were set to 60 s, 30 s, and 120 s, respectively, with a flow rate of 10 mL/min. Each compound was repeated twenty times in a randomized order under the same experimental conditions. Response curves representing the change in resistance upon exposure to each analyte are shown in Figure 4.2a. For the purpose of highlighting the shape and direction of each response, the resistance values have been normalized using vector normalization, where the y-axis is now represented by arbitrary values. Initial sensor response upon exposure to an analyte occurs within approximately 1 s, regardless of analyte. The magnitude, direction, and shape of the response, however, do vary as a function of analyte. An increase in resistance was observed for ethers (e.g., diethyl ether, THF), ketones (e.g., acetone, cyclohexanone), and DMSO, an organosulfur compound. Similarly, a decrease in resistance was observed for chlorinated hydrocarbons (e.g., chloroform, 4-chlorotoluene), hydrocarbons (e.g., toluene, hexane), 2NT, and acetic acid. Looking beyond the magnitude and direction of the response and towards the shape of the curve reveals the diversity between each analyte response. PCA was performed to further explore the

relationship between the tested analytes, including grouping of each compound and separations between compounds.

The  $\Delta R$ ,  $A_{\text{Resp}}$ ,  $A_{\text{Recov}}$ , and  $A_{\text{Resp/Recov}}$  features were calculated for each measurement (11 compounds, 20 repetitions) to create a 4 x 220 feature vector as the input to PCA. Each row represents a single measurement and each column represents a feature calculated for that particular measurement. Vector normalization was then performed on the feature vector in order to bring the values of each feature on the same scale. The PCA transformation for all response curves from Figure 4.2a is represented in Figure 4.2b, with the same coloring scheme and corresponding chemical structure. Excellent grouping can be seen for the repetitions of each analyte, and good separability exists between analyte classes. Some general observations can be made: ethers and ketones group closely together, with DMSO slightly outside of that group; the relatively non-polar compounds toluene, hexane, chloroform, and 4-chlorotoluene form a group; while 2NT is not near any other analyte.

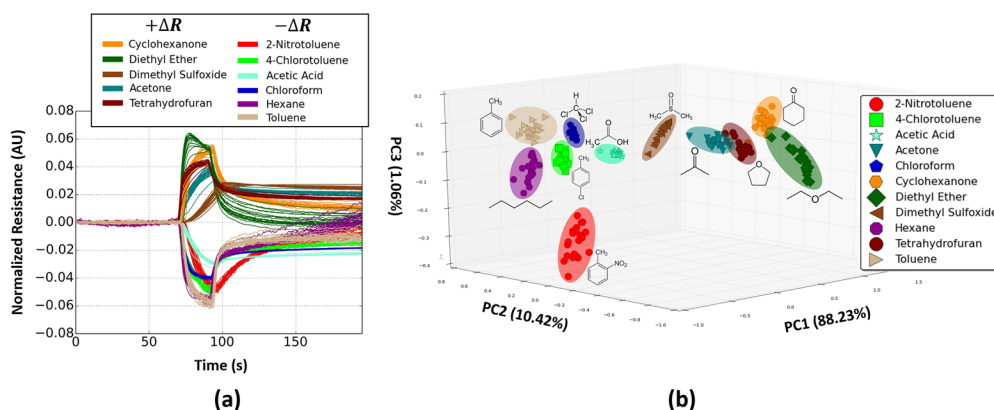


**Figure 4.2** a) Normalized sensor response to a chemically diverse set of compounds and b) corresponding PCA transform.

The values in Table 4.1 summarize the average  $\Delta R$  and signal-to-noise ratio (SNR) values for each analyte, along with their respective standard deviations. The percentage change in resistance was largest for chloroform with a value of -4.73%, and smallest for 2NT with a value of -0.22%. Although some of the changes in resistance values are small, the SNR values are large in every case, even when considering the worst case of subtracting the maximum standard deviation.

**Table 4.1** Maximum change in resistance, SNR values, and corresponding standard deviations for the responses shown in Figure 4.2. The mean and standard deviation were calculated for twenty measurements of each analyte.

Compound	$\Delta R$ (%)	SNR
Tetrahydrofuran	$2.52 \pm 0.26$	$497 \pm 70$
Dimethyl Sulfoxide	$1.47 \pm 0.20$	$333 \pm 46$
Acetone	$1.00 \pm 0.21$	$219 \pm 49$
Diethyl Ether	$0.83 \pm 0.08$	$167 \pm 24$
Cyclohexanone	$0.76 \pm 0.11$	$171 \pm 22$
Chloroform	$-4.47 \pm 0.29$	$1080 \pm 89$
Acetic Acid	$-3.34 \pm 0.79$	$748 \pm 174$
4-Chlorotoluene	$-0.53 \pm 0.07$	$118 \pm 17$
Toluene	$-0.31 \pm 0.03$	$73 \pm 8$
Hexane	$-0.25 \pm 0.02$	$52 \pm 7$
2-Nitrotoluene	$-0.22 \pm 0.04$	$28 \pm 10$

### Sensor Response: Chemically Similar Compounds

Under the same experimental conditions described previously, the graphene sensor was exposed to a group of mono-substituted benzene compounds consisting of: benzonitrile, bromobenzene, chlorobenzene, ethylbenzene, iodobenzene, nitrobenzene, phenol, propylbenzene, and toluene. The fractional change in resistance for each

compound is shown in Figure 4.3a, along with the PCA transformation for all response curves in Figure 4.3b. The same coloring scheme and corresponding chemical structure are shown for direct comparison.

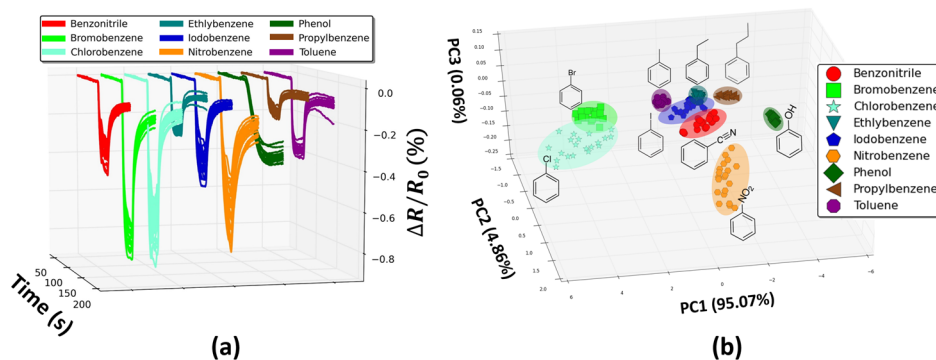


**Figure 4.3** a) Sensor response to a group of substituted benzene compounds and b) corresponding PCA transform.

The values in Table 4.2 summarize the average  $\Delta R$  and SNR values for each analyte, along with their standard deviations for each set of repetitions. The percentage change in resistance was largest for the halogenated substituted compounds, with bromobenzene at a value of -0.78% and chlorobenzene very close at -0.76%. Upon inspection of the PCA transformation shown in Figure 4.3b, some trends can be seen between compounds with similar properties. Two of the three halogenated compounds, bromobenzene and chlorobenzene, clearly form a group by themselves and both have similar vapor pressure and dipole moment values. On the other hand, the third halogenated compound, iodobenzene does not cluster with the other two likely do the addition of the heavier iodine substituent, giving the compound an order of magnitude lower vapor pressure, decreasing the

concentration reaching the sensor. The aliphatic substituted benzenes; Toluene, ethylbenzene, and propylbenzene also cluster amongst themselves. The iterative addition of one carbon to the substituted chain leads to an increasing dipole moment and decreasing vapor pressure. These changes are presumably represent in the PCA plot, where these three compounds order along the major principle component in accordance with the described trends. Both phenol and nitrobenzene are grouped by themselves, which may be attributed to longer recovery portion of the signal seen in Figure 4.3a. The longer recovery of phenol and nitrobenzene may be the result of their relatively low vapor pressures of 0.4 mmHg and 0.15 mmHg, respectively, causing slow desorption from the graphene surface. Although some similarities can be seen, a general relationship between response characteristics and physical properties does not appear to apply to all compounds.

**Table 4.2** Maximum change in resistance, SNR values, and corresponding standard deviations for the responses shown in Figure 4.3. The mean and standard deviation were calculated for twenty measurements of each analyte.

Compound	$\Delta R$ (%)	SNR
Bromobenzene	$-0.78 \pm 0.05$	$209 \pm 16$
Chlorobenzene	$-0.76 \pm 0.08$	$207 \pm 23$
Nitrobenzene	$-0.65 \pm 0.11$	$168 \pm 28$
Iodobenzene	$-0.42 \pm 0.05$	$114 \pm 16$
Toluene	$-0.36 \pm 0.02$	$97 \pm 7$
Benzonitrile	$-0.35 \pm 0.26$	$94 \pm 14$
Ethylbenzene	$-0.25 \pm 0.01$	$67 \pm 4$
Phenol	$-0.22 \pm 0.02$	$59 \pm 8$
Propylbenzene	$-0.17 \pm 0.02$	$46 \pm 5$

## 4.6 Classification Accuracy

The previously described PCA plots display excellent separation, but only provide a visual representation of the extracted sensor features. The goal of a predictive sensor system is to create a generalized model during a training phase with known data, then when unseen data is encountered, the model attempts to predict its class. In this fashion, the previously described data sets were used to train various machine learning classification algorithms and then tested on unseen data to determine classification accuracy. The same feature vectors used as inputs to the PCA transformations in Figure 4.2b and Figure 4.3b were used as inputs to kNN, linear SVM, RF, and LDA classification algorithms.<sup>10</sup> The chemically diverse set (Set A) consists of 220 total measurements, while the substituted benzene set (Set B) consists of 180 total measurements, with each set containing 20 repetitions of each compound. To avoid overfitting, k-fold cross-validation was implemented with a training size of 60%, testing size of 40%, and k-fold value of 10. The training and testing percentages correspond to a train/test count of 132/88 and 108/72 for Set A and Set B, respectively. Each classification algorithm was trained on the training data and used to predict the class of the unseen testing portion. The resulting classification accuracy for each classifier and data set are shown in Figure 4.4. For Set A, the overall classification accuracy was above 90% for every classifier with an accuracy of 95%, 95%, 96%, and 92% for kNN, SVM, RF, and LDA, respectively. Similarly, for Set B, the classification accuracies were 89%, 92%, 88%, and 92% for kNN, SVM, RF, and LDA, respectively.

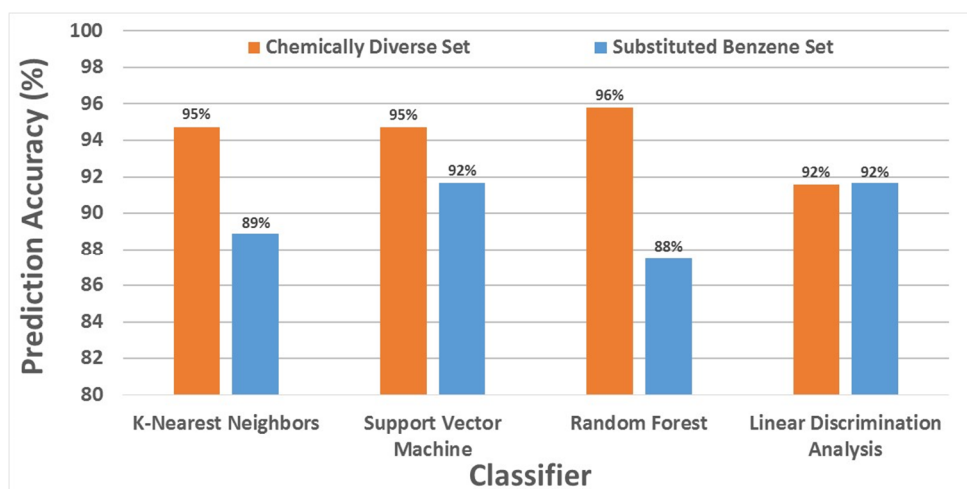


**Figure 4.4** Classification accuracy comparison for the chemically diverse and substituted benzene data sets using K-Nearest Neighbors, Linear SVM, Random Forest, and Linear Discrimination Analysis classifiers.

The classification accuracies shown in Figure 4.4 are averages for classification of all compounds in each set. A confusion matrix is used to itemize the the classification accuracy for each individual compound and can provide insight into what compounds are commonly being confused with each other. For the eight possible classification values shown in Figure 4.4, two were chosen which best represent the overall trend of misclassified compounds. Figure 4.5a represents the confusion matrix for Set A, using the kNN classifier, which produced an accuracy of 95%. The most frequent misclassifications in this set were diethyl ether as cyclohexanone, hexane as toluene, and toluene as hexane. These misclassifications are not surprising considering the relative PCA grouping of diethyl ether and cyclohexanone and the higher amount of noise found in the hexane and toluene response curves, which is higher than all other. For Set B, the most encountered missclassifications were iodobenzene as benzonitrile, chlorobenzene as bromobenzene, ethylbenzene as propylbenzene, and



modifications to enhance selectivity; and therefore, the observed responses were inherent to the material and device itself. Other notable characteristics of the sensor include room temperature operation, rapid response and recovery, reversibility, reproducibility, and stable operation. The capability of the sensor to discriminate between various compounds was first evaluated by PCA, which displayed excellent separation between compounds. Further studies using machine learning based classification algorithms were used to evaluate the capability of the sensor to correctly classify chemically diverse and chemically similar compounds. In this work, the sensor was capable of classifying 11 chemically diverse compounds and 9 mono-substituted benzene compounds with an accuracy of 96% and 92%, respectively. These results are compelling for a single sensor and indicate a promising future for graphene based sensor arrays. Such a level of selectivity and discrimination for a single sensor has not yet been reported. In addition, such a high-performance device is an excellent candidate to serve as a platform for surface modified elements in a cross-reactive array to further increase discrimination and classification towards a versatile, adaptable system capable of being used across multiple fields.

## Chapter 5 Discrimination Enhancement with Transient Feature Analysis of a Graphene Chemical Sensor

### 5.1 Abstract

A graphene chemical sensor is subjected to a set of structurally and chemically similar hydrocarbon compounds consisting of toluene, o-xylene, p-xylene, and mesitylene. The fractional change in resistance of the sensor upon exposure to these compounds exhibits a similar response magnitude among compounds, while large variation is observed within repetitions for each compound, causing a response overlap. Therefore, traditional features depending on maximum response change will cause confusion during further discrimination and classification analysis. More robust features which are less sensitive to concentration, sampling, and drift variability would provide higher quality information. In this work, we have explored the advantage of using transient based exponential fitting coefficients to enhance the discrimination of similar compounds. The advantages of such feature analysis to discriminate each compound is evaluated by using principle component analysis (PCA). In addition, machine learning based classification algorithms were used to compare the prediction accuracies when using fitting coefficients as features. The additional features greatly enhanced the discrimination between compounds while performing PCA, and also improved the prediction accuracy by 34% when using linear discrimination analysis.

\* This chapter is reproduced according to American Chemical Society copyright guidelines, from "Discrimination Enhancement with Transient Feature Analysis of a Graphene Chemical Sensor" by Eric C. Nallon, Vincent P. Schnee, Collin J. Bright, Michael P. Polcha, and Qiliang Li, *Analytical Chemistry*, 2015. Copyright 2015, American Chemical Society.

## 5.2 Introduction

The changes in electrical, photophysical, and mechanical properties of a device can be used as the transduction mechanism of a chemical sensor. Generally, the magnitude of the signal change is used as a key discriminating feature. This value varies strongly with analyte concentration and chemical properties of the compound, causing the interpretation of similar compounds to become convoluted.<sup>87</sup> In realistic environments the concentration is unknown and can vary due to external factors such as temperature and humidity. Even in a controlled laboratory environment analyte vapor concentrations can vary, ultimately producing variations in the sensor response. The maximum steady-state change is the most popular feature used in chemo-sensory data processing and has been used in many types of chemical sensors including, but not limited to graphene,<sup>29,88</sup> carbon nanotubs,<sup>17,89–91</sup> carbon black,<sup>92</sup> non-fluorescent organic polymers,<sup>93,94</sup> fluorescent organic polymers,<sup>24</sup> metal oxide semiconductor,<sup>95</sup> metal organic frameworks,<sup>96</sup> surface acoustic wave,<sup>97</sup> and recent 2D material systems.<sup>98,99</sup> Two practical issues exist in capturing this value: first, it becomes available late in the response, and second, it is susceptible to drift.<sup>100</sup> Depending on the sensing material and sensor type, the response time can range from fractions of a second to minutes, which in the latter case causes the steady-state response to be available late after sampling begins. Response drift can be attributed to both sensor related issues such as aging and fouling, and measurement related issues such as temperature, flow, and humidity fluctuations. Similar chemicals also tend to produce similar steady-state responses, especially for single devices opposed to sensor arrays, further convoluting the interpretation of the sensor output.

Many chemical sensors tend to exhibit time-dependent exponential behavior during their response and recovery phase. The interaction of a chemical species with a chemical sensor can either be confined to the surface of the sensing layer, or it can take place in the volume of the sensitive coating. Surface interaction implies that the species of interest is adsorbed at the surface or interfaces and can be described by solid-gas molecular kinetics. Adsorption rate relationships and isotherms such as Langmuir, Freundlich, or Brunauer-Emmett-Teller may be used to model the adsorption and desorption process at the solid-gas interface of graphene and other chemical sensors.<sup>101</sup> An empirically fitted relationship between the transient sensor response and a physical adsorption/desorption model can indirectly provide information about the adsorbed analytes' physical and/or chemical properties. This type of information is less susceptible to drift and concentration fluctuations, and would provide excellent discriminative information.

Ideally, chemical sensor time-series response data would be processed in a manner which provides chemical and physical properties of the analyte. For example, the dipole moment of an analyte has been related to the response of various chemical sensors including the change in resistance of an epitaxial graphene sensor<sup>69</sup> and tungsten oxide nanosensor,<sup>102</sup> and change in drain current of an organic field effect transistor.<sup>103</sup>

In this work, a resistive graphene chemical sensor is exposed to the chemically and structurally similar compounds: mesitylene, o-xylene, p-xylene, and toluene. We demonstrate the advantages of using exponential fitting coefficients as features to enhance discrimination and classification. For these compounds, we have also investigated relationships between the extracted fitting coefficients and the analytes' vapor pressure and

molar mass. The fractional change in resistance of the graphene sensor exhibits similar magnitudes between compounds and significant variation of this magnitude for repeated exposures of each compound. Traditional identifying features based on the maximum response change adopt these variations, which eventually results in misclassification. The advantage of using exponential fitting coefficients is explored by fitting all features, including those based on the steady-state response, to a random forest classifier and evaluating the feature importance contribution through a weighted contribution method. Principal component analysis (PCA) was then used to visually demonstrate the effect of the additional features on the spatial separation and grouping of each compound. Additionally, the k-nearest neighbor (kNN), random forest, and linear discrimination analysis (LDA) learning algorithms were fit to each set of features to determine if the additional features lead to increased classification accuracy.

### **5.3 Materials and Methods**

In this work, monolayer graphene on 1 cm x 1 cm Si/SiO<sub>2</sub> substrates was used as purchased from Graphenea (Cambridge, MA). Devices were fabricated by performing standard photolithography to define interdigitated electrode contacts. A Temescal BJD-1800 electron beam evaporator was used to deposit Ti/Au (25 nm/300 nm), followed by successive soaking in acetone, isopropanol, and deionized water to achieve metal lift-off. The interdigitated electrode pattern consisted of 16 fingers with length 1000 μm, width 50 μm, and separation of 50 μm, for a total sensor area of 0.8 mm<sup>2</sup>. After nitrogen drying, the patterned device was mounted in a 68-pin leadless chip carrier and manually wire bonded. The bonded device was loaded into a 68-pin breakout board outfitted with a custom-

machined Teflon block to provide a low volume flow channel of 0.25 mL to the sensor surface. The entire sampling process was automated using a custom headspace sampling system, where the sensor was brought to the opening of a 40 mL vial containing the desired analyte as soon as the vial was unsealed. Each measurement was conducted under ambient laboratory conditions for temperature and humidity, with each repeated measurement carried out under identical experimental conditions. A Keithley 2450 (Cleveland, OH) source meter was used for resistance measurements collecting data at approximately 14 Hz. A Python script was used to read a user-generated input CSV file specifying the measurement parameters for a single measurement. The parameters include: baseline time, sample time, recovery time, bias voltage, and sample flow rate. In this manner, many repetitions could be performed in a standardized and reproducible way, generating large volumes of highly reproducible data. All post processing, data analysis, and plotting was performed using Python 2.7 with scipy, numpy,<sup>8</sup> pandas,<sup>9</sup> scikit-learn,<sup>10,85,86</sup> and matplotlib<sup>12</sup> modules.

One of the primary components of a prediction model is providing meaningful and informative features to the classification algorithm so it may be properly trained. This process, commonly referred to as feature engineering, is one of the most important and challenging tasks in the fields of pattern recognition, data mining, machine learning, and predictive modeling in general.<sup>104</sup> Ranking features according to importance can aid in the feature engineering process by highlighting the factors which directly impact the classification accuracy. A random forest is an ensemble method which combines several individual decision trees. This ensemble method provides a feature importance measure and has been shown to be a sensible means for variable selection in many applications.<sup>105</sup>

## 5.4 Data Processing

For each measurement, resistance values were computed with the applied bias voltage and measured current from the Keithley 2450 source meter. The start and stop times for each sample were stored during each measurement, and were subsequently used to automatically calculate the maximum change in resistance ( $\Delta R$ ), area of the response during sampling ( $A_S$ ), and area of the response during recovery ( $A_R$ ). The start and stop points also provided bounding points for applying exponential fitting models to correctly fit the sample and recovery portions of the response. Preprocessing procedures included correcting for drift using a first order linear fit to the baseline points, and calculating fractional change in resistance.<sup>4</sup> The illustration in Figure 5.1 shows the regions of a typical response to a chemical analyte, where the response is presented as change in resistance over time. The baseline period represents the period during which room air flows over the sensor without any analyte present. The sampling period occurs when the sensor head is lowered into the headspace of an open vial and the headspace vapor flows over the sensor at the same flowrate as in the baseline period. The recovery phase begins when the sensor head is removed from the vial headspace and room air again flows over the sensor. Various features are extracted from each response curve and used as discriminators in further data exploration, discrimination, and classification. The maximum change in resistance is calculated by taking the difference between the maximum signal value and the average value of the baseline resistance. The area for each of these regions is calculated by using the trapezoidal rule to approximate the area under the curve for that region. The area of the sample region was calculated between points  $t_a$  and  $t_b$ , which represent the start and stop of

the sampling period, while the area of the recovery region was calculated between points  $t_b$  and  $t_c$ , which represent the start and stop of the recovery period. Exponential fitting models were applied to the sample and recovery portions of the response using Equations 6 and 7, respectively. The features extracted from the fitting of the sample region were  $\alpha_S$ ,  $\beta_S$ , and  $\gamma_S$ , while those extracted from the fitting of the recovery region were  $\alpha_R$ ,  $\beta_R$ , and  $\gamma_R$ .

$$R_S(t) = \alpha_S(1 - e^{-\beta_S t}) + \gamma_S \quad (6)$$

$$R_R(t) = \alpha_R e^{-\beta_R t} + \gamma_R \quad (7)$$

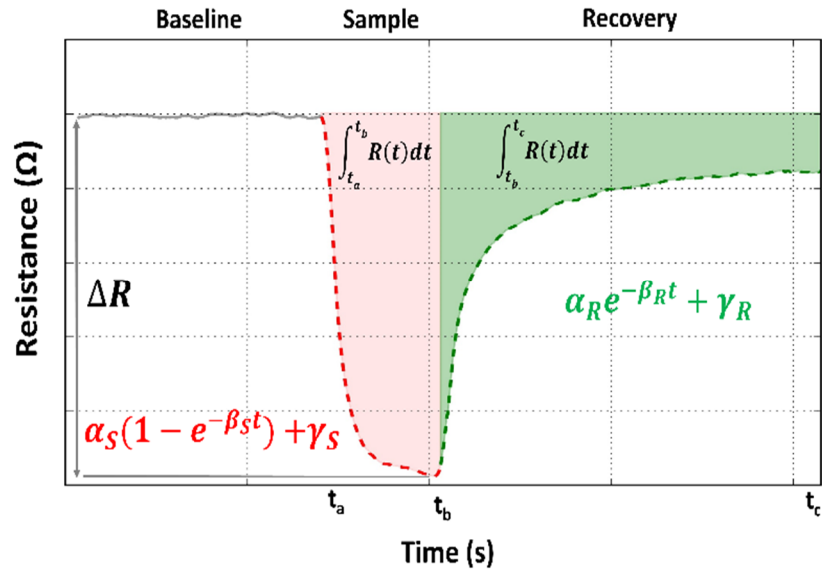


**Figure 5.1** Typical sensor response curve with regions I) baseline, II) sample, and III) recovery. Features include the maximum change in resistance ( $\Delta R$ ), area of the response (red shaded area), area of the recovery (green shaded area), and exponential fitting coefficients from the sample ( $\alpha_S$ ,  $\beta_S$ ,  $\gamma_S$ ) and recovery ( $\alpha_R$ ,  $\beta_R$ ,  $\gamma_R$ ) regions.

## 5.5 Results and Discussion

### Sensor Response: Chemically and Structurally Similar Compounds

The response of the sensor was tested by continuously measuring its resistance during exposure to four chemically and structurally similar compounds: mesitylene, o-xylene, p-xylene, and toluene. These analytes are shown in Table 5.1, along with their structure, formula, mass, and vapor pressure. The sensor was biased at a constant voltage of 10 mV and the current recorded continuously for each individual measurement, from which the resistance change was calculated. The baseline, sample, and recovery times were set to 60 s, 30 s, and 120 s, respectively, with a flow rate of 10 mL/min. This procedure was repeated eighteen times for each compound in a randomized order under the same experimental conditions. The calculated fractional change in resistance for all eighteen measurements for each analyte is shown in Figure 5.2.

**Table 5.1** Chemical information for mesitylene, o-xylene, p-xylene, and toluene.

Compound	Symbol	Formula	Molar Mass (g/mol)	Vapor Pressure (mmHg)
Mesitylene		C <sub>9</sub> H <sub>12</sub>	120.19	2
o-xylene		C <sub>8</sub> H <sub>10</sub>	106.19	7
p-xylene		C <sub>8</sub> H <sub>10</sub>	106.19	9
Toluene		C <sub>7</sub> H <sub>8</sub>	92.14	21

The eighteen repetitions for each compound exhibit significant overlap among their response magnitudes. A particularly large amount of overlap can be seen between o-xylene, p-xylene, and toluene. It is not surprising that the sensor response to o-xylene and p-xylene is similar, as they are structural isomers with identical molecular weight and similar vapor pressure. The maximum change in resistance will be influenced by these variations, and other features such as calculated areas will also inherit these variations, since they are based on the maximum steady-state change. This inter-dependence of higher-order features can subsequently lead to confusion for further separation and discrimination analysis.

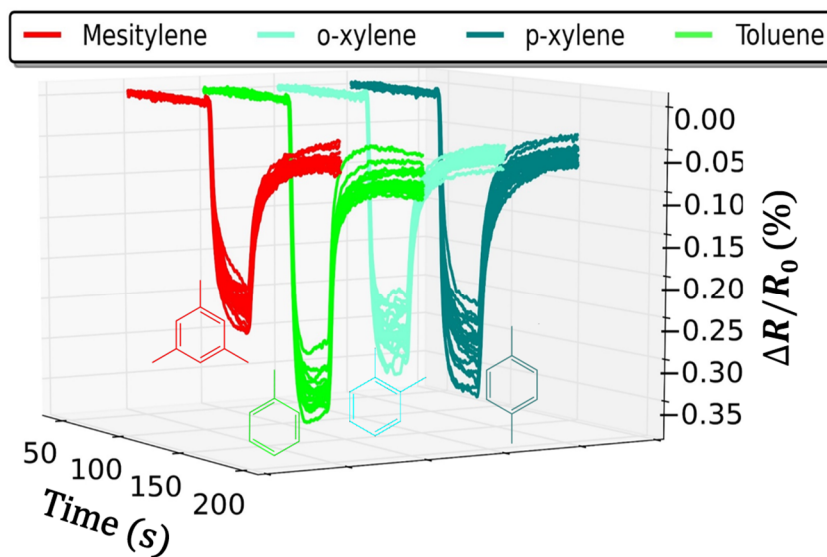


**Figure 5.2** Sensor response to a group of analytes highlighting the overlap that can be encountered between responses.

## Transient Fitting Methods

The sample and recovery portions described in Figure 5.1 have characteristic transients which are well fit by a first-order exponential. For every compound, the sensor response for each of the eighteen measurements was normalized by the  $\ell^2$  norm shown in Equation 8.

$$\ell_{norm}^2 = \sqrt{\sum_{k=1}^n |x_k|} \quad (8)$$

After normalization, the sample and recovery portions of each response were fit according to the first-order exponential models shown in equation 6 and equation 7, respectively, using a non-linear least squares optimization. Figure 5.3 provides a summary of the exponential fit for each sensor response, a comparison of importance for each feature, and the mean and standard deviation (STD) values of each feature. Figure 5.3a displays a plot of the exponential fit for each response during both the sample and recovery phase of the measurement. Visually, a clear distinction can be seen between mesitylene and o-xylene. Toluene and p-xylene appear to have very similar fits during the sample phase, but have differing trajectories during the recovery phase. For each fit applied to the sample and recovery phase the extracted coefficients were  $\alpha_S, \beta_S, \gamma_S$ , and  $\alpha_R, \beta_R, \gamma_R$ , respectively.

To evaluate the relative importance of the feature data generated in this work, a feature vector consisting of a combination of the fitting coefficients ( $\alpha_S, \beta_S, \gamma_S, \alpha_R, \beta_R$ , and  $\gamma_R$ ) and the maximum change based parameters ( $\Delta R, A_S$ , and  $A_R$ ) was created and then fit to an optimized random forest classifier, producing a set of feature importance weights associated with the highest classification accuracy. In Figure 5.3b the features are shown on the x-axis with their respective feature importance shown on the y-axis in percent. The

features shown in red ( $\Delta R$ ,  $A_S$ , and  $A_R$ ) account for 16% of the total feature importance, with most of that percentage dominated by  $\Delta R$ . Although the calculated areas,  $A_S$  and  $A_R$  provide discriminative information, their higher standard deviations, as we will soon see, may hinder their usefulness. The rest of the features, shown in green, consist of the exponential fitting terms and together account for 84% of the total feature importance, with the exponential coefficients  $\beta_S$  and  $\beta_R$  ranked most important in both the sample and recovery phase. To further demonstrate the potential advantages of the fitting terms, Figure 5.3c summarizes the mean and standard deviation for each feature, calculated from each compound's eighteen repetitions. The largest STD values arise from the sample and recovery areas, which are also reflected in the random forest feature importance. The lowest STD values appear mostly in the three fitting terms from the recovery phase. The STD is a meaningful evaluation metric, since these features are used to eventually train the algorithm, and a large STD can lead to overlap between feature values and ultimately result in confusion during further discrimination and classification.

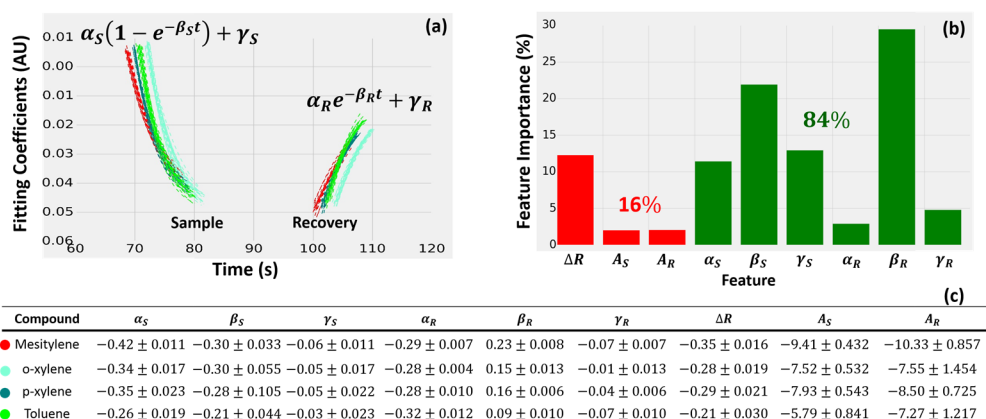


**Figure 5.3** a) Plotted fitting coefficients for each compound, b) feature importance weights for each feature determined by a random forest classifier, and c) standard deviation values for each feature.

## Physicochemical Relationships

The exponential nature of the sensor response can be modeled with a solid-gas adsorption and desorption process which can be related to physical/chemical properties of the compounds. The simplest form of adsorption was derived by Langmuir using kinetic theory where solid-gas surface adsorption kinetics are a product of the surface coverage and the molecular flux of the compound.<sup>106</sup> This process can be described by Equation 9, where  $(1 - \theta)$  is the fraction of sites not covered,  $s^*$  is a sticking coefficient term,  $P$  is pressure,  $N_A$  is the Avogadro constant,  $T$  is temperature,  $m$  is mass,  $R$  is the gas constant, and  $E_{ads}$  is the activation energy of adsorption. Since the device surface area is fixed, and the temperature and pressure are held constant in this experiment, the pre-exponential becomes a function of the mass. When the constants are separated, the pre-exponential frequency term then varies as  $1/\sqrt{m}$ . Figure 5.4a shows the relationship between the mass of each tested compound and the calculated pre-exponential term  $\alpha_S$ , from the sample phase

of the response, where the x-axis shows each compound, and the y-axis shows both  $1/\sqrt{m}$  and  $\alpha_s$  values. A correlation coefficient of 0.9893 was calculated between these two parameters, indicating they have a strong positive correlation. This appears to hold true even for o-xylene and p-xylene, which are structural isomers and consequently have the same mass, and an almost identical fitting term.

$$\text{Rate of Adsorption} = \frac{PN_A}{\sqrt{2\pi mRT}} (1 - \theta) s^* e^{-\frac{E_{ads}}{RT}} \quad (9)$$

In a similar manner, Figure 5.4b shows the relationship between each compound's vapor pressure and the calculated exponential term  $\beta_R$  from the recovery phase of the response, where the x-axis again represents each compound and the y-axis shows both the vapor pressure and  $\beta_R$ . The modeled Langmuir rate of desorption can be expressed by Equation 10, where  $k_d$  is a desorption rate constant,  $\theta$  is the fraction of sites occupied, R is the gas constant, T is temperature, and  $E_{des}$  is the activation energy of desorption. In this case we are showing the relationship between the exponential fitting term and the desorption rate, which is also described by an exponential. For the four compounds tested, a correlation coefficient of 0.9844 was calculated between these two parameters indicating they also have a strong positive correlation.

The greater complexity of desorption seen in this work between isomers of xylene on graphene is mirrored by the desorption process of butane isomers on silicon. The conformation difference of the butane isomers has a minor importance in the adsorption kinetics, but steric conformation effects were responsible for a difference in the stability of

the adsorbed layers, leading to differences in the desorption process.<sup>107</sup> The strong correlation between the measured exponential coefficients and the known analyte masses suggest that this system is accurately modeled by the Langmuir isotherm, with an activation energy of desorption higher than that of adsorption. Evidence of this adsorption behavior can be seen in Figure 5.4a, where the diffusion based adsorption of the xylene isomers on the graphene surface doesn't change mass, which is the same for the two isomers. Desorption is a more complex process that is governed by a multitude of interactions, including surface-molecule and molecule-molecule interactions which have a steric dependence. The complexity of the desorption reaction is suggested in Figure 5.4b by the varying values for the two xylene isomers despite their identical masses.

$$\text{Rate of Desorption} = k_d \theta e^{-\frac{E_{des}}{RT}} \quad (10)$$

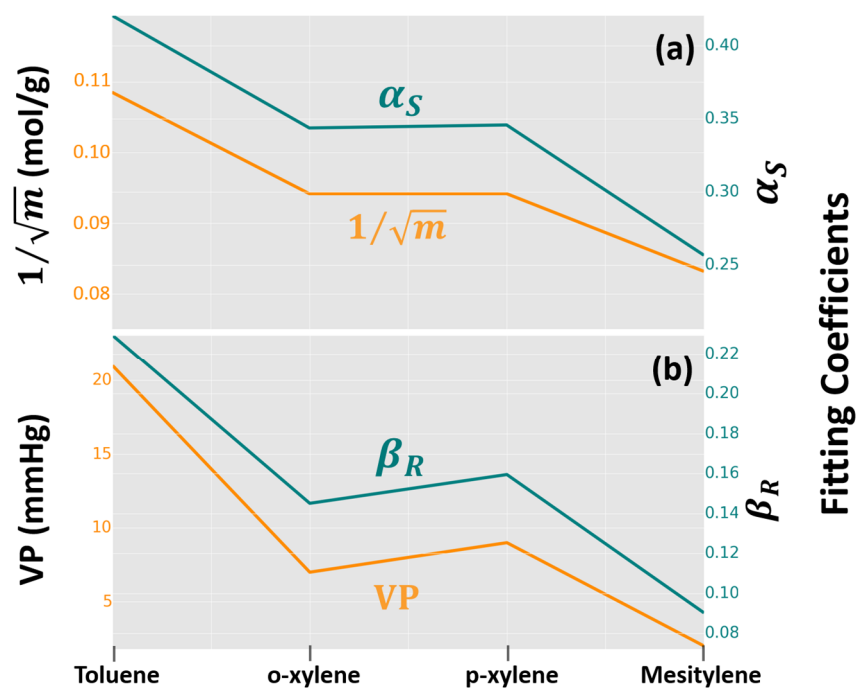


**Figure 5.4** Relationship between a) compound mass ( $1/\sqrt{m}$ ) and adsorption frequency factor fitting term ( $\alpha_S$ ) and b) vapor pressure (VP) and desorption exponential fitting term ( $\beta_R$ ).

## 5.6 Discrimination and Classification

To demonstrate the effectiveness of using exponential fitting coefficients as discrimination features, a PCA transformation was performed on the described data set. Figure 5.5a shows the PCA transformation of a feature vector containing the  $\Delta R$ ,  $A_S$ , and  $A_R$  features extracted from the responses in Figure 5.2. Mesitylene is the only compound that appears to form a noticeable group. This is not surprising since its magnitude of response is the lowest and its variation in response does not overlap much with the other compounds. On the other hand, toluene, o-xylene, and p-xylene form a large cluster, with all three compounds almost equally distributed. Figure 5.5b shows a PCA transformation containing

the first three principal components of a feature vector containing the same features as those used in Figure 5.5a, but supplemented with the  $\alpha_S$ ,  $\beta_S$ ,  $\gamma_S$ ,  $\alpha_R$ ,  $\beta_R$ , and  $\gamma_R$  fitting coefficients. The PCA transformation was performed in an identical manner and viewed from the same frame of reference. Visual comparison of the two PCA plots clearly shows significantly better grouping and separation of the four compounds, with the most overlap seen between o-xylene and p-xylene. The larger separation between compounds and tighter grouping within each group result from the additional information provided by the fitting coefficients and the smaller STD values associated with each.

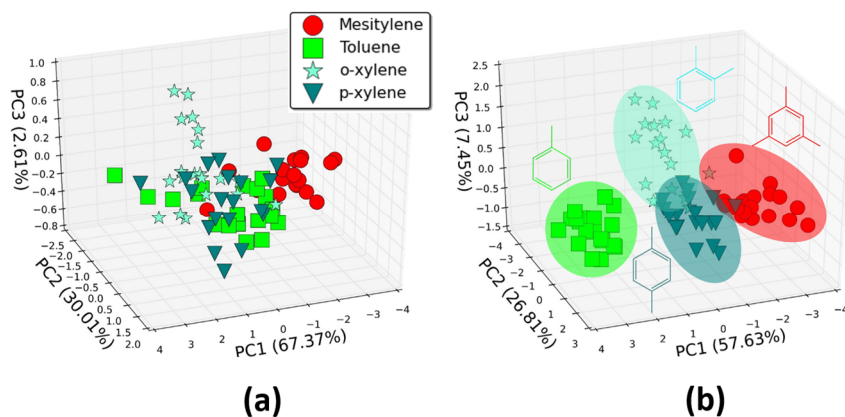


**Figure 5.5** PCA transform for a feature vector containing a)  $\Delta R$ ,  $A_S$ ,  $A_R$  and b) supplemented exponential fitting coefficients  $\alpha_S$ ,  $\beta_S$ ,  $\gamma_S$ ,  $\alpha_R$ ,  $\beta_R$ , and  $\gamma_R$ .

The comparison in Figure 5.5 indicates that including exponential fitting coefficients in the feature vector provides better grouping and separation among the compounds. Although this looks promising visually, it is worth performing a similar comparison using classification accuracy as the metric. The three classifiers used were k-nearest neighbors

(kNN), random forest, and linear discrimination analysis (LDA). The entire data set collected for this analysis consisted of 72 samples (4 compounds, 18 repetitions each). In order to avoid overfitting, k-fold cross-validation ( $k = 10$ ) was performed with a training size of 50%, producing train and test sets with 36 measurements each. The results from each classifier's prediction accuracy are summarized in Figure 5.6. Compared to a feature vector containing the fitting coefficients, a feature vector containing only  $\Delta R$ ,  $A_S$ , and  $A_R$  exhibits a lower classification accuracy for each classifier type. Further comparison of the results show that for kNN, random forest, and LDA the classification accuracy increased by 39%, 23%, and 34%, respectively. The improved classification accuracy is mostly attributed to decreased misclassifications of toluene, o-xylene, and p-xylene.

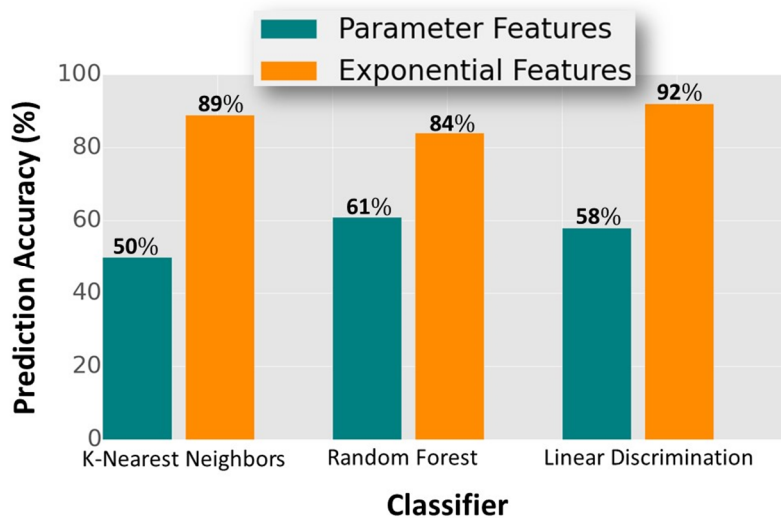


**Figure 5.6** Classification accuracy comparison using parameters features only and supplementing with transient features from exponential fitting.

## 5.7 Conclusions

Traditional feature engineering methods for chemical sensor analysis based on maximum change are subject to fluctuations such as concentration variations and drift caused by sensor aging. Time-dependent features can be extracted from the same response curve by exponential fitting, where the fitting coefficients are directly used as additional discriminators. In this work, a comparison between feature vectors with and without exponential fitting coefficients by PCA clearly showed an excellent improvement in separation between chemically and structurally similar analytes. This technique was further validated by comparing prediction accuracies produced while using each feature vector. The addition of the exponential fitting coefficients resulted in improvement of classification accuracy across three separate classifiers. Additional research in the area of simulations and surface analysis could provide additional insights of the mechanisms involved between chemical vapors and the graphene surface. These results demonstrate a robust method to extract features from time based chemical response data, which could be applied to individual sensors, or sensor arrays of various sensor types.

# Chapter 6 Surface Functionalization of Graphene for Sensor Applications

## 6.1 Types of graphene modification

The pure carbon structure of graphene provides a platform for surface functionalization with many possibilities. Generally speaking, functionalization of graphene can be separated into three approaches: covalent, noncovalent, and immobilization. Covalent functionalization of the graphene surface involves the direct attachment of organic or inorganic groups to the graphene surface. This type of functionalization is destructive in the sense that the  $sp^2$  bonding is changed to  $sp^3$ , disrupting the aromatic bonding, and can dramatically change electrical and other properties. Figure 6.1 illustrates the difference between noncovalent and covalent functionalization, highlighting the disruption of the carbon  $sp^2$  bonding to form  $sp^3$  bonding.<sup>108</sup> Many covalent methods exist and some of the most widely reported methods consist of cycloaddition reactions, addition of free radicals, organometallics, biopolymers, antibodies, and nucleic acids. Noncovalent functionalization offers an approach to retain the extraordinary properties of graphene while inducing additional desirable properties. The exposed  $\pi$ -electrons of graphene can be exploited to form this bond, while not disturbing the  $sp^2$  hybridization of the carbon bonding which attributes to much of graphene's properties. Some noncovalent functionalities are made possible through  $\pi$ - $\pi$  stacking, electrostatic interactions, and hydrogen bonding include polycyclic molecules, biomolecules, polymers, and other organic/inorganic molecules. Related to noncovalent functionalization, but often categorized separately, is immobilization. An important immobilization technique that can be applied to graphene, with applications in

sensor applications, is the use of metal and metal oxide nanoparticles. It is generally accepted that the extraordinary properties of graphene might enhance the effects of nanoparticles in the composite material.<sup>109</sup>

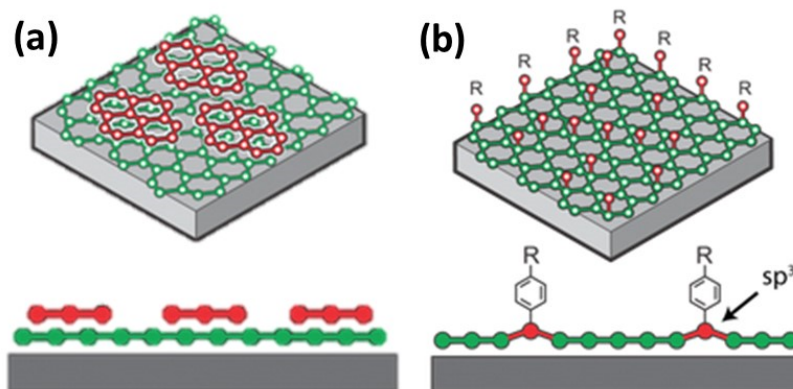


**Figure 6.1** a) Noncovalent and b) covalent functionalization of graphene.<sup>108</sup>

## 6.2 Oxygen plasma modification

The treatment of graphene with a plasma is a simple, fast, and scalable process, which can be easily integrated into common semiconductor fabrication production lines.<sup>110</sup> It also does not require new or highly specialized equipment, as much of the equipment already in use for reactive ion etching and plasma cleaning processes would be cross-compatible. Plasmas can be generated from commonly used gases such as oxygen, hydrogen, nitrogen, and other fluorinated gases. For the application of using graphene in semiconducting devices, this process could be used to functionalize the graphene surface in order to induce a band-gap. From the perspective of the work presented here, this same

surface functionalization can be used to modify the graphene surface in order to gain sensitivity or selectivity. The Raman spectra of monolayer graphene contains two main peaks: the G-band around  $1580\text{ cm}^{-1}$  and the 2D-band around  $2700\text{ cm}^{-1}$ . After oxygen plasma exposure, new features emerge due to defect activation with the most prominent bands appearing at  $\sim 1340\text{ cm}^{-1}$  and  $1620\text{ cm}^{-1}$ , corresponding to the D-band and D'-band, respectively.

Before testing oxygen functionalized graphene as a chemical sensor, a series of graphene samples were subjected to an oxygen plasma for different amounts of time. Four single-layer graphene samples were cleaved, where three were subjected to an oxygen plasma at a power of 15 W and a pressure of 1.5 Torr for 60 s, 90 s, and 180 s. The remaining piece was used as a control sample. Shown in Figure 6.2 is the Raman spectra for pristine single-layer graphene, along with single-layer graphene which has been treated with an oxygen plasma for 60 s, 90 s, and 180 s. The D-band shows the largest increase for the 60 s exposure, then a decrease for 90 s exposure which eventually turns into a complete lack of signal for 180 s exposure. As the exposure time increases, the intensity of all relevant bands decreases, and for the 180 s exposure no peaks are present indicating most likely destruction of the graphene layer. The most prominent feature, besides that of the D-band increase, is the appearance of a D' peak on the side of the G-band.

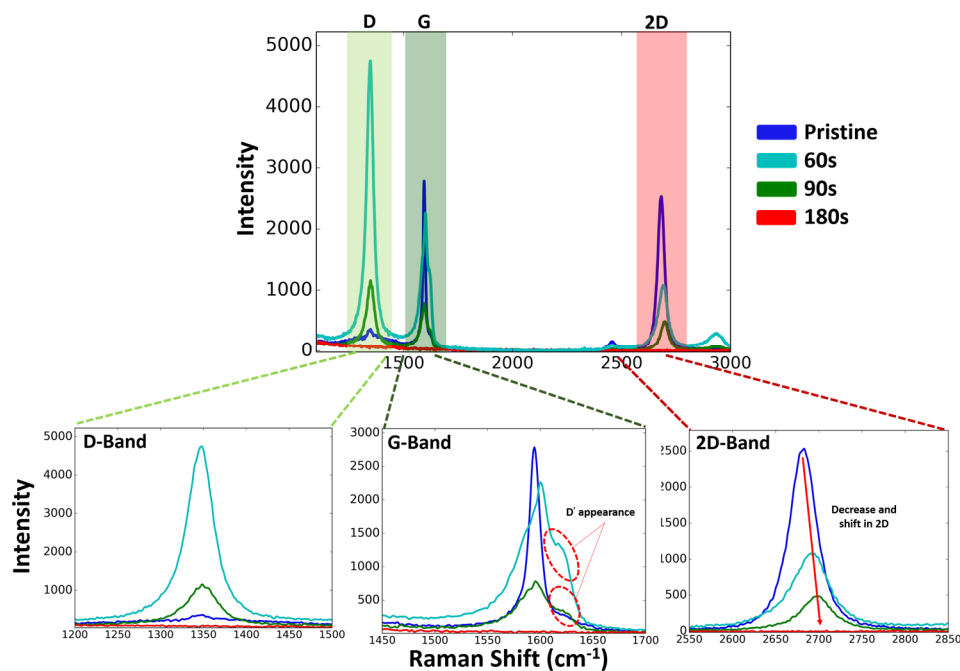


**Figure 6.2** Raman spectra of single-layer graphene subjected to oxygen plasma for different amounts of time.

Based on the previous oxygen plasma exposure study, a SLG sensor was exposed to an oxygen plasma at a power of 15 W and a pressure of  $\sim 1.5$  Torr for 60 s. The sensor, along with a reference sensor cleaved from the same piece before oxygen plasma exposure, was tested against the vapors of various chemicals. Some of the most notable sensor response differences are shown in Figure 6.3 for 3-nitrotoluene, 4-chlorotoluene, chlorobenzene, and nitrobenzene. Each of these compounds are nitro- and chloro-containing aromatic compounds and the change in sensor response between the modified and unmodified sensors was significant, with a change of 18%, 11%, 8.5%, and 15% for 3-nitrotoluene, 4-chlorotoluene, chlorobenzene, and nitrobenzene, respectively.

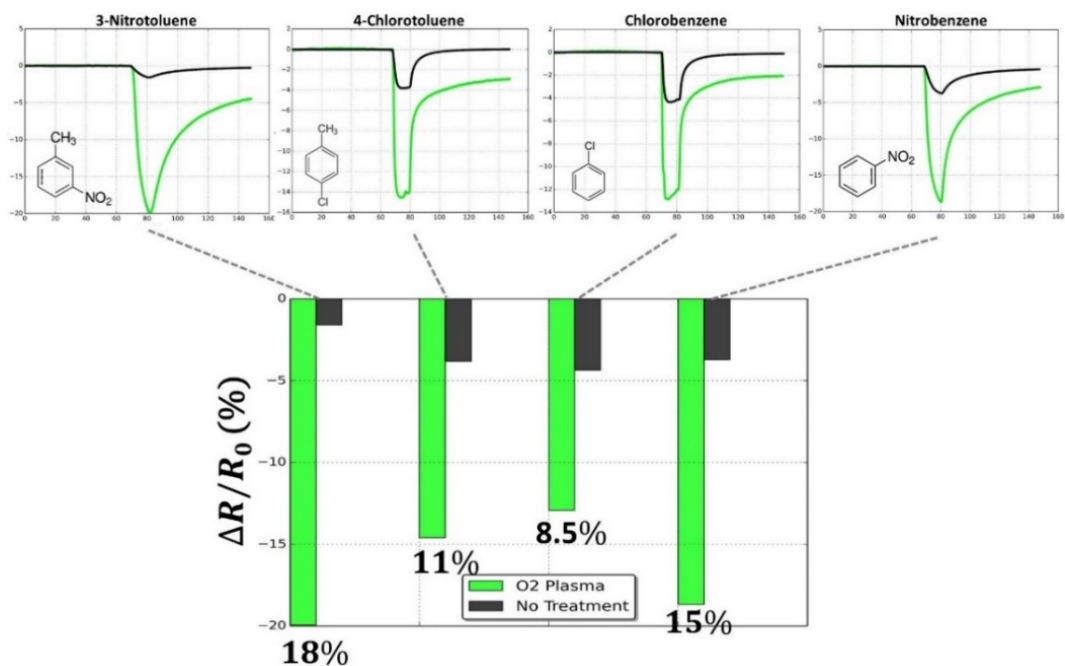


**Figure 6.3** Comparison of oxygen plasma treated sensor response to 3-nitrotoluene, 4-chlorotoluene, chlorobenzene, and nitrobenzene.

Three other interesting examples for the oxygen plasma treated sensor are for exposure to phenol, 4-chlorophenol, and 4-chloroaniline. As shown in Figure 6.4, the untreated sensor has little to no response when exposed to these compounds, but the oxygen plasma treated sensor exhibits a significant response towards these compounds.

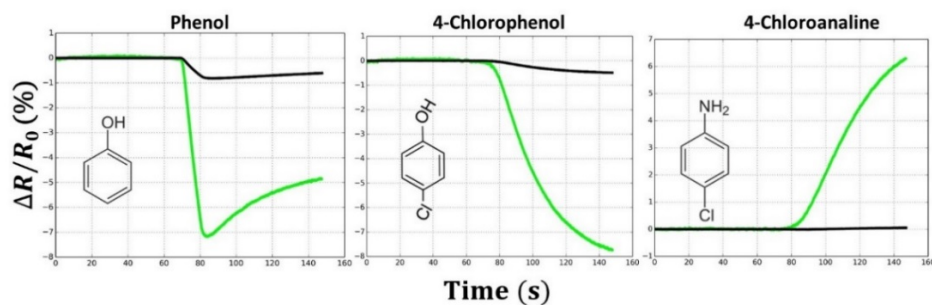


**Figure 6.4** Comparison of oxygen plasma treated sensor response to phenol, 4-chlorophenol, and 4-chloroaniline.

The reasons for the observed response behavior may be attributed to a combination of plasma induced defects to the graphene lattice, and also the addition of oxygen functionalities, causing increased sensitivity to certain compounds. A SEM image of the oxygen treated graphene sensor is shown in Figure 6.5 and appears to show a network of defects that appear to be connected to each other. This image, along with the previous Raman spectra measurements, points towards plasma induced defects as the likely outcome of the oxygen plasma treatment.

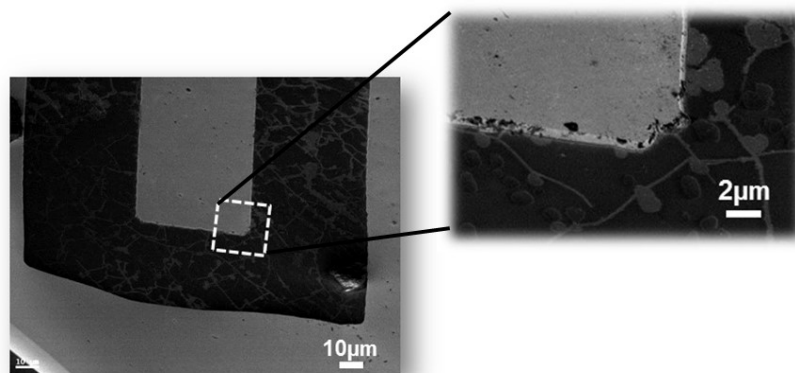


**Figure 6.5** SEM image of graphene sensor treated with an oxygen plasma for 60s at 10 W.

### 6.3 Modification with Diazonium Compounds

Free radicals are very reactive organic intermediates, and are capable of attacking the  $sp^2$  carbon atoms found in graphene to form covalent bonds.<sup>109</sup> One such compound group capable of producing a free radical and also containing various functional groups are diazonium compounds. These compounds are capable of covalently attaching to the graphene surface via an electron transfer mechanism. The reaction occurs when a delocalized electron is transferred from the graphene to the aryl diazonium cation, which becomes an aryl radical after releasing a molecule of  $N_2$ . The radical then forms a covalent bond with a carbon atom in the graphene lattice, changing its hybridization to  $sp^3$  and displacing it out of the graphene plane.<sup>111</sup> Diazonium salts provide many functional groups that can be used to change the surface energy of graphene or other materials. Some of the potential functional groups and their relative dipole moments are shown in Figure 6.6 and include nitro, bromo, chloro, di-chloro, and methoxyl with dipoles 3.9, 1.6, 1.7, 1.8, and -0.3,

respectively.<sup>112</sup> Creating a sensor array consisting of individual sensors with varying surface dipole moments could be an attractive approach to a cross-reactive array.

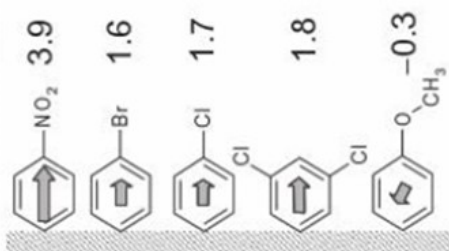


**Figure 6.6** Various diazonium compound functional groups with their relative dipole moments.<sup>112</sup>

Following the methods of Sharma et al.<sup>113</sup>, a SLG sensor was functionalized with 4-nitrobenzene diazonium tetrafluoroborate (NBD) and tested against various compounds, along with a control sensor cleaved before functionalization. For the reaction solution, 200 mL of 1% sodium dodecyl sulfate was combined with 20 mM NBD and heated to 35 – 45 °C. The sensor sample was submerged in the reaction solution for ~12 h with constant stirring. Many accounts of diazonium functionalization have been reported and include Raman spectroscopy to quantify covalent attachments of the compound to the surface.<sup>111,114–116</sup> Raman spectra were taken on an un-treated control sample and an NBD treated graphene sensor. The measured spectra for both samples can be seen in Figure 6.7, where a very strong D-band peak and also a D'-band feature are revealed. The high intensity of the D-band indicates a large number of defects are present, but can be difficult to tell if they are due to  $sp^3$  modifications to the graphene lattice or vacancy type defects. Recent

research suggests that the intensity ratio of the D and D' peak is maximum ( $\sim 13$ ) for  $sp^3$ -defects, decreases for vacancy-like defects ( $\sim 7$ ), and it reaches a minimum for boundaries in graphite ( $\sim 3.5$ ).<sup>52</sup> The calculated ratio of the D to D' peaks for the NBD modified graphene gives a value of 5.74, which according to this, would classify it as vacancy-like defects.

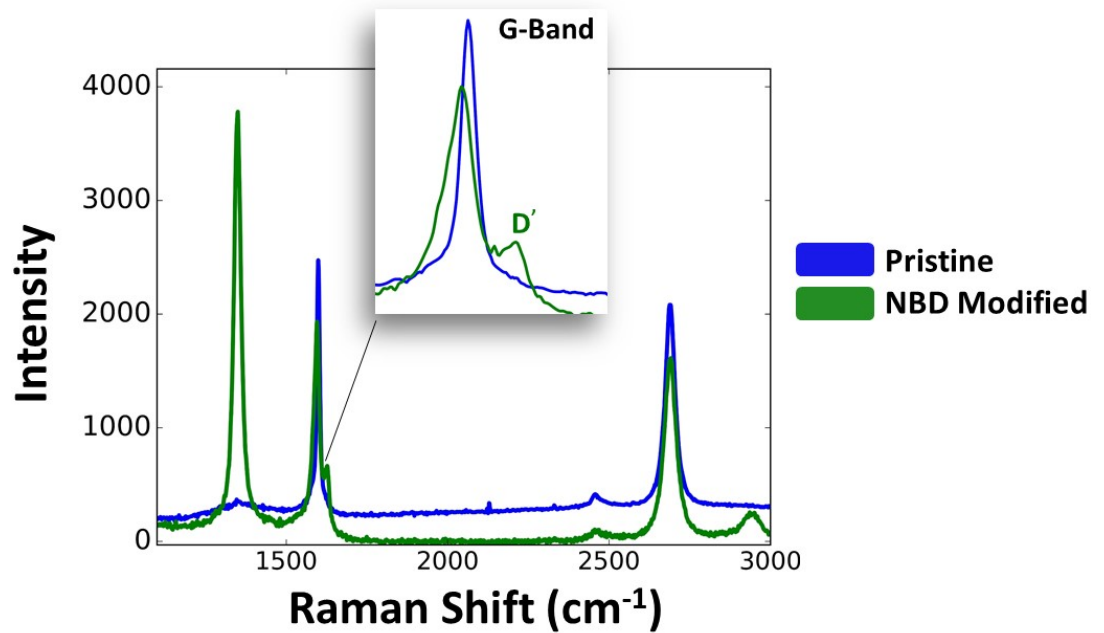


**Figure 6.7** Raman spectra of graphene sensor modified with nitrobenzene diazonium tetrafluoroborate.

Following the reaction time period, the sensor was rinsed with deionized water, then mounted and wire bonded in an LCC, along with the control sensor for direct comparison. Shown in Figure 6.8 is the sensor response comparison for unmodified and NBD-functionalized SLG sensors. The sensors were exposed to acetone, tetrahydrofuran (THF), dimethyl sulfoxide (DMSO), toluene, nitrotoluene, and acetonitrile.

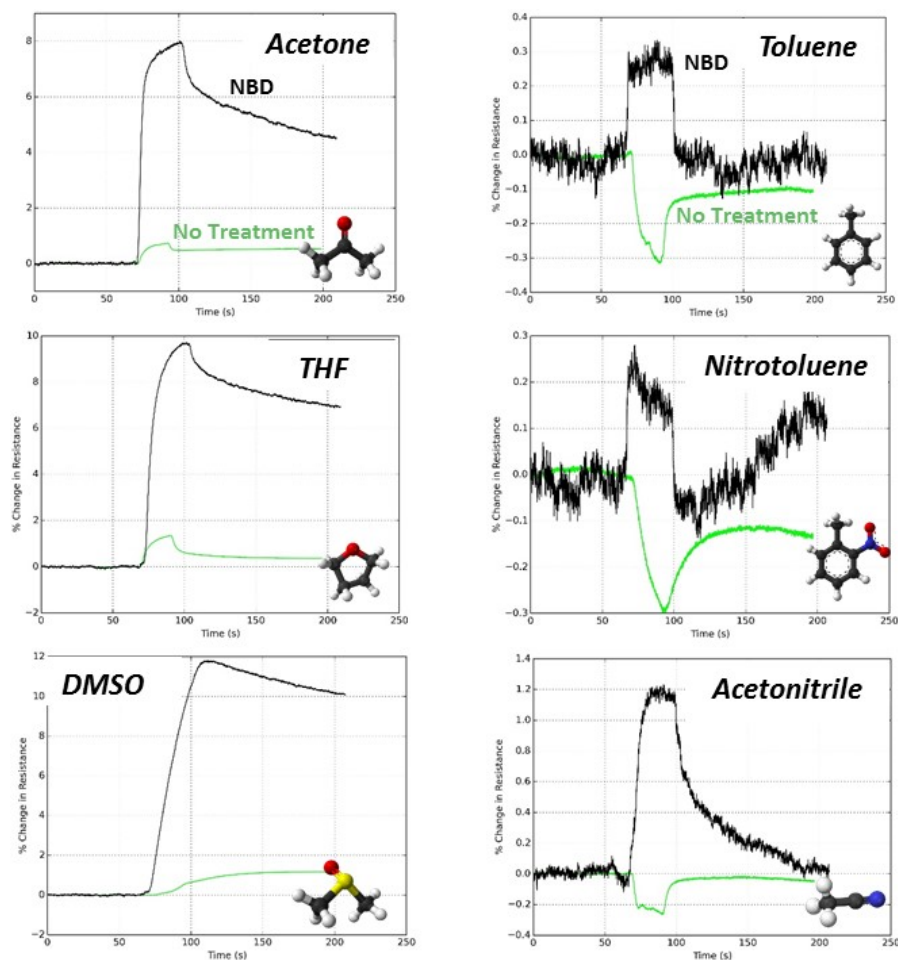


**Figure 6.8** Response comparison of an unmodified and NBD-functionalized SLG sensor.

## 6.4 Polymer modification

Polymers cover a wide field of chemistry and many types can be synthesized for multiple applications. The use of polymers in chemical sensor related applications is highly confined to carbon black-polymer composites,<sup>117</sup> quartz-crystal microbalances,<sup>118</sup> and acoustic wave devices.<sup>119</sup> The polymer in these devices adds diversity when configured in a

sensor array format by taking advantage of the different physiochemical properties of the polymer, which affect the interaction of the chemical compound with the sensor. The selection of polymers for use in sorption based chemical sensors is commonly approached by considering the linear solvation energy relationships (LSER) of the polymer and analytes, and has been extensively modeled. The LSER model is based on a linear combination of solvation parameters consisting of the effective hydrogen-bond acidity, hydrogen bond basicity, dipolarity/polarization parameters, and dispersion parameter.<sup>120</sup> Polymers are usually soluble in a variety of polar and non-polar solvents, depending on their structure and properties. From a manufacturing standpoint, this offers a flexible way to deposit or incorporate polymers with sensors by technique such as spin-casting, spraying, drop-casting, and stamping. For deposition of a single polymer over an entire substrate, spin-coating is a simple procedure capable of producing large area uniform films with the ability to control film thickness by the spin speed and spin time. Figure 6.9 illustrates SEM images of five different polymers solutions cast from a 5 mg/mL chloroform solution directly onto the graphene sensor electrode array. Overall, the images indicate a uniform coating of each polymer, but for polymer 4 and polymer 5, larger chunks of the solid polymer are present, most likely due to not being completely solvated in the chloroform. This is particularly evident in the higher magnification image for polymer 5 where multiple chunks of polymer are almost as wide as the 25  $\mu\text{m}$  metal trace. The image of polymer 3 also shows an interesting detail; a pattern emerges at the edges of the metal electrode, and when it meets the graphene layer, it appears to align with the direction of the outward spinning of the polymer at that point.

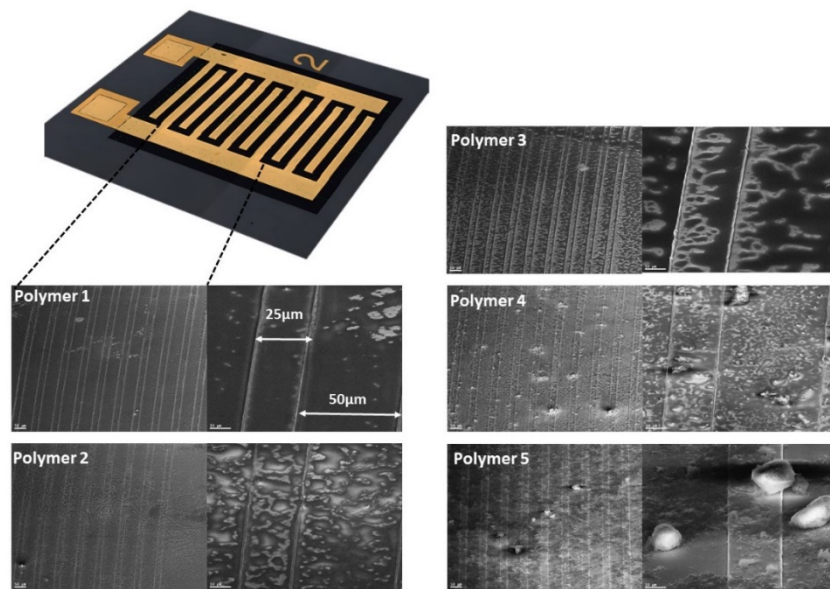


**Figure 6.9** SEM images of five different polymers spin-cast from a chloroform solution over the graphene sensor electrode array.

Although spin-cast deposition of polymers can produce uniform films, it is not feasible to use this technique to deposit multiple polymers on a single substrate without interference among polymers. For a sensor array, such as those used in an electronic nose, single element devices are usually fabricated on the same substrate, eliminating spin-casting as a polymer deposition method. Shown in Figure 6.10a is a sensor array consisting of 24 identical devices with routed bonding pads. Each device consists of 12 finger-like electrodes with a spacing and width of 25  $\mu\text{m}$  each. Shown in Figure 6.10b is a second mask used with SU8 negative photoresist to create a permanent structure with openings to each sensor and its bonding pads. The SU8 used for this step is thick at approximately 5  $\mu\text{m}$ , which serves

the purpose of creating wells in which polymers can be deposited. The completed device wired bonded to a LCC is shown in Figure 6.10c.

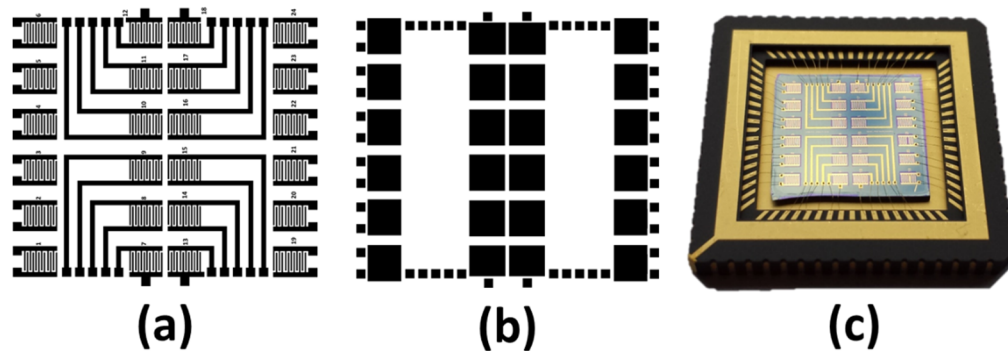


**Figure 6.10** 24-element sensor array a) photolithography metallization mask design, b) photolithography SU8 mask design, and c) completed device in LCC.

To better illustrate the structure of the sensor with the SU8 well, confocal laser scanning microscope images were taken for of a single device. This instrument uses a UV laser and a precision x/y/z stage to create a depth profile of a surface by taking point by point laser measurements. Post-processing software can then be used to create intensity and false color images to represent height changes of the surface. Shown in Figure 6.11 are a color, intensity, and false color height image generated from an Olympus Confocal laser scanning microscope. The color image is taken with a color camera, while the intensity image is generated from the laser measurements, which is used to generate the false color image. The false color image in Figure 6.11c illustrates the various layers of the device structure showing the SiO<sub>2</sub>/Graphene, Ti/Au contacts, and SU8 layer. This image shows more clearly the SU8 layer that creates a well around the sensor area and allows openings for

the bonding pads. The bonding pad openings serve an extra purpose; during wire bonding the metal can remove the graphene from the substrate and this SU8 well helps to anchor the metal at the perimeter and prevent lifting.

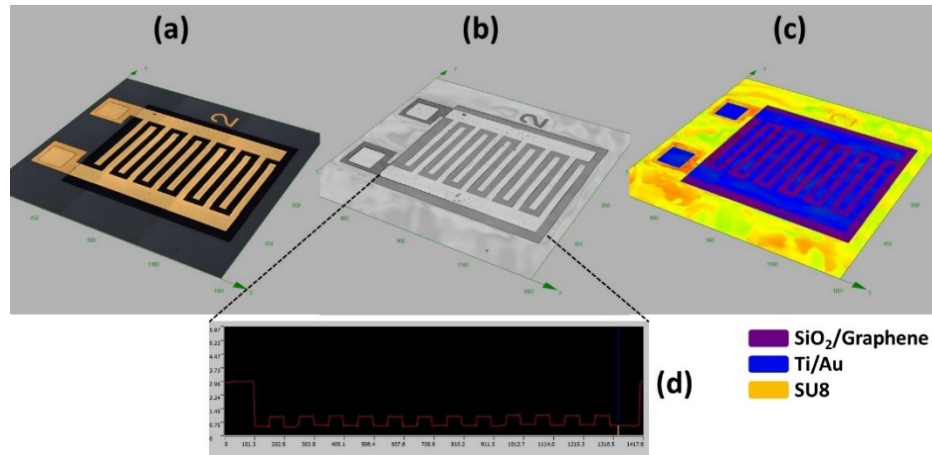


**Figure 6.11** Confocal laser scanning microscope images of a single sensor element in a) color, b) intensity, and c) false height coloring along with the d) step profile along the electrode array.

The addition of the SU8 well to the device design allows for very small amounts of polymers to be deposited via drop-casting from solution. To demonstrate the ability to deposit multiple polymers on a single substrate and the resulting multivariate output sensor response, a sensor array device as show in Figure 6.10c was fabricated and 5 polymers were drop-casted onto individual sensors. The five polymers used were tetraethylene glycol dimethyl ether (TEGDME), poly(dimethylsiloxane-co-alkylmethylsiloxane) (PDMS-Alk), polyethylene glycol (PEG), poly(benzyl methacrylate) (PBMA), and poly(ethylene-co-vinyl acetate) (PEVA). TEGDME and PEG solutions were used as-is, while PDMS-Alk, PBMA,

and PEVA were created at a concentration of 20 mg/mL in chloroform. Individual sensors were created by drop-casting  $\sim 0.4 \mu\text{L}$  of each polymer into separate sensor wells and followed by baking on a hotplate at  $70^\circ\text{C}$  for 5 minutes. Examples of the output response of the five polymer-coated sensors, along with a non-coated control sensor are shown in Figure 6.12. Shown in this figure is the response of the sensor array to chloroform and formaldehyde, which demonstrates the variety of achievable output. For both chloroform and formaldehyde, the polymer-coated sensors provide an output response with either a different sensitivity or selectivity, when compared to the un-coated sensor. The TEGDME and PDMS-Alk coatings cause a reversal in the response direction when exposed to chloroform and the PEG, PBMA, and PEVA coatings provide a reversal in the response direction for formaldehyde. Not only do the coated sensors exhibit signal magnitude and direction differences, but also contain important sorption based information contained in the response and recovery portions of the signal. This combination of information will prove to be very important for further discrimination and classification of complex compounds and odors.

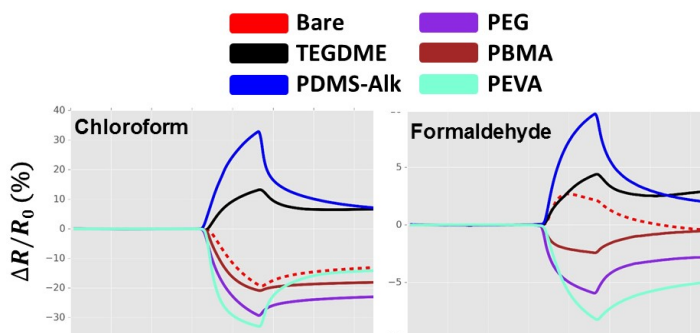


**Figure 6.12** Sensor array output response towards chloroform and formaldehyde for an array containing an un-coated sensor along with 5 polymer-coated sensors.

In Chapter 4, a single graphene sensor without any surface modification was thoroughly evaluated and tested against a variety of VOCs. The prediction accuracy of the sensor peaked at 96% for these compounds, and the misclassification of compounds was due to confusion between toluene and hexane and also between cyclohexanone and diethyl ether. The sensor response towards each of these compounds for each of their 20 measurements is shown in Figure 6.13, where much similarity can be seen between these two pairs of compounds. Cyclohexanone and diethyl ether contain some kinetic information in their response and recovery which may be further exploited to decrease misclassification. On the other hand, hexane and toluene have very similar response patterns in their magnitude, direction, and kinetic shape, making them very difficult to separate from each other. Correct classification becomes increasingly more difficult for a single sensor challenged against compounds with similar chemical and physical properties.

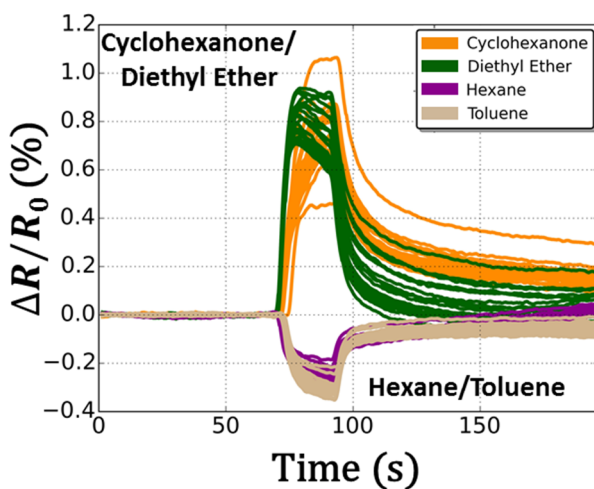


**Figure 6.13** Single graphene sensor without surface modification to cyclohexanone, diethyl ether, hexane, and toluene, highlighting the similar response patterns that cause misclassifications during the classification process.

To demonstrate how increased diversity could be achieved from a sensor array, two polymer coatings were identified for this example which could be used to provide additional information for correctly classifying cyclohexanone, diethyl ether, hexane, and toluene. Shown in Figure 6.14 is the response of sensors with a Polyepichlorohydrin (PECH) and 2-Hydroxyethyl cellulose (OHcell) coating to cyclohexanone, diethyl ether, hexane, and toluene. The sensor coated with PECH shown in Figure 6.14a provides much more diversity for these compounds when compared to the un-coated sensor, especially in the response and recovery kinetics. A disadvantage of using a coating such as this one is the lack of full recovery of the signal over the shown time period. More in-depth testing would also need to be done to optimize the polymer layer thickness to determine if the lack of recovery is related to the thickness. Figure 6.14b shows a sensor coated with OHcell and tested against the same compounds. The most obvious difference when compared against an un-

coated sensor exposed to these same compounds is the reversal in signal direction for cyclohexanone and diethyl ether. Another noticeable difference is the magnitude of the signal for hexane and toluene which is -8.9% and -5.5%, respectively, compared to only -0.2% for the un-coated sensor.

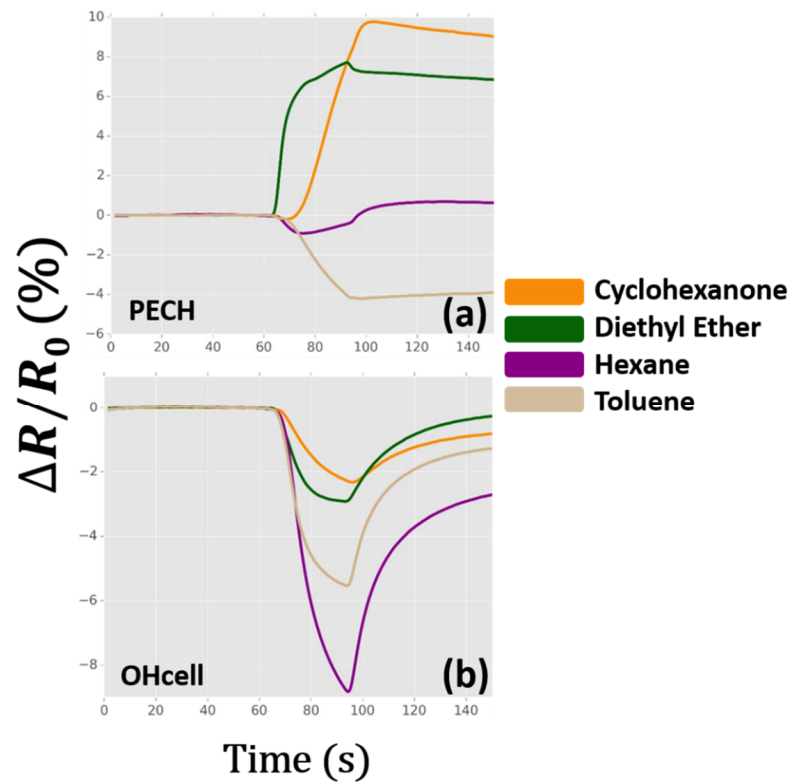


**Figure 6.14** Sensor array output response towards cyclohexanone, diethyl ether, hexane, and toluene.

## Chapter 7 Cross-Reactive Graphene Sensor Array

### 7.1 Abstract

As chemical and biological sensors continue to be integrated into our everyday lives, the demand for a highly dimensional, adaptable sensor array becomes increasingly important. In this work, a cross-reactive, graphene-based chemical sensor array is fabricated and its performance evaluated against single compounds and complex odors. An array of resistive graphene sensors are created on a single substrate and various polymer coatings applied to each individual sensor, creating a sensor output with cross-reactive response characteristics. A group of 23 polymer coatings are investigated by measuring the change in resistance among sensors, and the array response diversity evaluated using hierarchal clustering analysis and correlation analysis. We demonstrate the chemical diversity afforded by the addition of the polymer coatings, which provides not only information rich, sorption-based changes in each sensor response, but also electrical modification to the graphene, resulting in substantial enhancements in the sensing response and often a complete reversal in the resistance change direction. A variety of single volatile organic compounds and 10 Scotch whiskies were identified with 100% accuracy using only a portion of the sensing elements, suggesting that the array contains much more potential for identification of additional and more complex compounds. These results demonstrate for the first time, a cross-reactive graphene chemical sensor array, applicable to compact, low-cost, low-power, and adaptable sensing needs for electronic nose systems.

## 7.2 Introduction

An electronic nose (e-nose) is designed to mimic the human olfactory system by taking the pattern-based response of biological sensors and replacing them electronically with a chemical sensor array.<sup>55</sup> The olfactory sensory system is cross-reactive by nature, where the olfactory receptors are not highly selective toward specific analytes, and in fact, one receptor responds to many analytes and many receptors respond to any given analyte.<sup>121</sup> The pattern generated by this response and associated recognition of this pattern are critical to the operation of the overall olfactory system. Likewise, when considering an e-nose system, the sensor array should be designed in a cross-reactive manner, so that the collection of sensors contains as much chemical diversity as possible, providing an array which responds to the largest possible cross-section of analytes. In this manner, the array can adapt to new and previously unforeseen compounds and odors.

The type of sensor used in a cross-reactive array is broad and includes materials and devices such as metal oxide devices,<sup>122</sup> fluorescent organic polymers,<sup>24</sup> acoustic wave oscillators,<sup>119</sup> quantum dot composites,<sup>56</sup> colorimetric dyes,<sup>25</sup> carbon nanotubes,<sup>89</sup> and carbon black composites.<sup>123</sup> Although carbon-based materials such as carbon nanotubes and carbon black have been used in a cross-reactive format, the potential of graphene remains unrealized in this area. Recent research on single element graphene chemical sensors is promising, and capable of discrimination of multiple compounds, but the sensor will only perform to a certain extent before misclassifications occur due to similar response behavior.<sup>49,124</sup> In the case of graphene, covalent surface functionalization can provide diversity across sensor elements by modifying the graphene surface energy using

functionalization methods such as radicals, nitrenes, carbenes, arynes, and reactive plasma, to name a few.<sup>111,115,125,126</sup> Although these methods can provide the desired diversity, the process to apply multiple functionalities on a monolithic substrate for a sensor array is challenging and can cause much variation. A more reproducible and manufacturable approach to generating chemically diverse graphene sensors can be achieved by overcoating polymers directly onto array elements. Polymers can possess chromatographic properties, which aid in selectivity and separation of compounds, mixtures, and complex odors. This process is similar to the thin mucous layer found over the receptors in the human nose, which performs a degree of chromatographic separation of complex mixtures.<sup>127</sup>

Unlike carbon black, surface acoustic wave, and quartz crystal microbalance sensors, whose response is solely based on the polymer sorption properties, polymer coated graphene sensors appear to have a phenomenology containing response mechanisms due to both polymer sorption and modification of the graphene's electrical properties. The sorption based influence can be seen in the response shape during sampling and recovery, while modification of the graphene's electrical behavior is evident in the change in magnitude and direction of the resistance, sometimes causing dramatic effects. Carbon black polymer composites rely on swelling of the film, which in-turn causes the separation between carbon black particles to increase, effectively increasing the film resistance. The underlying operation of this type of sensor does not allow for a reversal in the resistance direction as seen with polymer coated graphene sensors. The temporal based information gained from polymer sorption properties, along with the change in magnitude and direction of the resistance response can be exploited for added diversity.

In this work, we demonstrate the first example of a graphene-based, cross-reactive chemical sensor array. The array is fabricated by overcoating polymers directly onto individual sensor elements contained on a monolithic substrate. The multivariate output response of the array displays phenomenology influenced by sorption properties of the polymers and modification of the electrical properties of the graphene. The array is tested against single compounds and the complex odors from scotch whiskies. The change in resistance among sensors is compared by traditional bar plots, hierarchical clustering, and correlation analysis to identify trends and relationships. The broadly responsive behavior of the sensor array suggests that multiple graphene sensors, combined with a diverse range of polymer coatings, is capable of being used as an adaptable universal electronic nose which can be used across multiple sensing disciplines.

### **7.3 Experimental Section**

#### **Sensor Array Design and Fabrication**

The sensor array consists of a 1.3 cm x 1.3 cm Si/SiO<sub>2</sub> substrate with monolayer graphene, 24-element Ti/Au interdigitated electrodes (IDE), and a final SU8 layer with openings for each individual sensor and its respective bonding pads. The Si/SiO<sub>2</sub>/Graphene substrates were cleaved into approximately 1.3 cm x 1.3 cm pieces from a larger 4" wafer (Graphenea, Cambridge, MA) by use of a diamond scribe. Conventional lift-off photolithography was then used to pattern the graphene substrate with the IDE design which consists of 24 identical devices, each comprised of 12 electrode fingers with length, width, and separation of 750 μm, 50 μm, and 50 μm, respectively, producing a total sensor area of 0.44 mm<sup>2</sup>. The patterned device was then transferred to a Temescal BJD-1800

electron beam evaporator, where a layer of Ti/Au (25nm/300nm) was deposited once an appropriate base pressure was achieved. Following metal deposition, the device was left in an acetone bath for approximately two hours to achieve metal lift-off. The metal patterned sensors were then rinsed with isopropanol and deionized water and dried with nitrogen. Once the metal deposition process was complete, a layer of SU8-2005 photoresist (MicroChem, Westborough, MA) was spun onto the device at a thickness of approximately 5  $\mu\text{m}$ . An additional photolithography mask design was used to provide an opening well to each sensor with length, width, and depth of 1300  $\mu\text{m}$ , 1200  $\mu\text{m}$ , and 5  $\mu\text{m}$ , respectively. The device was then hard baked at 150 °C for 5 minutes to further harden the SU8 layer and create a permanent structure. Lastly, the device was mounted in a 68-pin leadless ceramic chip carrier and each individual sensor wire bonded. Shown in Figure 7.1a is the photolithography mask design for the 24-element array used to create a completed device (Figure 7.1b), which contains 23 individual sensors with polymer coatings and a single uncoated sensor.

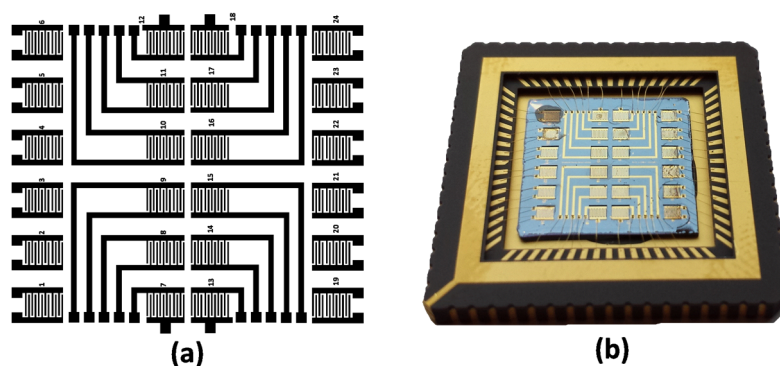


**Figure 7.1** 24-element graphene sensor array a) photolithography mask design and b) completed device, mounted and wire bonded in a leadless chip carrier with polymers applied to each sensor element.

### Polymer Coating Preparation and Application

Polymer coating solutions were created at a concentration of 20 mg/mL according to the 23 polymers and their respective solvents shown in Table 7.1. All polymers were purchased from Sigma Aldrich and used as-is or with a solvent as noted (Table 7.1). Following wire bonding, the sensor array was completed by drop casting  $\sim 0.4$   $\mu\text{L}$  of a single polymer solution into an SU8 well with a Hamilton microliter syringe, and baking the device on a hotplate at 70  $^{\circ}\text{C}$  for 5 minutes once all polymers were deposited. Each well created by the SU8 layer allows for the polymer solution to be contained to each individual sensor, and helps to prevent accidental mixing of the solutions. For the given concentration and deposition volume, approximately 8  $\mu\text{g}$  of the polymer is estimated to be left on the sensor surface after solvent evaporation.

**Table 7.1** Selected polymers and their respective solvents used as coatings to create a cross-reactive graphene sensor array.

<b>Coating</b>	<b>Abbreviation</b>	<b>Solvent</b>
Polyacenaphthylene	PACN	Chloroform
Poly(4-bromostyrene)	PBrS	Chloroform
Poly(4-tert-butylstyrene)	P4tBS	Chloroform
Poly(4-vinylphenol)	PVPh	Tetrahydrofuran
Poly(vinylbenzyl chloride)	PVBCl	Chloroform
Poly(4-vinylbiphenyl)	PVBP	Chloroform
Poly vinyl alcohol	PVA	Water
Nafion	Nafion	Used as is
Tetraethylene glycol dimethyl ether	TEGDME	Used as is
Polyethylene glycol solution	PEG	Used as is
Polystyrene	PS	Chloroform
Poly(4-vinylpyridine)	PVPy	Chloroform
Polyvinylpyrrolidone	PVPyd	Chloroform
2-Hydroxyethyl cellulose	OHcell	Water
Poly(1-hexadecene-sulfone)	P6DS	Chloroform
Poly(dimethylsiloxane-co-alkylmethylsiloxane)	PDMS-Alk	Chloroform
Poly(benzyl methacrylate)	PBMA	Chloroform
Poly(methyl methacrylate)	PMMA	Chloroform
Polycaprolactone	PCI	Chloroform
Poly(ethylene-co-vinyl acetate)	PEVA	Chloroform
Polyisobutylene	PIB	Chloroform
Poly(ethylene oxide)	PEO	Chloroform
Polyepichlorohydrin	PECH	Tetrahydrofuran

## **Instrumentation**

The bonded device was then loaded into a 68-pin breakout board outfitted with a custom machined Teflon block to provide a low volume flow channel of 0.25mL to the sensor surface. The sampling of all compounds was performed using a custom headspace sampling system where the sensor was brought to the opening of a 40mL vial containing each compound, allowing the accumulated headspace vapor to pass over the sensor at the specified flow rate. The sampling system and sensor were contained in a custom enclosure outfitted with a fume extraction system which was located in an ambient laboratory area. Each measurement was conducted under the same experimental conditions. The resistance of each sensor was measured using a data acquisition and control cube configured with two 12-channel, fully isolated resistance input boards (United Electronics Industry, Walpole, MA), creating 24 total channels with simultaneous data collection. Each channel was configured to operate in 4-wire mode, collecting resistance measurements at a rate of approximately 15 Hz. A Python script was used to read a user generated input CSV file specifying the measurement parameters for a single measurement which are: baseline time, sample time, recovery time, active channels, minimum/maximum resistance, and sample flow rate.

## **7.4 Results and Discussion**

### **Evaluation of Polymer Coating**

The selection of polymers for use in sorption based chemical sensors is commonly approached by considering the linear solvation energy relationships (LSER) of the polymer and analytes, and has been extensively modeled. The LSER model is based on a linear

combination of solvation parameters consisting of the effective hydrogen-bond acidity, hydrogen bond basicity, dipolarity/polarization parameters, and dispersion parameter.<sup>120</sup> Properly choosing combinations of polymers that cover a broad range of chemical interactions can provide the needed diversity to produce a broadly responding multivariate output. Unlike sensors which are solely dependent on the polymer sorption properties, polymer-coated graphene sensors exhibit a response which contains mechanisms due to both polymer sorption and modification of the graphene's electrical properties. While LSER parameters have proven useful in evaluating the relationships between purely sorption based sensors and analytes of interest, the modification of electronic properties of the graphene in the present study make the interaction significantly more complex. For this reason, the use of LSER parameters is not directly applicable to the coated graphene sensors. Additional statistical techniques such as hierarchical clustering analysis (HCA) and correlation analysis can be used to determine linear dependence among sensor channels, and aid in determining relationships among the effects each polymer has on the measured output response.

### **Cross-Reactive Array Response: Single Compounds**

The cross-reactive responsivity of the sensor array was first tested by exposing the array to singular compounds covering a wide variety of chemical families consisting of ethanol, methanol (MeOH), acetone, cyclohexanone, tetrahydrofuran (THF), diethyl ether, formaldehyde, 2-nitrotoluene (2NT), 4-chlorotoluene, toluene, hexane, chloroform, acetonitrile (ACN), and dimethyl sulfoxide (DMSO). The sensor array was comprised of 24 individual sensors, where 23 sensors were coated with the polymers described in Table 1 and the remaining sensor was left uncoated to serve as a control. For each measurement the

baseline, sample, and recovery periods were set to 60 s, 30 s, and 60 s, respectively, with a flow rate of 20 mL/min. The resistance of each channel was measured simultaneously at a continuous rate of approximately 15 Hz. The maximum change in resistance ( $\Delta R$ ) was extracted from each sensor response and is summarized in Figure 7.2a. For the purpose of illustrating the diverse output response, while displaying a manageable amount of information, the bar plot in Figure 7.2a contains response data for acetone, THF, MeOH, and ACN. Additional response data for all other compounds can be found in the Supporting Information. Figure 7.2a consolidates the  $\Delta R$  values for the 24 sensors while exposed to acetone, THF, MeOH, and ACN, with a color coding legend to indicate the respective polymer coating. Excellent diversity across the sensor array is observed for all compounds, even when only considering the extracted  $\Delta R$  feature and disregarding temporal information due to sorption kinetics captured by features such as response and recovery areas, and fitting coefficients. Figure 7.2b and Figure 7.2c are time-series plots of the change in resistance with time in seconds and  $\Delta R$  in percent as the x-axis and y-axis, respectively. Figure 7.2b shows the response pattern to ACN for sensors coated with PVPh, PVPyd, PCI, PEG, and PVBP, along with an uncoated sensor. Similarly, Figure 7.2c shows the response pattern to MeOH for sensors coated with TEGDME, PDMS-Alkm, PVPyd, PCI, PEG, and an uncoated sensor. These plots demonstrate the diversity that is observed not only in the magnitude and direction of the sensor array response, but also in the shapes of the response curves which contain important kinetic information.

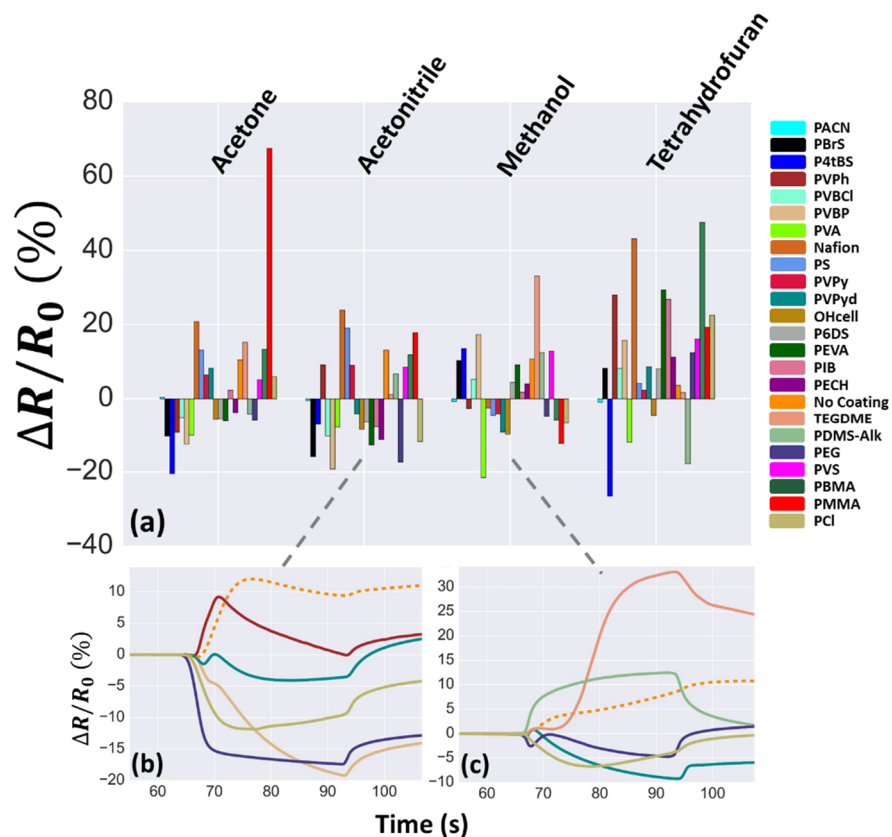


**Figure 7.2** a) Cross-reactive response behavior of the graphene sensor array with 23 different polymer coatings, comparing the maximum change in resistance upon exposure to acetone, acetonitrile, methanol, and tetrahydrofuran. Time-series plots of maximum change in resistance for coatings b) PVPh, PVPyd, PCI, PEG, and PVBP while exposed to acetonitrile and c) TEGDME, PDMS, PVPYd, PCI, and PEG while exposed to methanol.

Changes from the measured  $\Delta R$  for the uncoated sensor displayed dramatic changes (both increases and decreases) in sensitivity, often resulting in a complete reversal in the resistance signal. Table 7.2 summarized the most significant changes when compared to the uncoated sensor response for each compound.

**Table 7.2** Comparison of uncoated and coated sensor responses for a specific coating which produced a notable change for each single compound.

<b>Compound</b>	<b>Coating</b>	<b>Uncoated <math>\Delta R</math> (%)</b>	<b>Coated <math>\Delta R</math> (%)</b>
2-Nitrotoluene	Nafion	-0.6	-6.4
4-Chlorotoluene	Nafion	-1.0	-11
Acetone	PMMA	-11	68
Acetonitrile	PVBP	13	-19
Chloroform	PDMS-Alk	-19	33
Cyclohexanone	PECH	1.8	9.8
Diethyl Ether	PDMS-Alk	3.6	-9.5
Dimethyl Sulfoxide	PDMS-Alk	1.9	-18
Ethanol	OHcell	-0.1	-2.4
Formaldehyde	Nafion	2.7	34
Hexane	OHcell	1	-8.9
Methanol	PVA	11	-22
Tetrahydrofuan	P4tBS	3.6	-27
Toluene	PECH	-1.4	-4.2

A combination of HCA and correlation heat maps was used to determine the relationships among polymer-coated sensor channels.  $\Delta R$  of each channel was chosen as the metric to produce a visually comprehensible comparison of sensor performance. HCA was performed using squared Euclidean distance as the dissimilarity metric and a complete linkage criterion. A correlation matrix was calculated from the same  $\Delta R$  feature vector used for HCA and was visually represented by a heat map. The correlation matrix contains values which range from -1 to +1, with values closer to +1 signifying a strong positive correlation and values closer to -1 signifying a strong negative correlation. Shown in Figure 7.3 is a correlation heatmap and HCA plot for all compound/polymer combinations, where the maximum change in resistance was extracted from each sensor response. Figure 7.3a

represents the Pearson product-moment correlation coefficients calculated between each sensor's  $\Delta R$ , which is used to describe the linear correlation between each sensor output. The colorbar ranges from -1.0 to +1.0, corresponding to colors blue and red, respectively. Shown to the left of the colorbar in Figure 7.3a is an average Pearson correlation value calculated for each coating. This value gives an overall correlation for each coating compared against all other coatings being evaluated. An uncoated sensor labeled "No Coating" is included as a control to compare selectivity and sensitivity changes. The sensor with no coating is uncorrelated with many of the other coated sensors such as PDMS-AIk, PVA, P4tBS, TEGDME, OHcell, PEG, PVBP, PBrS, and PACN, mainly due to either large changes in the  $\Delta R$  or reversal in  $\Delta R$  value. On the other hand, the uncoated sensor is most correlated with PVS, PS, PVPy, and PVPyD, which also agrees with the HCA grouping. Figure 7.3b displays a dendrogram for HCA performed on the same data array and is used to visualize how coatings group together based on a specified response feature. In Figure 7.3b, the x-axis and y-axis represent the polymer coatings and relative calculated dissimilarity, respectively. The level of dissimilarity is calculated by taking the squared Euclidean distance between the  $\Delta R$  value found for each coating, while considering the entire compound set. The two-component groups which display the most similarity are P6DS/PVBCI, PVPy/PS, PVS/No Coating, PIB/PEVA, PVBP/PBrS, and PCI/PEG. On the other hand, groups that display the least similarity are PDMS-AIk/TEGDME, PBMA/PVPh, and PMMA/Nafion. Examples of this dissimilarity can further be seen in Figure 7.4 for coatings PECH and PDMS-AIk, which are from two very different portions of the dendrogram (plots of this type for every coating can be found in the Supporting Information). The time-series

plots show the response of each sensor with its respective coating to the same set of compounds.

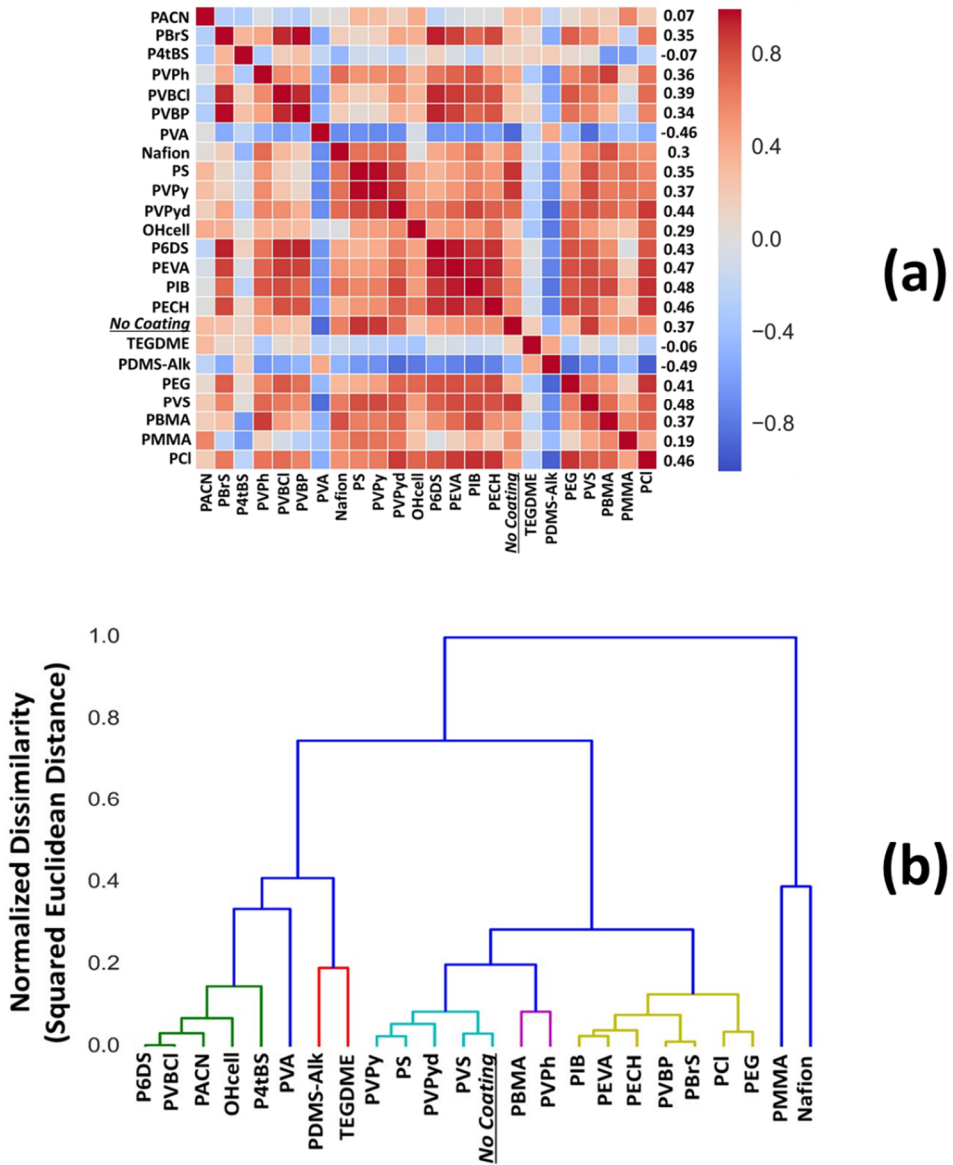


**Figure 7.3** Analysis of graphene sensor array with a) a correlation heatmap and b) hierarchical cluster analysis dendrogram.

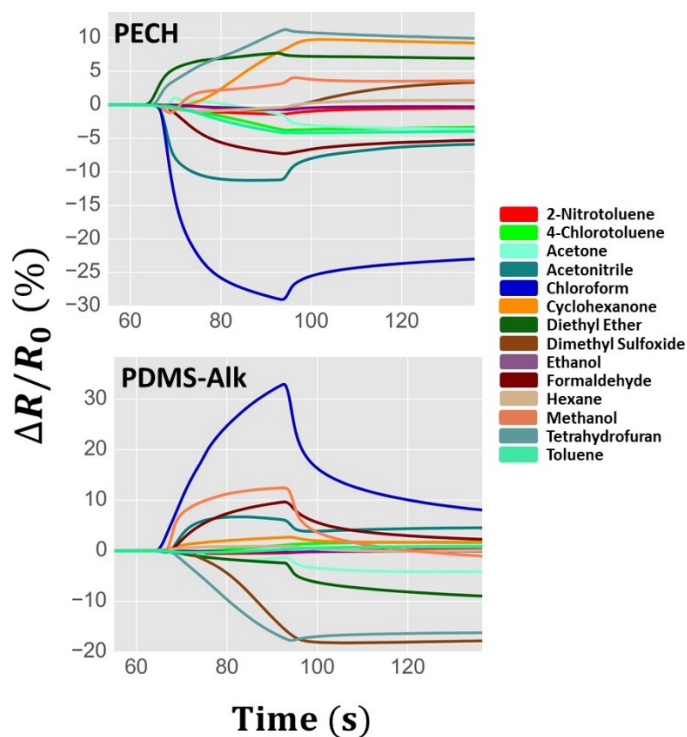


**Figure 7.4** Time-series plots of PECH and PDMS-Alk coated sensors demonstrating the variations that can be seen for sensors with different polymer coatings.

In our previous work we tested a single graphene sensor without modification or coating against 2NT, 4-chlorotoluene, acetic acid, acetone, chloroform, cyclohexanone, diethyl ether, DMSO, hexane, THF, and toluene, where a classification accuracy of 96% was achieved for 20 measurements of each compound.<sup>124</sup> Although this uncoated sensor produced a diverse range of outputs, we believe that the limits of its capability were approached. Using the same testing conditions, measurement repetitions, response feature types, and classification algorithm, we were able to achieve 100% classification by using only a single graphene sensor with a Nafion coating. When considering two coated sensors,

100% classification was achieved with a Nafion coating along with either P4tBS, PVBCI, PVPy, PVPh, or OHcell for the same set of compounds.

### **Cross-Reactive Array Response: Complex Odors**

The sensor array was tested against the complex volatile mixture contained in the headspace of various Scotch whiskies. Scotch has very unique and distinguishable smells, with many compounds found in its headspace odor such as higher alcohols, ethyl and isoamyl esters, acetates, fatty acids, ketones, monoterpenes, and phenols.<sup>128</sup> An uncoated graphene sensor displayed little or no diversity when exposed to ethanol and the following Scotch whiskies: Gordon & Mcphail, Jura, Macallan, Dewar's, Kilchoman, Laphroig, Exclousive Malts, Johnnie Walker Blue (JW Blue), Johnnie Walker Black (JW Black), and Johnnie Walker Spice Road (JW Spice Road), as shown in Figure 7.5a. While not all previously described polymers were evaluated against this set of Scotch whiskies, a few were identified as potentially discriminating coatings and are provided here. Sensors coated with Nafion, OHcell, and PBrS are shown in Figure 7.5b, 5c, and 5d, respectively, with each displaying a degree of diversity. The Nafion coating produced a reversal in signal direction for ethanol and each Scotch, and also a substantial increase in magnitude. The OHcell coating shown in Figure 7.5c exhibits the capability to isolate ethanol from the Scotch "smell," which indicates that the response seen for the Scotch samples are caused by compounds other than ethanol. To test the discrimination ability of the sensor array towards these complex odors, 15 measurements were taken for ethanol and each Scotch whiskey, which were then supplied to a feedforward neural network. A classification

accuracy of 100% was achieved using OHcell, Ncell, PACN, and PBrS sensor coatings (refer to Supporting Information for further classification details).

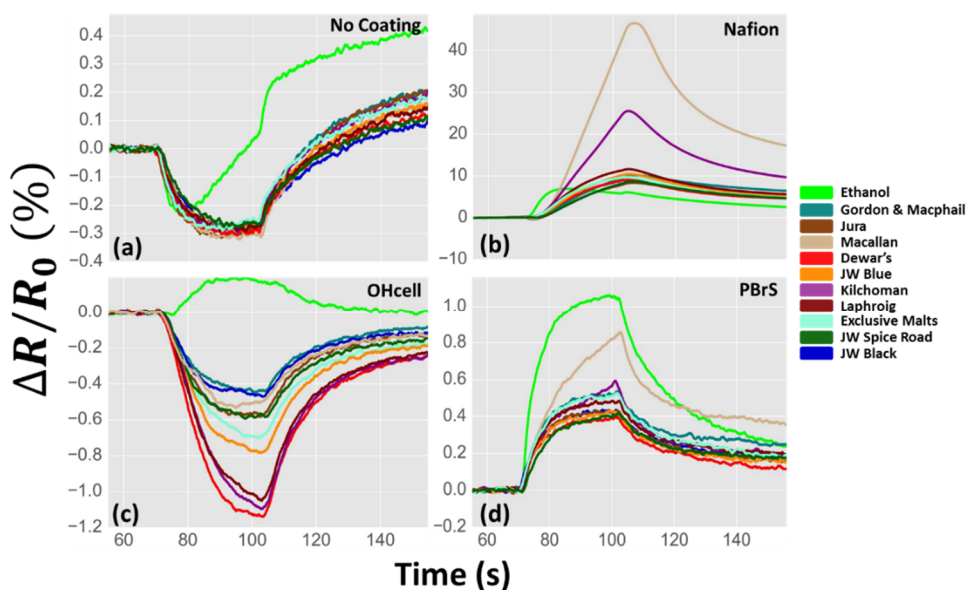


**Figure 7.5** Graphene sensor response to the headspace of various Scotch whiskies for an a) uncoated sensor and sensors coated with b) Nafion, c) 2-Hydroxyethyl cellulose, and d) Poly(4-tert-butylstyrene).

## 7.5 Conclusions

A cross-reactive chemical sensor array, based on polymer coated resistive graphene sensors, was fabricated then tested and characterized against a variety of single compounds and complex odors. The most remarkable attribute of the sensor array is the diverse output response, which is not only influenced by the sorption properties of the polymer, but also by

electronic interactions between the polymer and graphene. This dual-phenomenology is fundamentally different compared to other similar widely used sensor arrays such as carbon black, which rely solely on swelling of the polymer to cause an increase in the sensor resistance. To our knowledge, this is first reported case of using graphene in a cross-reactive array and may open the door to additional research to further develop graphene into a viable electronic nose material.

## 7.6 Supporting Information

For the purpose of displaying the collected data in a way to demonstrate the diversity of the graphene sensor array, only a portion of the tested analytes were previously presented. The entire analyzed dataset is presented here. Figure 7.6 is a bar plot consolidating the maximum change in resistance ( $\Delta R$ ) for each sensor channel while exposed to all compounds: ethanol, methanol (MeOH), acetone, cyclohexanone, tetrahydrofuran (THF), diethyl ether, formaldehyde, 2-nitrotoluene (2NT), 4-chlorotoluene, toluene, hexane, chloroform, acetonitrile (ACN), and dimethyl sulfoxide (DMSO). Ethanol, 2NT, 4-chlorotoluene, and toluene show the least diversity in terms of coatings which produce a reversal in the response direction, but still provide adequate diversity when considering the magnitude and shape of each respective response.

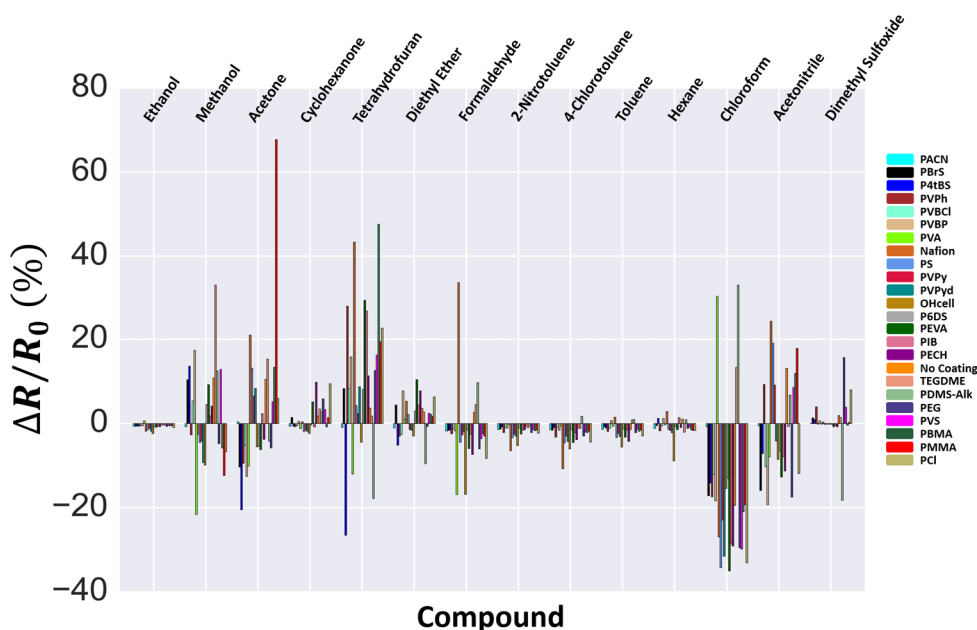


**Figure 7.6** Cross-reactive behavior of the graphene sensor array, with 23 different polymer coatings, comparing the maximum change in resistance response pattern towards ethanol, methanol, acetone, cyclohexanone, tetrahydrofuran, diethyl ether, formaldehyde, 2-nitrotoluene, 4-chlorotoluene, toluene, hexane, chloroform, acetonitrile, and dimethyl sulfoxide.

The values extracted from each polymer coated sensor, including an uncoated sensor, used to create the plot in Figure 7.6 are shown in a heat map table in Figure 7.7. The x-axis and y-axis display the polymer coating labels and tested compound, respectively. A  $\Delta R$  value for every combination between coating and compound is shown in numerical format, and also with a corresponding color which is weighted according to the provided colorbar. A positive  $\Delta R$  is shown in red with a maximum of 68%, and a negative  $\Delta R$  is shown in blue with a maximum of 35%. Time-series plots for all 24 sensors can be seen in Figure 7.8. Each plots contains that particular sensor's response to 2NT, 4-chlorotoluene,

acetone, CAN, chloroform, cyclohexanone, diethyl ether, DMSO, ethanol, formaldehyde, hexane, methanol, THF, and toluene.

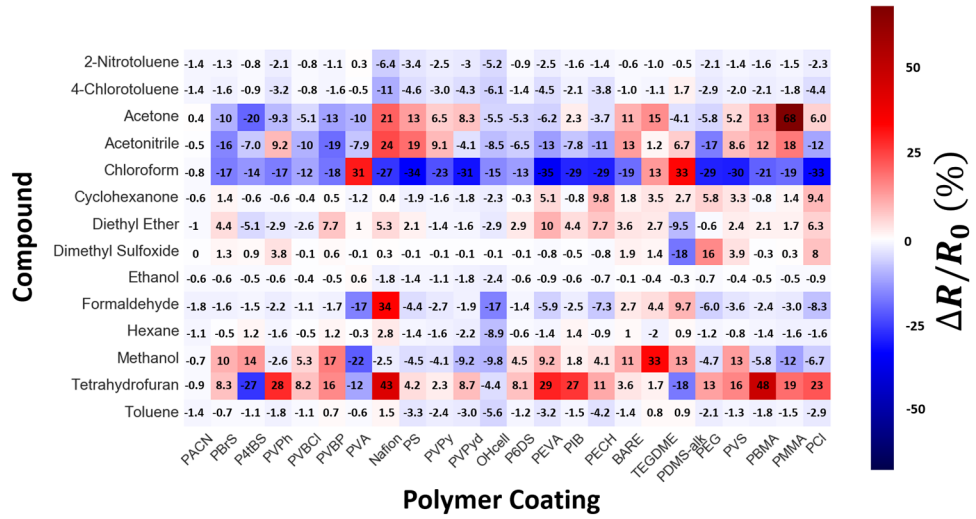


**Figure 7.7** Array maximum change in resistance response values shown with actual value and also represented by color mapping, with red indicating an increase in resistance and blue indicating a decrease in resistance.

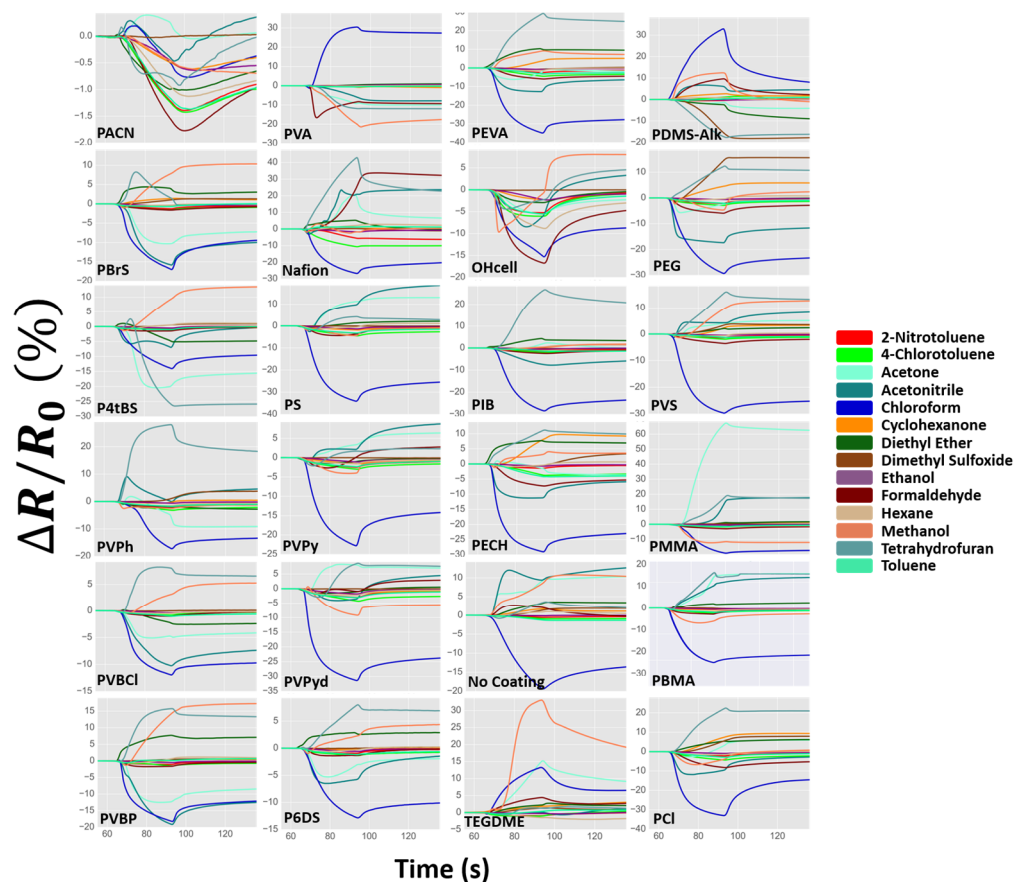


**Figure 7.8** Times-series change in resistance for each sensor type towards 2-Nitrotoluene, 4-Chlorotoluene, Acetone, Acetonitrile, Chloroform, Cyclohexanone, Diethyl Ether, Dimethyl Sulfoxide, Ethanol, Formaldehyde, Hexane, Methanol, Tetrahydrofuran, and Toluene.

The measured resistance values for each sensor output were sub-sampled by taking 50 equally spaced points from each output to compile a 165 x 200 feature vector, with 165 observations and 200 features. The feature vector was then scaled to zero mean and unit variance (autoscale). Linear discrimination analysis (LDA) was then used to reduce the dimension of the feature space to 9 features, which are linear combinations of all original

features. The plotted LDA transformation can be seen in Figure 7.9 showing excellent class separation. The LDA transformed feature vector was then supplied to a multilayer perceptron feedforward neural network using 10-fold cross-validation and a training percentage of 70%, which was able to achieve a classification of 100%.

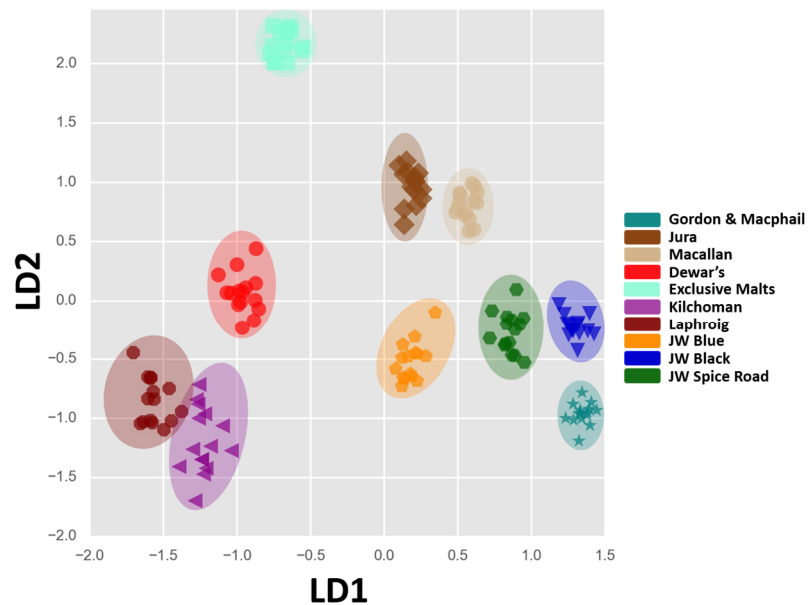


**Figure 7.9** Linear discrimination transform of Scotch whisky data displaying excellent class separation.

## Chapter 8 Future Graphene-Based Sensing Work

Graphene has been shown to have astonishing properties and great potential for use in applications which span many fields. Graphene-based chemical or biological sensors are the most promising applications of graphene. This is because graphene has less constrictive constraint and is more competitive in the area of sensors in comparison with semiconductor devices which are dominant in CMOS technology. These are many different paths in research and development to integrate graphene in new, innovative sensing designs.

For example, microfluidic based sensor designs are important for biological sensing applications where the sample to be analyzed is in a liquid form (e.g., saliva, blood, urine). In this case, graphene can be modified with DNA, peptides, and other biological functionalities in order to target specific diagnosis needs. Basic resistive based graphene sensors could be designed on the micro or nano-level and placed directly in the fluidic flow path in an array format.

Raman spectroscopy is a powerful tool for characterization and investigation of the graphene's surface. Currently the major application is to characterize growth quality and extent of surface functionalization. In the case where surface modification is done in liquid, it may be possible to directly monitor the reaction at the graphene surface as it happens with a Raman microscope. By selecting the correct magnification, confocal depth, and subtracting background from the modification solution, a time-series spectra of the modification process may be captured. In addition, Raman spectroscopy also has the potential to gain insight to how gaseous chemical compounds temporarily modify the graphene surface, which would provide further details to the mechanisms involved during

chemical sensing. Designing a flow cell with an optical window which can be positioned under a Raman microscope could allow in-situ measurements of the graphene surface while being exposed to chemical vapor. Comparing and aligning these results with the simultaneous resistive based response measurement could provide further details of the response mechanism between graphene and chemical compounds.

The research presented in this work will be extended by continuing and expanding on the concepts from Chapter 7. The study of polymer-coated graphene sensors indicates that it is quite possible to create a broadly responsive sensor array by applying multiple polymer coatings directly on graphene sensors. The results from this were very compelling, but more research needs to be done to better understand the effect of the polymer. Characterization of the polymers used in this research and others will be important to identify a set of polymers that provide increased selectivity and increased sensitivity. Additionally, the selected polymers can be used in a different configuration with a graphene derivative. Graphene nanoplatelets can be combined with a polymer to make a conductive graphene nanoplatelet-polymer composite, similar to carbon black-polymer composite. The graphene nanoplatelets can provide additional unique properties to the polymer and would allow for an easy to manufacture and inexpensive sensor array. The concept of using graphene as a chemical sensor will also be extended to the biological world by functionalizing the graphene surface with nanoparticles, peptides, and other biological functionalizations. The same device structure and processing concepts will be applied and adapted from previous lessons learned to quickly adapt to sensing biological analytes.

## References

- (1) Axel, R. The Molecular Logic of Smell. *Sci. Am.* **1995**.
- (2) Bushdid, C.; Magnasco, M. O.; Vosshall, L. B.; Keller, A. Humans Can Discriminate More than 1 Trillion Olfactory Stimuli. *Science* **2014**, *343*, 1370–1372.
- (3) Craven, B. A.; Paterson, E. G.; Settles, G. S. The Fluid Dynamics of Canine Olfaction: Unique Nasal Airflow Patterns as an Explanation of Macrosmia. *J. R. Soc. Interface* **2010**, *7*, 933–943.
- (4) Pearce, T. C. *Handbook of Machine Olfaction Electronic Nose Technology*; Wiley-VCH: Weinheim [Germany], 2003.
- (5) Patel, H. K. *The Electronic Nose: Artificial Olfaction Technology*, Biological and Medical Physics, Biomedical Engineering; Springer India: New Delhi, 2014.
- (6) Most Popular Coding Languages of 2015. *Most Popular Coding Languages of 2015*.
- (7) Jones, E.; Oliphant, T.; Peterson, P.; others. *SciPy: Open Source Scientific Tools for Python*; 2001.
- (8) Van Der Walt, S.; Colbert, S. C.; Varoquaux, G. The NumPy Array: A Structure for Efficient Numerical Computation. *Comput. Sci. Eng.* **2011**, *13*, 22–30.
- (9) McKinney, W. Data Structures for Statistical Computing in Python. In *Proceedings of the 9th Python in Science Conference*; 2010; Vol. 445, pp. 51–56.
- (10) Pedregosa, F.; Varoquaux, G.; Gramfort, A.; Michel, V.; Thirion, B.; Grisel, O.; Blondel, M.; Prettenhofer, P.; Weiss, R.; Dubourg, V.; *et al.* Scikit-Learn: Machine Learning in Python. *J. Mach. Learn. Res.* **2011**, *12*, 2825–2830.
- (11) Hauck, T. *Scikit-Learn Cookbook: Over 50 Recipes to Incorporate Scikit-Learn into Every Step of the Data Science Pipeline, from Feature Extraction to Model Building and Model Evaluation*; Packt Publishing: Birmingham, U.K., 2014.
- (12) Hunter, J. D. Matplotlib: A 2D Graphics Environment. *Comput. Sci. Eng.* **2007**, *9*, 90–95.
- (13) Richert, W.; Coelho, L. P. *Building Machine Learning Systems with Python*; Packt Publishing: Birmingham, 2013.
- (14) Kuhn, M.; Johnson, K. *Applied Predictive Modeling*; Springer: New York, NY, 2013.
- (15) Dougherty, G. *Pattern Recognition and Classification an Introduction*; Springer New York : Imprint : Springer: New York, NY, 2013.
- (16) Wang, B.; Cancilla, J. C.; Torrecilla, J. S.; Haick, H. Artificial Sensing Intelligence with Silicon Nanowires for Ultrasensitive Detection in the Gas Phase. *Nano Lett.* **2014**, *14*, 933–938.

- (17) Kybert, N. J.; Lerner, M. B.; Yodh, J. S.; Preti, G.; Johnson, A. T. C. Differentiation of Complex Vapor Mixtures Using Versatile DNA–Carbon Nanotube Chemical Sensor Arrays. *ACS Nano* **2013**, *7*, 2800–2807.
- (18) Lewis, N. S. Comparisons between Mammalian and Artificial Olfaction Based on Arrays of Carbon Black–Polymer Composite Vapor Detectors. *Acc. Chem. Res.* **2004**, *37*, 663–672.
- (19) Fine, G. F.; Cavanagh, L. M.; Afonja, A.; Binions, R. Metal Oxide Semi-Conductor Gas Sensors in Environmental Monitoring. *Sensors* **2010**, *10*, 5469–5502.
- (20) Berna, A. Metal Oxide Sensors for Electronic Noses and Their Application to Food Analysis. *Sensors* **2010**, *10*, 3882–3910.
- (21) Sunil, K.; Yadava, R. D. S. Data Mining Approach to Polymer Selection for Making SAW Sensor Array Based Electronic Nose. *Sens. Transducers* **2012**, 108.
- (22) Ying, Z.; Jiang, Y.; Du, X.; Xie, G.; Yu, J.; Tai, H. Polymer Coated Sensor Array Based on Quartz Crystal Microbalance for Chemical Agent Analysis. *Eur. Polym. J.* **2008**, *44*, 1157–1164.
- (23) Lang, H. P.; Ramseyer, J. P.; Grange, W.; Braun, T.; Schmid, D.; Hunziker, P.; Jung, C.; Hegner, M.; Gerber, C. An Artificial Nose Based on Microcantilever Array Sensors. *J. Phys. Conf. Ser.* **2007**, *61*, 663–667.
- (24) Woodka, M. D.; Schnee, V. P.; Polcha, M. P. Fluorescent Polymer Sensor Array for Detection and Discrimination of Explosives in Water. *Anal. Chem.* **2010**, *82*, 9917–9924.
- (25) Janzen, M. C.; Ponder, J. B.; Bailey, D. P.; Ingison, C. K.; Suslick, K. S. Colorimetric Sensor Arrays for Volatile Organic Compounds. *Anal. Chem.* **2006**, *78*, 3591–3600.
- (26) Zhang, C.; Suslick, K. S. Colorimetric Sensor Array for Soft Drink Analysis. *J. Agric. Food Chem.* **2007**, *55*, 237–242.
- (27) Lipatov, A.; Varezchnikov, A.; Wilson, P.; Sysoev, V.; Kolmakov, A.; Sinitskii, A. Highly Selective Gas Sensor Arrays Based on Thermally Reduced Graphene Oxide. *Nanoscale* **2013**, *5*, 5426.
- (28) Schedin, F.; Geim, A. K.; Morozov, S. V.; Hill, E. W.; Blake, P.; Katsnelson, M. I.; Novoselov, K. S. Detection of Individual Gas Molecules Adsorbed on Graphene. *Nat. Mater.* **2007**, *6*, 652–655.
- (29) Lu, Y.; Goldsmith, B. R.; Kybert, N. J.; Johnson, A. T. C. DNA-Decorated Graphene Chemical Sensors. *Appl. Phys. Lett.* **2010**, *97*, 083107.
- (30) Kybert, N. J.; Han, G. H.; Lerner, M. B.; Dattoli, E. N.; Esfandiari, A.; Charlie Johnson, A. T. Scalable Arrays of Chemical Vapor Sensors Based on DNA-Decorated Graphene. *Nano Res.* **2014**, *7*, 95–103.
- (31) Kleffmann, J.; Tapia, G. V.; Bejan, I.; Kurtenbach, R.; Wiesen, P. NO<sub>2</sub> Measurement Techniques: Pitfalls and New Developments. In *Disposal of Dangerous Chemicals in Urban Areas and Mega Cities*; Barnes, I.; Rudziński, K. J., Eds.; Springer Netherlands: Dordrecht, 2013; pp. 15–28.
- (32) Chung, M. G.; Kim, D. H.; Lee, H. M.; Kim, T.; Choi, J. H.; Seo, D. kyun; Yoo, J.-B.; Hong, S.-H.; Kang, T. J.; Kim, Y. H. Highly Sensitive NO<sub>2</sub> Gas Sensor Based on Ozone Treated Graphene. *Sens. Actuators B Chem.* **2012**, *166-167*, 172–176.

- (33) Novikov, S.; Lebedeva, N.; Satrapinski, A. Ultrasensitive NO<sub>2</sub> Gas Sensor Based on Epitaxial Graphene. *J. Sens.* **2015**, *2015*, 1–7.
- (34) Rumyantsev, S.; Liu, G.; Shur, M. S.; Potyrailo, R. A.; Balandin, A. A. Selective Gas Sensing with a Single Pristine Graphene Transistor. *Nano Lett.* **2012**, *12*, 2294–2298.
- (35) Novoselov, K. S.; Geim, A. K.; Morozov, S. V.; Jiang, D.; Zhang, Y.; Dubonos, S. V.; and Grigorieva, I. V.; Firsov, A. A. Electric Field Effect in Atomically Thin Carbon Films. *science* **2004**, *306*, 666–669.
- (36) Nixon, A. *Graphene Electron Cloud*; 2016.
- (37) Kauffman, D. R.; Star, A. Carbon Nanotube Gas and Vapor Sensors. *Angew. Chem. Int. Ed.* **2008**, *47*, 6550–6570.
- (38) Yavari, F.; Koratkar, N. Graphene-Based Chemical Sensors. *J. Phys. Chem. Lett.* **2012**, *3*, 1746–1753.
- (39) Quiroga, M. A.; Cabeza, G. F. Role of Van Der Waals Forces in Graphene Adsorption over Pd, Pt, and Ni. *Braz. J. Phys.* **2013**, *43*, 126–129.
- (40) Group for Physics of Ordered Nanostructures and New Materials in Photonic. *Graphene Exfoliation*.
- (41) Warner, J. H.; Schaffel, F.; Rummeli, M.; Bachmatiuk, A. *Graphene: Fundamentals and Emergent Applications*; First edition.; Elsevier: Amsterdam, 2013.
- (42) Li, P.; Chen, C.; Zhang, J.; Li, S.; Sun, B.; Bao, Q. Graphene-Based Transparent Electrodes for Hybrid Solar Cells. *Front. Mater.* **2014**, *1*.
- (43) Dreyer, D. R.; Park, S.; Bielawski, C. W.; Ruoff, R. S. The Chemistry of Graphene Oxide. *Chem Soc Rev* **2010**, *39*, 228–240.
- (44) Bae, S.; Kim, H.; Lee, Y.; Xu, X.; Park, J.-S.; Zheng, Y.; Balakrishnan, J.; Lei, T.; Ri Kim, H.; Song, Y. I.; *et al.* Roll-to-Roll Production of 30-Inch Graphene Films for Transparent Electrodes. *Nat. Nanotechnol.* **2010**, *5*, 574–578.
- (45) Lipatov, A.; Varezchnikov, A.; Augustin, M.; Bruns, M.; Sommer, M.; Sysoev, V.; Kolmakov, A.; Sinitskii, A. Intrinsic Device-to-Device Variation in Graphene Field-Effect Transistors on a Si/SiO<sub>2</sub> Substrate as a Platform for Discriminative Gas Sensing. *Appl. Phys. Lett.* **2014**, *104*, 013114.
- (46) Wang, Q. H.; Jin, Z.; Kim, K. K.; Hilmer, A. J.; Paulus, G. L. C.; Shih, C.-J.; Ham, M.-H.; Sanchez-Yamagishi, J. D.; Watanabe, K.; Taniguchi, T.; *et al.* Understanding and Controlling the Substrate Effect on Graphene Electron-Transfer Chemistry via Reactivity Imprint Lithography. *Nat. Chem.* **2012**, *4*, 724–732.
- (47) Kumar, B.; Min, K.; Bashirzadeh, M.; Farimani, A. B.; Bae, M.-H.; Estrada, D.; Kim, Y. D.; Yasaei, P.; Park, Y. D.; Pop, E.; *et al.* The Role of External Defects in Chemical Sensing of Graphene Field-Effect Transistors. *Nano Lett.* **2013**, *13*, 1962–1968.
- (48) Balandin, A. A. Low-Frequency 1/f Noise in Graphene Devices. *Nat. Nanotechnol.* **2013**, *8*, 549–555.
- (49) Rumyantsev, S.; Liu, G.; Shur, M. S.; Potyrailo, R. A.; Balandin, A. A. Selective Gas Sensing with a Single Pristine Graphene Transistor. *Nano Lett.* **2012**, *12*, 2294–2298.

- (50) Lin, Y.-C.; Lu, C.-C.; Yeh, C.-H.; Jin, C.; Suenaga, K.; Chiu, P.-W. Graphene Annealing: How Clean Can It Be? *Nano Lett.* **2012**, *12*, 414–419.
- (51) Cheng, Z.; Zhou, Q.; Wang, C.; Li, Q.; Wang, C.; Fang, Y. Toward Intrinsic Graphene Surfaces: A Systematic Study on Thermal Annealing and Wet-Chemical Treatment of SiO<sub>2</sub>-Supported Graphene Devices. *Nano Lett.* **2011**, *11*, 767–771.
- (52) Eckmann, A.; Felten, A.; Mishchenko, A.; Britnell, L.; Krupke, R.; Novoselov, K. S.; Casiraghi, C. Probing the Nature of Defects in Graphene by Raman Spectroscopy. *Nano Lett.* **2012**, *12*, 3925–3930.
- (53) Wall, M. The Raman Spectroscopy of Graphene and the Determination of Layer Thickness. *Thermo Fish. Sci. Appl. Note* **2011**, 52252.
- (54) Di Carlo, S.; Falasconi, M.; Sánchez, E.; Scionti, A.; Squillero, G.; Tonda, A. Increasing Pattern Recognition Accuracy for Chemical Sensing by Evolutionary Based Drift Compensation. *Pattern Recognit. Lett.* **2011**, *32*, 1594–1603.
- (55) Che Harun, F. K.; Covington, J. A.; Gardner, J. W. Mimicking the Biological Olfactory System: A Portable Electronic Mucosa. *IET Nanobiotechnol.* **2012**, *6*, 45.
- (56) Bright, C. J.; Nallon, E. C.; Polcha, M. P.; Schnee, V. P. Quantum Dot and Polymer Composite Cross-Reactive Array for Chemical Vapor Detection. *Anal. Chem.* **2015**, *87*, 12270–12275.
- (57) Mallya, A. N.; Kottokaran, R.; Ramamurthy, P. C. Conducting Polymer–carbon Black Nanocomposite Sensor for Volatile Organic Compounds and Correlating Sensor Response by Molecular Dynamics. *Sens. Actuators B Chem.* **2014**, *201*, 308–320.
- (58) García-Berrios, E.; Theriot, J. C.; Woodka, M. D.; Lewis, N. S. Detection of Ammonia, 2,4,6-Trinitrotoluene, and Common Organic Vapors Using Thin-Film Carbon Black-Metalloporphyrin Composite Chemiresistors. *Sens. Actuators B Chem.* **2013**, *188*, 761–767.
- (59) Sisk, B. C.; Lewis, N. S. Vapor Sensing Using Polymer/Carbon Black Composites in the Percolative Conduction Regime. *Langmuir* **2006**, *22*, 7928–7935.
- (60) Paczosa-Bator, B.; Cabaj, L.; Piech, R.; Skupień, K. Potentiometric Sensors with Carbon Black Supporting Platinum Nanoparticles. *Anal. Chem.* **2013**, *85*, 10255–10261.
- (61) Zhang, B.; Fu, R.; Zhang, M.; Dong, X.; Wang, L.; Pittman, C. U. Gas Sensitive Vapor Grown Carbon Nanofiber/polystyrene Sensors. *Mater. Res. Bull.* **2006**, *41*, 553–562.
- (62) Mao, X.; Yang, X.; Rutledge, G. C.; Alan Hatton, T. Ultra-Wide-Range Electrochemical Sensing Using Continuous Electrospun Carbon Nanofibers with High Densities of States. *ACS Appl. Mater. Interfaces* **2014**, *6*, 3394–3405.
- (63) Lee, J. S.; Kwon, O. S.; Park, S. J.; Park, E. Y.; You, S. A.; Yoon, H.; Jang, J. Fabrication of Ultrafine Metal-Oxide-Decorated Carbon Nanofibers for DMMP Sensor Application. *ACS Nano* **2011**, *5*, 7992–8001.
- (64) Wang, F.; Gu, H.; Swager, T. M. Carbon Nanotube/Polythiophene Chemiresistive Sensors for Chemical Warfare Agents. *J. Am. Chem. Soc.* **2008**, *130*, 5392–5393.
- (65) Robinson, J. A.; Snow, E. S.; Bădescu, Ș. C.; Reinecke, T. L.; Perkins, F. K. Role of Defects in Single-Walled Carbon Nanotube Chemical Sensors. *Nano Lett.* **2006**, *6*, 1747–1751.

- (66) Parikh, K.; Cattanach, K.; Rao, R.; Suh, D.-S.; Wu, A.; Manohar, S. K. Flexible Vapour Sensors Using Single Walled Carbon Nanotubes. *Sens. Actuators B Chem.* **2006**, *113*, 55–63.
- (67) Goldsmith, B. R.; Mitala, J. J.; Josue, J.; Castro, A.; Lerner, M. B.; Bayburt, T. H.; Khamis, S. M.; Jones, R. A.; Brand, J. G.; Sliigar, S. G.; *et al.* Biomimetic Chemical Sensors Using Nanoelectronic Readout of Olfactory Receptor Proteins. *ACS Nano* **2011**, *5*, 5408–5416.
- (68) Kawano, T.; Chiamori, H. C.; Suter, M.; Zhou, Q.; Sosnowchik, B. D.; Lin, L. An Electrothermal Carbon Nanotube Gas Sensor. *Nano Lett.* **2007**, *7*, 3686–3690.
- (69) Nagareddy, V. K.; Chan, H. K.; Hernández, S. C.; Wheeler, V. D.; Myers-Ward, R. L.; Nyakiti, L. O.; Eddy, C. R.; Walton, S. G.; Goss, J. P.; Wright, N. G.; *et al.* Detection of Polar Chemical Vapors Using Epitaxial Graphene Grown on SiC (0001). *Appl. Phys. Lett.* **2013**, *102*, 173103.
- (70) Dan, Y.; Lu, Y.; Kybert, N. J.; Luo, Z.; Johnson, A. T. C. Intrinsic Response of Graphene Vapor Sensors. *Nano Lett.* **2009**, *9*, 1472–1475.
- (71) Omidvar, A.; Mohajeri, A. Edge-Functionalized Graphene Nanoflakes as Selective Gas Sensors. *Sens. Actuators B Chem.* **2014**, *202*, 622–630.
- (72) Fowler, J. D.; Allen, M. J.; Tung, V. C.; Yang, Y.; Kaner, R. B.; Weiller, B. H. Practical Chemical Sensors from Chemically Derived Graphene. *ACS Nano* **2009**, *3*, 301–306.
- (73) Sekhar, P. K.; Brosha, E. L.; Mukundan, R.; Garzon, F. H. Chemical Sensors for Environmental Monitoring and Homeland Security. *Electrochem. Soc. Interface* **2010**, *19*, 35.
- (74) Black, D. R.; Harley, R. A.; Hering, S. V.; Stolzenburg, M. R. A New, Portable, Real-Time Ozone Monitor. *Environ. Sci. Technol.* **2000**, *34*, 3031–3040.
- (75) Tisch, U.; Haick, H. Chemical Sensors for Breath Gas Analysis: The Latest Developments at the Breath Analysis Summit 2013. *J. Breath Res.* **2014**, *8*, 027103.
- (76) Liu, Y.; Minami, T.; Nishiyabu, R.; Wang, Z.; Anzenbacher, P. Sensing of Carboxylate Drugs in Urine by a Supramolecular Sensor Array. *J. Am. Chem. Soc.* **2013**, *135*, 7705–7712.
- (77) Minami, T.; Esipenko, N. A.; Akdeniz, A.; Zhang, B.; Isaacs, L.; Anzenbacher, P. Multianalyte Sensing of Addictive Over-the-Counter (OTC) Drugs. *J. Am. Chem. Soc.* **2013**, *135*, 15238–15243.
- (78) Peris, M.; Escuder-Gilabert, L. On-Line Monitoring of Food Fermentation Processes Using Electronic Noses and Electronic Tongues: A Review. *Anal. Chim. Acta* **2013**, *804*, 29–36.
- (79) Adley, C. Past, Present and Future of Sensors in Food Production. *Foods* **2014**, *3*, 491–510.
- (80) Zhang, C.; Bailey, D. P.; Suslick, K. S. Colorimetric Sensor Arrays for the Analysis of Beers: A Feasibility Study. *J. Agric. Food Chem.* **2006**, *54*, 4925–4931.
- (81) Olguín, C.; Laguarda-Miró, N.; Pascual, L.; García-Breijo, E.; Martínez-Mañez, R.; Soto, J. An Electronic Nose for the Detection of Sarin, Soman and Tabun Mimics and Interfering Agents. *Sens. Actuators B Chem.* **2014**, *202*, 31–37.
- (82) Schnorr, J. M.; van der Zwaag, D.; Walish, J. J.; Weizmann, Y.; Swager, T. M. Sensory Arrays of Covalently Functionalized Single-Walled Carbon Nanotubes for Explosive Detection. *Adv. Funct. Mater.* **2013**, *23*, 5285–5291.
- (83) Georgakilas, V. *Functionalization of Graphene*, Wiley-VCH: Weinheim [Germany], 2014.

- (84) Dobrokhotov, V.; Larin, A.; Sowell, D. Vapor Trace Recognition Using a Single Nonspecific Chemiresistor. *Sensors* **2013**, *13*, 9016–9028.
- (85) Richert, W.; Coelho, L. P. *Building Machine Learning Systems with Python*; Packt Publishing: Birmingham, 2013.
- (86) Hauck, T. *Scikit-Learn Cookbook*; Packt Publishing: Birmingham, U.K., 2014.
- (87) Kreno, L. E.; Leong, K.; Farha, O. K.; Allendorf, M.; Van Duyne, R. P.; Hupp, J. T. Metal–Organic Framework Materials as Chemical Sensors. *Chem. Rev.* **2012**, *112*, 1105–1125.
- (88) Vedala, H.; Sorescu, D. C.; Kotchey, G. P.; Star, A. Chemical Sensitivity of Graphene Edges Decorated with Metal Nanoparticles. *Nano Lett.* **2011**, *11*, 2342–2347.
- (89) Wang, F.; Swager, T. M. Diverse Chemiresistors Based upon Covalently Modified Multiwalled Carbon Nanotubes. *J. Am. Chem. Soc.* **2011**, *133*, 11181–11193.
- (90) Mirica, K. A.; Azzarelli, J. M.; Weis, J. G.; Schnorr, J. M.; Swager, T. M. Rapid Prototyping of Carbon-Based Chemiresistive Gas Sensors on Paper. *Proc. Natl. Acad. Sci.* **2013**, *110*, E3265–E3270.
- (91) Liu, S. F.; Moh, L. C. H.; Swager, T. M. Single-Walled Carbon Nanotube–Metalloporphyrin Chemiresistive Gas Sensor Arrays for Volatile Organic Compounds. *Chem. Mater.* **2015**, *27*, 3560–3563.
- (92) Severin, E. J.; Sanner, R. D.; Doleman, B. J.; Lewis, N. S. Differential Detection of Enantiomeric Gaseous Analytes Using Carbon Black–Chiral Polymer Composite, Chemically Sensitive Resistors. *Anal. Chem.* **1998**, *70*, 1440–1443.
- (93) Kieser, B.; Dieterle, F.; Gauglitz, G. Discrimination of Methanol and Ethanol Vapors by the Use of a Single Optical Sensor with a Microporous Sensitive Layer. *Anal. Chem.* **2002**, *74*, 4781–4787.
- (94) Li, B.; Santhanam, S.; Schultz, L.; Jeffries-EL, M.; Iovu, M. C.; Sauv e, G.; Cooper, J.; Zhang, R.; Revelli, J. C.; Kusne, A. G.; *et al.* Inkjet Printed Chemical Sensor Array Based on Polythiophene Conductive Polymers. *Sens. Actuators B Chem.* **2007**, *123*, 651–660.
- (95) Berna, A. Z.; Anderson, A. R.; Trowell, S. C. Bio-Benchmarking of Electronic Nose Sensors. *PLoS ONE* **2009**, *4*, e6406.
- (96) Campbell, M. G.; Sheberla, D.; Liu, S. F.; Swager, T. M.; Dinc a, M. Cu<sub>3</sub>(hexaiminotriphenylene)<sub>2</sub>: An Electrically Conductive 2D Metal–Organic Framework for Chemiresistive Sensing. *Angew. Chem. Int. Ed.* **2015**, *54*, 4349–4352.
- (97) Zellers, E. T.; Han, M. Effects of Temperature and Humidity on the Performance of Polymer-Coated Surface Acoustic Wave Vapor Sensor Arrays. *Anal. Chem.* **1996**, *68*, 2409–2418.
- (98) Perkins, F. K.; Friedman, A. L.; Cobas, E.; Campbell, P. M.; Jernigan, G. G.; Jonker, B. T. Chemical Vapor Sensing with Monolayer MoS<sub>2</sub>. *Nano Lett.* **2013**, *13*, 668–673.
- (99) Abbas, A. N.; Liu, B.; Chen, L.; Ma, Y.; Cong, S.; Aroonyadet, N.; K opf, M.; Nilges, T.; Zhou, C. Black Phosphorus Gas Sensors. *ACS Nano* **2015**, *9*, 5618–5624.
- (100) Muezzinoglu, M. K.; Vergara, A.; Huerta, R.; Rulkov, N.; Rabinovich, M. I.; Selverston, A.; Abarbanel, H. D. I. Acceleration of Chemo-Sensory Information Processing Using Transient Features. *Sens. Actuators B Chem.* **2009**, *137*, 507–512.

- (101) Hierlemann, A. Fundamentals of Chemical Sensing. *Integr. Chem. Microsens. Syst. CMOS Technol.* **2005**, 9–14.
- (102) Wang, L.; Kalyanasundaram, K.; Stanacevic, M.; Gouma, P. Nanosensor Device for Breath Acetone Detection. *Sens. Lett.* **2010**, *8*, 709–712.
- (103) Someya, T.; Dodabalapur, A.; Huang, J.; See, K. C.; Katz, H. E. Chemical and Physical Sensing by Organic Field-Effect Transistors and Related Devices. *Adv. Mater.* **2010**, *22*, 3799–3811.
- (104) *Advanced Intelligent Computing Theories and Applications*; Springer: Berlin; Heidelberg; New York, NY, 2008.
- (105) Strobl, C.; Boulesteix, A.-L.; Zeileis, A.; Hothorn, T. Bias in Random Forest Variable Importance Measures: Illustrations, Sources and a Solution. *BMC Bioinformatics* **2007**, *8*, 25.
- (106) Silbey, R. J.; Alberty, R. A.; Alberty, R. A. *Physical Chemistry*; Wiley: New York, 2001.
- (107) Kiskinova, M.; Yates, Jr., J. T. Observation of Steric Conformational Effects in Hydrocarbon Adsorption and Decomposition: Cis and Trans-Butene-2 on Si(100)-(2x1). *Surf. Sci.* **1995**, *325*, 1–10.
- (108) Daasbjerg, K. Organic Surface Chemistry.
- (109) *Functionalization of Graphene*; Geörgakilas, V., Ed.; Wiley-VCH: Weinheim, 2014.
- (110) Felten, A.; Eckmann, A.; Pireaux, J.-J.; Krupke, R.; Casiraghi, C. Controlled Modification of Mono- and Bilayer Graphene in O<sub>2</sub>, H<sub>2</sub> and CF<sub>4</sub> Plasmas. *Nanotechnology* **2013**, *24*, 355705.
- (111) Paulus, G. L. C.; Wang, Q. H.; Strano, M. S. Covalent Electron Transfer Chemistry of Graphene with Diazonium Salts. *Acc. Chem. Res.* **2013**, *46*, 160–170.
- (112) Chehimi, M. M.; Wiley InterScience (Online service). *Aryl Diazonium Salts New Coupling Agents in Polymer and Surface Science*; John Wiley & Sons: Weinheim, Germany, 2012.
- (113) Sharma, R.; Baik, J. H.; Perera, C. J.; Strano, M. S. Anomalously Large Reactivity of Single Graphene Layers and Edges toward Electron Transfer Chemistries. *Nano Lett.* **2010**, *10*, 398–405.
- (114) Farmer, D. B.; Golizadeh-Mojarad, R.; Perebeinos, V.; Lin, Y.-M.; Tulevski, G. S.; Tsang, J. C.; Avouris, P. Chemical Doping and Electron–Hole Conduction Asymmetry in Graphene Devices. *Nano Lett.* **2009**, *9*, 388–392.
- (115) Park, J.; Yan, M. Covalent Functionalization of Graphene with Reactive Intermediates. *Acc. Chem. Res.* **2013**, *46*, 181–189.
- (116) Lonkar, S. P.; Deshmukh, Y. S.; Abdala, A. A. Recent Advances in Chemical Modifications of Graphene. *Nano Res.* **2015**, *8*, 1039–1074.
- (117) Ryan, M. A.; Shevade, A. V.; Zhou, H.; Homer, M. L. Polymer–carbon Black Composite Sensors in an Electronic Nose for Air-Quality Monitoring. *MRS Bull.* **2004**, *29*, 714–719.
- (118) Ponrathnam, T.; Cho, J.; Kurup, P. U.; Kumar, J.; Nagarajan, R. Enhancing Detection of Nitroaromatic Vapors by Utilizing Polymer Coatings on Quartz Crystal Microbalances Having Strong Dipoles. *Sens. Actuators B Chem.* **2015**, *216*, 443–452.
- (119) Grate, J. W. Acoustic Wave Microsensor Arrays for Vapor Sensing. *Chem. Rev.* **2000**, *100*, 2627–2648.

- (120) *Computational Methods for Sensor Material Selection*; Ryan, M. A.; Shevade, A. V.; Taylor, C. J.; Homer, M. L.; Blanco, M.; Stetter, J. R., Eds.; Springer US: New York, NY, 2010.
- (121) Albert, K. J.; Lewis, N. S.; Schauer, C. L.; Sotzing, G. A.; Stitzel, S. E.; Vaid, T. P.; Walt, D. R. Cross-Reactive Chemical Sensor Arrays. *Chem. Rev.* **2000**, *100*, 2595–2626.
- (122) Brudzewski, K.; Osowski, S.; Pawlowski, W. Metal Oxide Sensor Arrays for Detection of Explosives at Sub-Parts-per Million Concentration Levels by the Differential Electronic Nose. *Sens. Actuators B Chem.* **2012**, *161*, 528–533.
- (123) Gao, T.; Woodka, M. D.; Brunschwig, B. S.; Lewis, N. S. Chemiresistors for Array-Based Vapor Sensing Using Composites of Carbon Black with Low Volatility Organic Molecules. *Chem. Mater.* **2006**, *18*, 5193–5202.
- (124) Nallon, E. C.; Schnee, V. P.; Bright, C.; Polcha, M. P.; Li, Q. Chemical Discrimination with an Unmodified Graphene Chemical Sensor. *ACS Sens.* **2015**, 151022135358004.
- (125) Liu, L.-H.; Yan, M. Functionalization of Pristine Graphene with Perfluorophenyl Azides. *J. Mater. Chem.* **2011**, *21*, 3273.
- (126) Foley, B. M.; Hernández, S. C.; Duda, J. C.; Robinson, J. T.; Walton, S. G.; Hopkins, P. E. Modifying Surface Energy of Graphene via Plasma-Based Chemical Functionalization to Tune Thermal and Electrical Transport at Metal Interfaces. *Nano Lett.* **2015**, *15*, 4876–4882.
- (127) Covington, J. A.; Gardner, J. W.; Hamilton, A.; Pearce, T. C.; Tan, S. L. Towards a Truly Biomimetic Olfactory Microsystem: An Artificial Olfactory Mucosa. *IET Nanobiotechnol.* **2007**, *1*, 15.
- (128) Câmara, J. S.; Marques, J. C.; Perestrelo, R. M.; Rodrigues, F.; Oliveira, L.; Andrade, P.; Caldeira, M. Comparative Study of the Whisky Aroma Profile Based on Headspace Solid Phase Microextraction Using Different Fibre Coatings. *J. Chromatogr. A* **2007**, *1150*, 198–207.

## **Biography**

Eric C. Nallon graduated from Crestwood High School, Mountaintop, Pennsylvania, in 2002. He received his Bachelor of Science in Electrical Engineering from The Pennsylvania State University in 2007. He has been employed as an Electrical Engineer at the US Army Night Vision and Electronics Sensors Directorate since 2008, and received M.S. in May 2012 and Ph.D in May 2016, both in Electrical and Computer Engineering from George Mason University.